



저작자표시-비영리-변경금지 2.0 대한민국

이용자는 아래의 조건을 따르는 경우에 한하여 자유롭게

- 이 저작물을 복제, 배포, 전송, 전시, 공연 및 방송할 수 있습니다.

다음과 같은 조건을 따라야 합니다:



저작자표시. 귀하는 원저작자를 표시하여야 합니다.



비영리. 귀하는 이 저작물을 영리 목적으로 이용할 수 없습니다.



변경금지. 귀하는 이 저작물을 개작, 변형 또는 가공할 수 없습니다.

- 귀하는, 이 저작물의 재이용이나 배포의 경우, 이 저작물에 적용된 이용허락조건을 명확하게 나타내어야 합니다.
- 저작권자로부터 별도의 허가를 받으면 이러한 조건들은 적용되지 않습니다.

저작권법에 따른 이용자의 권리는 위의 내용에 의하여 영향을 받지 않습니다.

이것은 [이용허락규약\(Legal Code\)](#)을 이해하기 쉽게 요약한 것입니다.

[Disclaimer](#)

2022년 8월
박사학위 논문

**Design and Synthesis of
Nanostructured Transition Metal
(Co, Mn, Fe, and Ni) Compounds for
Electrochemical Water Splitting**

Graduate School of Chosun University

Department of Advanced Materials Engineering

LI XUE

Design and Synthesis of Nanostructured Transition Metal (Co, Mn, Fe, and Ni) Compounds for Electrochemical Water Splitting

전기화학적 물 분해를 위한 나노 구조 전이금속 (Co, Mn,
Fe, Ni) 화합물의 설계 및 합성

August 26, 2022

Graduate School of Chosun University
Department of Advanced Materials Engineering

LI XUE

Design and Synthesis of Nanostructured Transition Metal (Co, Mn, Fe, and Ni) Compounds for Electrochemical Water Splitting

Advisor: Prof. Yung Tae Yoo






A dissertation submitted in partial fulfillment of the
requirements for a Doctoral Degree

April, 2022

Graduate School of Chosun University
Department of Advanced Materials Engineering

LI XUE

이 설의 박사학위논문을 인준함

위원장	조선대학교 교수	<u>박정우</u>	
위원	조선대학교 교수	<u>박설현</u>	
위원	조선대학교 교수	<u>곽재복</u>	
위원	전남대학교 교수	<u>김진혁</u>	
위원	조선대학교 교수	<u>유영태</u>	

2022년 6월

조선대학교 대학원

TABLE OF CONTENTS

ABBREVIATIONS.....	iv
LIST OF TABLES.....	vii
LIST OF FIGURES.....	viii
ABSTRACT (ENGLISH).....	xii
ABSTRACT (KOREAN).....	xiv
1. Introduction.....	1
1.1 Background.....	1
1.2 Fundamentals of ECWS.....	3
1.2.1 The Media of ECWS.....	4
1.2.2 Critical Parameters of ECWS.....	5
1.2.3 Mechanisms for ECWS.....	7
1.3 Catalysts Based on Transition Metal Compounds (TMC).....	8
1.3.1 Literature Review for TMC.....	9
1.3.2 Strategies to Boost Electrocatalytic Performance of TMC.....	11
1.3.3 TMC Investigated for ECWS in This Research Work.....	12
1.4 Methodologies Used for Deposition of TMC.....	13
1.5 Objectives of This Thesis.....	13
1.6 Flow Chart of This Research Work.....	16
2. Synthesis and Characterization Techniques.....	17
2.1 Synthesis of TMC.....	17
2.1.1 HT Method.....	18
2.1.2 ED method.....	18
2.1.3 CBD Method.....	19

2.2 Advanced Characterization Techniques.....	20
2.2.1 XPS	20
2.2.2 XRD	21
2.2.3 FE-SEM	22
2.2.4 TEM	23
2.2.5 Raman Spectroscopy	23
2.2.6 FTIR.....	24
2.3 Electrochemical Characterization.....	24
2.3.1 Linear Sweep Voltammetry (LSV) Measurement.....	24
2.3.2 CV Measurement	25
2.3.3 EIS Measurement.....	26
3. Synthesis and Characterization of Electrocatalysts.....	28
3.1 Substrate Cleaning.....	28
3.2 Core-shell Nanowires of CoMn-LDH@Ni(OH) ₂ Catalysts.....	28
3.2.1 HT Synthesis of CoMn-LDH.....	28
3.2.2 ED Synthesis of Ni(OH) ₂	28
3.2.3 Formation Mechanism	29
3.2.4 Structural Analysis	31
3.2.5 Morphological and Compositional Analysis.....	32
3.2.6 XPS Analysis	35
3.3 Nanowire-Nanosheet-like Dual Structured CoMnFeO ₄	39
3.3.1 HT Synthesis of M _x Mn _y O ₄ (M = Co, Fe, and Ni).....	39
3.3.2 HT Synthesis of CoMnFeO ₄	40
3.3.3 Formation Mechanism of CoMnFeO ₄	41

3.3.4 Morphological Analysis of $M_xMn_yO_4$ (M = Co, Fe, and Ni).....	42
3.3.5 Structural Analysis of $CoMnFeO_4$	43
3.3.6 Morphological Analysis of $CoMnFeO_4$	45
3.3.7 XPS Analysis of $CoMnFeO_4$	48
3.4 Summary.....	50
4. Investigation of Electrochemical Performance of Catalysts and Their Application in Overall Water splitting.....	51
4.1 Electrochemical Measurements.....	51
4.2 Core-Shell $CoMn-LDH@Ni(OH)_2$ for Overall Water Splitting.....	52
4.2.1 Optimization of $CoMn-LDH@Ni(OH)_2$ via OER Studies.....	52
4.2.2 Electrochemical Activity for OER and HER.....	54
4.2.3 Origin of Superior Performance.....	59
4.2.4 $CoMn-LDH@Ni(OH)_2$ for Overall Water Splitting.....	62
4.2.5 Mechanism Discussion.....	63
4.3 Heteroatomic Doping of $CoMnFeO_4$ for Water Oxidation.....	65
4.3.1 Performance Optimization of $CoMnFeO_4$ via OER studies.....	65
4.3.2 Influence of Fe Concentration and Annealing Conditions on OER.....	69
4.3.3 Electrocatalytic Activity for OER.....	71
4.3.4 Origin of Superior OER activity.....	75
5. Conclusion and Future Scope of Research.....	80
5.1 Conclusions.....	80
5.2 Future Scope of Research.....	83
ACKNOWLEDGEMENT.....	84
PUBLICATIONS.....	85

BIBLIOGRAPHY.....	87
APPENDICES	108
Appendix “A” Main Reagents and Materials	108
Appendix “B” Synthesis and Characterization Tools.....	109
Appendix “C” Electrolyte Preparation and Microscopy Sample Preparation	110

ABBREVIATIONS

CBD	Chemical Bath Deposition
CFP	Carbon Fiber Paper
CO ₂	Carbon Dioxide
CIS	Commonwealth of Independent States
CNTs	Carbon Nanotubes
CoMn-LDH@Ni(OH) ₂	Cobalt Manganese-Layered Double Hydroxide Coated by Nickel Hydroxide
Co ₂ MnO ₄	Cobalt Manganese Oxide
CoMnFeO ₄	Iron Doped Cobalt Manganese Oxide
C _{dl}	Double-Layer Capacitance
CV	Cyclic Voltammetry
CoP	Cobalt Phosphide
DI-water	Deionized Water
EC	Electrical Conductivity
ECWS	Electrochemical Water Splitting
EDS	Energy-Dispersive Spectroscopy
ED	Electrochemical Deposition
ECSA	Electrochemical Active Surface Area
EIS	Electrochemical Impedance Spectroscopy
FTIR	Fourier Transform Infrared Spectroscopy
FFER	Fossil Fuel Energy Resources
Fe _x Mn _y O ₄	Iron Manganese Oxide
FE-SEM	Field Emission Scanning Electron Microscope
LSV	Linear Sweep Voltammetry
H ₂	Hydrogen
HT	Hydrothermal
HER	Hydrogen Evolution Reaction
J _c	Current Density
KOH	Potassium Hydroxide

MOF	Metal-Organic Framework
LDH	Layered Double Hydroxide
MA	Mass Activity
NF	Nickel Foam
Ni(OH) ₂	Nickel Hydroxide
Ni _x Mn _y O ₄	Nickel Manganese Oxide
O ₂	Oxygen
OER	Oxygen Evolution Reaction
R _s	Resistance of Electrolyte Solution
R _{ct}	Resistance of Charge Transfer
XPS	X-Ray Photoelectron Spectroscopy
SA	Specific Activity
SAED	Selected Area Diffraction
XRD	X-Ray Diffraction
TEM	Transmission Electron Microscope
T _s	Tafel Slope
TMC	Transition Metal Compounds

LIST OF TABLES

Table 1. 1 Total energy consumption in recent years and prediction of future (unit: Mt _{oe}).	2
Table 1. 2 New catalysts based on TMC and reference catalysts.	13
Table 4. 1 Comparison of OER performances of previously reported OER electrocatalysts.	55
Table 4. 2 Comparison of HER performances of previously reported HER electrocatalysts.	58
Table 4. 3 Comparison of overall water splitting performances of previously reported electrocatalysts.	62
Table 4. 4 Comparison of OER performances for different molar ratios and concentrations of Co _x Mn _y O ₄	66
Table 4. 5 Comparison of OER performances for different molar ratios and concentrations of Fe _x Mn _y O ₄	67
Table 4. 6 Comparison of OER performances for different molar ratios and concentrations of Ni _x Mn _y O ₄	68
Table 4. 7 Electrocatalytic OER performances of the previously reported Co- or/ and Mn-based oxides catalysts.....	74

LIST OF FIGURES

Figure 1. 1 (a) The world Energy demand-supply gap and (b) Energy demand [5].	1
Figure 1. 2 The strategy for energy sustainable development.	2
Figure 1. 3 Comparison of different energy sources.	3
Figure 1. 4 Illustration of overall ECWS system.	4
Figure 1. 5 The illustration of the role of the catalyst in the electrolysis progress.	5
Figure 1. 6 Illustrations of critical parameters of ECWS. (a) Overpotential, (b) Tafel slope, (c) Stability in terms of I-t (inset: E-t), and (d) Electrochemical active surface area (ECSA).	6
Figure 1. 7 Simplified illustrations of the mechanism of ECWS.	8
Figure 1. 8 Electrocatalysts based on TMC for ECWS[57].	10
Figure 1. 9 Strategies for obtaining efficient transition metal electrocatalysts.	12
Figure 1. 10 Flowchart illustrating the whole work.	16
Figure 2. 1 The two basic approaches used for the synthesis of nanostructured TMC.	17
Figure 2. 2 Schematic of the HT method.	18
Figure 2. 3 Schematic of ED method.	19
Figure 2. 4 Schematic of CBD method.	20
Figure 2. 5 Schematic of FE-SEM [74].	22
Figure 2. 6 LSV plot of (a) OER and (b) HER.	24
Figure 2. 7 A typical CV curve.	26
Figure 2. 8 Nyquist plot of EIS and corresponding equivalent circuit model (inset).	27
Figure 3. 1 Schematic diagram of synthesis procedures of CoMn-LDH@Ni(OH) ₂ .	29
Figure 3. 2 Structural analysis of CoMn-LDH@Ni(OH) ₂ and CoMn-LDH: (a) XRD patterns and (b) FTIR spectra.	31
Figure 3. 3 FE-SEM images of (a, b) bare NF and (c, d) CoMn-LDH@Ni(OH) ₂ .	32
Figure 3. 4 The FE-SEM images of (a, b) CoMn-LDH nanowires; (c, d) CoMn-LDH@Ni(OH) ₂ at different high magnifications.	33
Figure 3. 5 (a) EDS analysis, (b) TEM image, (c) HRTEM image, and (d-g) EDS elemental mapping of CoMn-LDH nanowires.	34
Figure 3. 6 (a) TEM image (b) HR-TEM image (inset: corresponding SAED). (c) EDS	

analysis and (d-f) Elemental mapping of CoMn-LDH@Ni(OH) ₂	35
Figure 3. 7 (a) Full scan XPS spectrum of Ni(OH) ₂ and high-resolution XPS spectra of (b) Ni 2p, and (c) O 1s.....	36
Figure 3. 8 (a) Full-scan XPS spectrum of CoMn-LDH, and XPS spectra of (b) Co 2p, (c) Mn 2p, and (d) O 1s.....	37
Figure 3. 9 XPS survey spectrum of CoMn-LDH@Ni(OH) ₂	37
Figure 3. 10 High-resolution XPS spectra of CoMn-LDH@Ni(OH) ₂ . (a) Ni 2p, (b) Co 2p, (c) Mn 2p, and (d) O 1s.	38
Figure 3. 11 Schematic for the preparation of M _x Mn _y O ₄ catalysts.....	39
Figure 3. 12 Schematic of calcination device.....	40
Figure 3. 13 Schematic for the preparation of CoMnFeO ₄ catalysts.....	41
Figure 3. 14 The optical image of the samples: (a) bare NF, (b) precursor after HT, and (c) CoMnFeO ₄ after annealing.....	42
Figure 3. 15 FE-SEM images at different magnifications of (a, b) Co ₂ MnO ₄ , (c, d) Fe ₂ MnO ₄ , and (e, f) Ni ₂ MnO ₄	42
Figure 3. 16 XRD patterns of (a, b) Co ₂ MnO ₄ and CoMnFeO ₄ and (c) CoMnFeO ₄ series.....	44
Figure 3. 17 (a) FE-SEM images of (c, d) Co ₂ MnO ₄ nanowires and (e, f) CoMnFeO ₄ at different magnifications.....	45
Figure 3. 18 FE-SEM images of CoMnFeO ₄ with Fe concentration of (a, b) 0.5, (c, d) 1.0, and (e, f) 2.0 mmol.....	46
Figure 3. 19 (a-c) TEM image (d) HR-TEM image (inset: corresponding SAED). (e-n) EDS profiles and elemental mapping of CoMnFeO ₄	47
Figure 3. 20 (a) SEM image, (b) EDS profile, and (c) elemental mapping of CoMnFeO ₄	48
Figure 3. 21 XPS survey spectra of CoMnFeO ₄ and Co ₂ MnO ₄	48
Figure 3. 22 High-resolution XPS spectra of CoMnFeO ₄ and Co ₂ MnO ₄ . (a) Co 2p, (b) Mn 2p, (c) Fe 2p, and (d) O 1s.....	49
Figure 4. 1 OER polarization curves of CoMn-LDH (1:1), Mn (OH) ₂ , Co(OH) ₂ , and bare NF in 1.0 M KOH at a scan rate of 1 mV s ⁻¹ . (b) Overpotential at a current density of 50 and 100 mA cm ⁻² (c) Optical images.....	52
Figure 4. 2 (a) OER polarization curves of CoMn-LDH with different Co: Mn molar	

ratios in 1.0 M KOH at a scan rate of 1 mV s⁻¹. (b) Tafel plots. (c) Overpotential at a current density of 50 and 100 mA cm⁻²..... 53

Figure 4. 3 (a) OER polarization curves of all catalysts at a scan rate of 1 mV s⁻¹ in 1 M KOH. (b) Corresponding Tafel plots (c) Comparative plots of overpotential and Tafel slopes of bare NF, Ni(OH)₂, CoMn-LDH, and CoMn-LDH@Ni(OH)₂ at a current density of 30 mA cm⁻². (d) Long-term stability measurement of CoMn-LDH@Ni(OH)₂ at 30 mA cm⁻² for 25 h. inset: FE-SEM images of CoMn-LDH@Ni(OH)₂ after long-term stability test..... 54

Figure 4. 4 XPS spectra of CoMn-LDH@Ni(OH)₂ after 25 hours stability test. (a) XPS survey spectrum and high-resolution XPS spectra of (b) Ni 2p, (c) Co 2p, (d) Mn 2p, and (e) O 1s..... 56

Figure 4. 5 (a) HER polarization curves of all catalysts at a scan rate of 1 mV s⁻¹ in 1 M KOH. (b) Comparison of overpotentials at current densities of -10, -50, and -100 mA cm⁻² (c) Corresponding Tafel plots..... 57

Figure 4. 6 (a) Multiple current process (b) Long-term stability measurement of CoMn-LDH@Ni(OH)₂ at -10 mA cm⁻² for 25 hours. (c, d) FE-SEM images of CoMn-LDH@Ni(OH)₂ after long-term stability test. 59

Figure 4. 7 CV curves at different scan rates of (a) CoMn-LDH, and (b) Ni(OH)₂. 59

Figure 4. 8 (a) CV curves at different scan rates for CoMn-LDH@Ni(OH)₂. (b) Capacitive current density VS. scan rate, (c) Nyquist plots, and (d) Mass and specific activities at an overpotential of 320 mV of CoMn-LDH@Ni(OH)₂, CoMn-LDH, and Ni(OH)₂..... 61

Figure 4. 9 The equivalent circuit of CoMn-LDH@Ni(OH)₂..... 61

Figure 4. 10 Electrocatalytic performance of CoMn-LDH@Ni(OH)₂ towards overall water splitting (a) LSV polarization plot of a two-electrode system (inset: setup of the two electrode system) and (b) long-term stability over 25 hours at 10 mA cm⁻²..... 62

Figure 4. 11 Schematic of the overall water splitting process by the CoMn-LDH@Ni(OH)₂ core-shell nanowires. 64

Figure 4. 12 OER polarization plots of Co_xMn_yO₄..... 66

Figure 4. 13 OER polarization plots of Fe_xMn_yO₄..... 67

Figure 4. 14 OER polarization plots of Ni_xMn_yO₄..... 68

Figure 4. 15 The OER behavior of samples with different Fe concentrations..... 69

Figure 4. 16 (a) The LSV curves, (b)overpotentials under 200 mA cm^{-2} , and (c) XRD patterns of samples at different calcinated temperatures. 70

Figure 4. 17 (a) The LSV curves, (b)overpotentials under 200 mA cm^{-2} , and (c) XRD patterns of samples with different calcinated time..... 71

Figure 4. 18 The LSV curves of samples at different calcinated atmospheres (a) and scan rates (b). 71

Figure 4. 19 (a) LSV polarization plots, (b) Corresponding Tafel curves, (c) Overpotential and Tafel slopes of bare NF, Co_2MnO_4 , and CoMnFeO_4 at 10 mA cm^{-2} , (d) Multistep chronopotentiometry of CoMnFeO_4 at $10 \sim 100 \text{ mA cm}^{-2}$ for each 500 s, inset: enlarged region of green dotted line circle in Figure. 4. 19d, (e) Long-term stability measurement of CoMnFeO_4 , and (f) LSV plots before and after 80 h stability test..... 72

Figure 4. 20 (a) A comparison of overpotentials to reach different current densities for CoMnFeO_4 and Co_2MnO_4 , (b) the LSV curves in the low current density range of CoMnFeO_4 and Co_2MnO_4 73

Figure 4. 21 (a) FE-SEM, inset TEM, and (b) XPS analyses of CoMnFeO_4 after stability test of 80 hours. 75

Figure 4. 22 (a-e) CV curves, (f) Curves of capacitive current density at different scan rates of CoMnFeO_4 -0.5, CoMnFeO_4 -1.0, and CoMnFeO_4 -2.0..... 76

Figure 4. 23 (a) Curves of capacitive current density at different scan rates, (b) ECSA normalized LSV plots, (c) Nyquist plots, inset: a fitted equivalent circuit, and (d) MA and SA at a potential of 1.65 V..... 77

Figure 4. 24 (a) Nyquist plots of CoMnFeO_4 -0.5, CoMnFeO_4 -1.0, and CoMnFeO_4 -2.0. (b) SA at a potential range of 1.50 to 1.68 V of CoMnFeO_4 and Co_2MnO_4 ... 78

ABSTRACT (ENGLISH)

Design and Synthesis of Nanostructured Transition Metal (Co, Mn, Fe, and Ni) Compounds for Electrochemical Water Splitting

Li Xue

Advisor: Prof. Yung Tae Yoo, Ph.D.

Dept. of Advanced Materials Engineering

Graduate School of Chosun University

Depletion of fossil fuels, coupled with the climate change related to greenhouse gas emissions, has decided the significantly urgent need of developing highly efficient and sustainable alternative energy sources. To note, a tremendous effort has been paid to diminish greenhouse gas emissions and generate zero-carbon, green, and sustainable energy sources. It is well known that hydrogen (H_2) is a promising energy source because of its unique features (sustainability, lightweight, and high energy density). Electrochemical water splitting (ECWS) is one type of sustainable solution for generating H_2 to meet the energy demands without carbon emission.

In this work, the development of novel electrocatalysts is aimed to improve energy efficiency in ECWS, especially involving oxygen evolution reaction (OER) and hydrogen evolution reaction (HER). Transition metals (nickel, cobalt, manganese, and iron)-based compounds including hydroxides and oxides have been explored and evaluated as electrochemical catalysts. The transition metal compounds were synthesized on a conductive and porous substrate (Ni foam) by utilizing simplistic approaches like the hydrothermal method (HT) and electrodeposition (ED). Electrocatalyst performance evaluation parameters such as overpotential, Tafel slope, electrochemical active surface

area, exchange current density, long-term stability as well as charge transfer resistance were investigated in detail.

In detail, Nickel hydroxide coated cobalt manganese layered double hydroxide (CoMn-LDH@Ni(OH)₂) nanowires were prepared by HT followed by the ED method. The OER, HER, and overall water splitting activity of as-prepared CoMn-LDH@Ni(OH)₂ were discussed. Iron-doped cobalt manganese spinel-type oxide (CoMnFeO₄) was synthesized by HT followed by calcination for 1 hour at 300°C. The influence of iron concentration and annealing conditions on the catalytic activity of Co-Mn oxide was studied. The OER performance of this as-prepared CoMnFeO₄ was discussed. It was concluded that the CoMn-LDH@Ni(OH)₂ is more efficient than Ni₂MnO₄, Fe₂MnO₄, and CoMnFeO₄ for OER because the compound incorporates a unique heterogeneous nanostructure, synergistic effect of core & shell, and simple deposition on nickel foam (NF) substrate without using a binder.

Keywords: Electrochemical water splitting, Transition metal compound, Core-shell, Nanowire-nanosheet coexistence, Fe-doping, synergistic effect,

ABSTRACT (KOREAN)

초록

전기화학적 물 분해를 위한 나노 구조 전이금속(Co, Mn, Fe, Ni) 화합물의 설계 및 합성

이 설

지도교수 유영 태

첨 단 소 재 공 학 과

조선대학교 대학원

온실가스 배출로 인한 기후변화 및 화석연료의 고갈은 효율적이고 지속가능한 대체 에너지원의 개발이 시급해지도록 만들었다. 온실가스 배출을 줄이고 제로-탄소 및 지속 가능한 에너지를 개발하기 위해 많은 연구자들은 엄청난 노력을 기울이고 있다. 그 중에서, 수소(H₂)는 가볍고, 높은 에너지 밀도를 가지기 때문에 지속가능한 대체 에너지 물질로 잘 알려져 있다. 수소를 생산하기 위한 방법은 여러가지가 있지만, 그 중 ECWS(Electrochemical water splitting)는 Zero-carbon 및 높은 에너지 수요를 만족시키는 지속가능한 해결책으로 각광받고 있다.

이번 연구에서는, ECWS의 에너지 효율을 개선하기 위해 새로운 전기 촉매를 개발하였고, 산소 발생 반응(OER)과 수소 발생 반응(HER)에 대한 접근 방식을 모두 포함하고 있다. 이를 수행하기 위해 전이금속(Co, Mn, Ni, Fe) 기반의 산화물, 수산화물, 셀렌화물을 포함하는 다양한 물질들을 조사하였고 평가하였다. HT 및 ED 법과 같은 간단한 접근법을 이용하여 전도성 및 다공성의 Ni 기판(NF)상에 전이금속 화합물을 형성시켰다.

이를 평가하기 위해 과전위, Tafel slope, 전기화학적 활성 표면적(ECSA), 교환전류밀도, 장기 안정성 및 전하이동 저항 등의 전기화학적 성능을 포함하는 다양한 parameter를 자세히 조사하였다.

구체적으로는, HT 법을 이용하여 CoMn 코어를 합성하였고, ED 법을 이용하여 Ni(OH)₂ shell 을 합성하였다. 최종적으로는 코어(CoMn)-셸 Ni(OH)₂ 구조를 갖는 Ni(OH)₂ 가 코팅된 CoMn 이중 수산화물(CoMn-LDH@Ni(OH)₂) 나노 와이어를 제조하였다. 제조된 (CoMn-LDH@Ni(OH)₂)의 산소발생반응, 수소발생반응 및 overall-water splitting 의 성능에 대해 의논하였다.

스피넬 구조를 갖는 철이 도핑된 코발트 망간산화물(CoMnFeO₄)은 HT 법으로 합성한 후 300°C 에서 1 시간 동안 하소시켰다. 또한, 철의 농도 및 열처리 조건에 따라 스피넬 구조를 갖는 Co-Mn 산화물의 촉매 성능 변화를 연구하였다. 이에 따라, 준비된 CoMnFeO₄ 의 산소발생반응의 성능이 논의되었다. 이 연구를 통해, CoMn-LDH@Ni(OH)₂ 는 CoMnFeO₄ 보다 더 효율적이라는 결론을 내릴 수 있었다. 특히 CoMn-LDH@Ni(OH)₂ 물질의 경우, core 와 shell 의 독특한 계층적 나노 구조가 만드는 시너지 효과가 있기 때문이다. 또한 이 물질을 합성할 경우 binder 가 필요하지 않아 증착이 용이하다는 장점이 있다.

Keywords: 전기화학적 물분해, 전이금속화합물, 코어-셸, Nanowire-nanosheet coexistence, Fe-doping, 시너지 효과

1. Introduction

1.1 Background

Due to the speedy advancement of the worldwide economy, the living conditions of people improved significantly in the 21st century. However, around 0.9 billion people are still living in underserved areas with energy deficiency. In 2050, the global human population growth is predicted more than 2 billion [1] accompanied by enormously aggravated global energy demands, which will increase one time compared to that of the 1990 s (Table 1. 1)[2][3] The distance between world energy demand and supply was projected to expand, as shown in Figure 1. 1[4][5]. Globally, more than 4/5 of this energy consumption is achieved by the conversion of fossil fuel energy resources (FFERs). Also, FFERs such as coal, natural gas, and petroleum which are rich in carbon atoms evolute about 2/3 of total global carbon dioxide (CO₂) emissions when they are used up. Consequently, global warming and climate change become crucial issues due to CO₂ being a big number of greenhouse gases. Therefore, ensuring global energy demands and reducing CO₂ emissions are becoming the worldwide primary research topic of sustainable development [6]. Investigating new green, renewable, and sustainable energy source with carbon-free emissions in nature could be an urgent strategy for energy sustainable development (Figure 1.2).

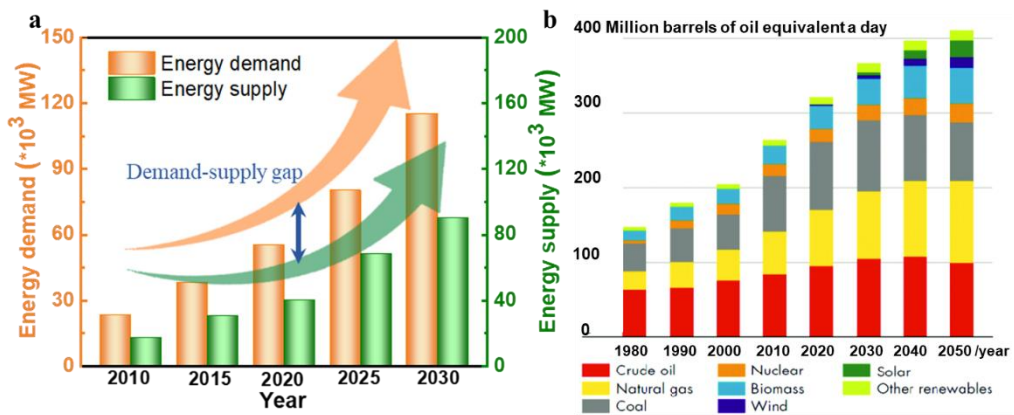


Figure 1. 1 (a) The world Energy demand-supply gap and (b) Energy demand [5].

Table 1. 1 Total energy consumption in recent years and prediction of future (unit: Mt_{oe}).

Year	Asia	Africa	Middle East	America	Europe	CIS	Pacific	Total
2050	8433	1082	823	3206	1536	1055	143	16278
2030	7376	838	778	3233	1732	1043	152	15152
2018	5859	850	803	3380	1847	1081	158	13978
2010	4825	689	647	3265	1927	1008	150	12511
2000	2886	487	372	3121	1853	898	129	9746
1990	2113	381	223	2583	1785	1372	104	8561

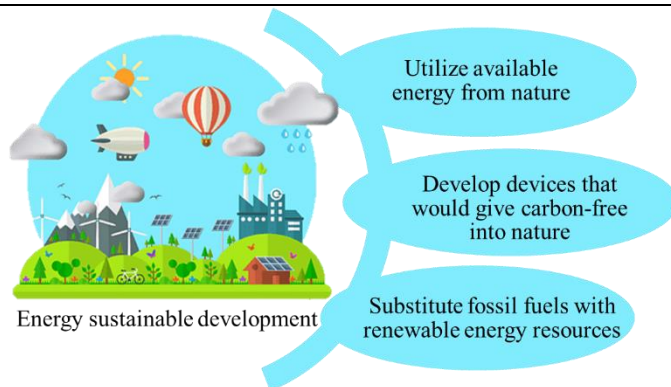


Figure 1. 2 The strategy for energy sustainable development.

Hydrogen (H₂) possesses the merits of sustainability, lightweight, and high-energy-density (**Figure 1.3**) and is expected to be the most promising fuel for substituting traditional FFER [6] [7] [8]. As we know, H₂ can be produced from biomass, water, natural gas, and coal gasification. Among all, steam methane reforming is the current main strategy, and more than 90% of H₂ is being generated from it[4]. However, this technique still emits CO₂ into the environment. Another option is to utilize earth-abundant feedstock including wind, solar, and water to generate H₂. Water which is only composed of H and O elements is recognized as the optimal candidate to derive H₂ production.

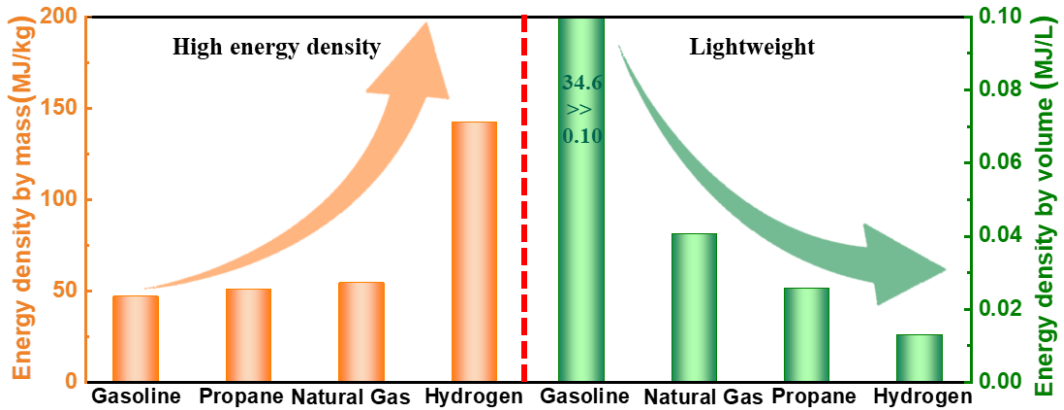
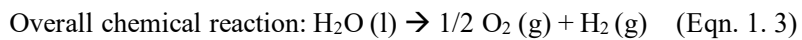
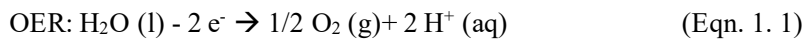


Figure 1. 3 Comparison of different energy sources.

1.2 Fundamentals of ECWS

ECWS is considered as a crucial alternative approach for sustainability by generating renewable H₂ which is an environment-friendly and promising candidate worldwide replacing FFER via converting electrical energy. In detail, ECWS represents splitting H₂O to oxygen (O₂) and H₂ under a continuous current electricity supply with a catalyst in an electrolyte solution. Typically, it includes two different cell reactions, the anodic reaction (OER) and cathodic reaction (HER) (**Figure 1. 4**)[9]. The OER and HER are expressed as follows:[10]



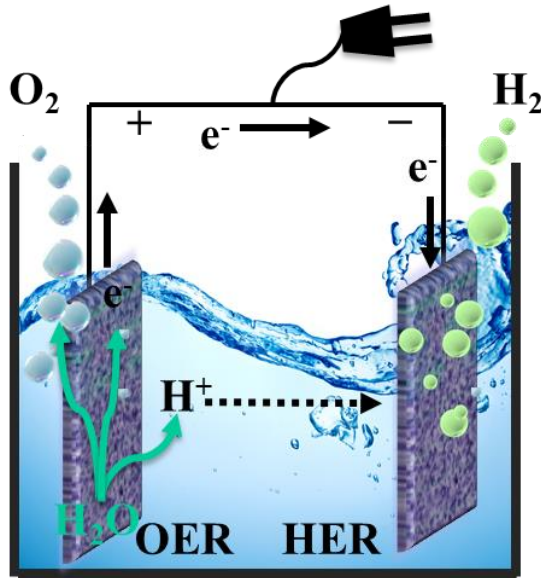


Figure 1. 4 Illustration of overall ECWS system.

It is projected that there is a change of 237.2 KJ/mol for Gibbs free energy which is the minimum energy demand during a catalytic process. In addition, the standard cell potential (E^0) can be obtained as follows:

$$E^0 = - \Delta G^0 / (n \times F) \quad (\text{Eqn. 1. 4})$$

here, n denotes the number of transferred electrons, and ' F ' denotes the Faraday constant. Hence, the corresponding E^0 is ~ 1.23 V for splitting H_2O into its component [11]. While the Nernst equation corresponding to HER can be expressed as follows:

$$E = E^0 - RT \ln [P_{H_2} / (P^0 \alpha^2)] / (2F) = -0.059 \times pH \text{ (V vs. RHE)} = 0 \text{ (V vs. RHE)} \dots \text{ Eqn. 1. 5}$$

here, ' E ' denotes the Nernstian potential of HER under the standard thermodynamic equilibrium condition, ' E^0 ' denotes the proton reduction potential which equals 0, ' R ' denotes a constant, ' T ' denotes temperature which equals 298 K, ' P ' denotes the pressure, ' α ' denotes the effective concentration of H^+ , and ' F ' denotes a faraday constant [12].

1.2.1 The Media of ECWS

On a lab scale, water is used as both reactant and electrolyte in the process of ECWS. As the literature reported, resistance in the electrolyte is a key factor to optimize the electrolyte

concentration. For instance, the alkaline electrolyte containing 35 wt% KOH has a conductivity of 2.7 S cm^{-1} [13]. Besides, corrosion in alkaline media is less and easier to handle than in acidic media, followed by cheaper cell catalysts and less maintenance. Moreover, it can generate higher purity H_2 [14]. Furthermore, in comparison to different alkaline electrolytes, KOH causes low corrosion and slightly low resistance than that NaOH and more H_2 is released in KOH when under the same conditions. Therefore, strongly alkaline media containing 1 mol/L KOH ($\text{pH} \approx 14$) was chosen for an electrolyte solution during the electrochemical measurements of this doctoral study.

1.2.2 Critical Parameters of ECWS

ECWS is an uphill reaction, which can be observed from $\Delta G^0 > 0$. Therefore, an efficient catalyst is becoming critical and necessary for reducing the kinetic barrier to driving ECWS effectively(Figure 1. 5)[15]. To compare the catalytic efficiency of catalysts, some critical parameters play an important role (Figure 1. 6). The catalytic performance was evaluated by overpotential (η), Tafel slope (T_s), stability, and electrochemical active surface area (ECSA).

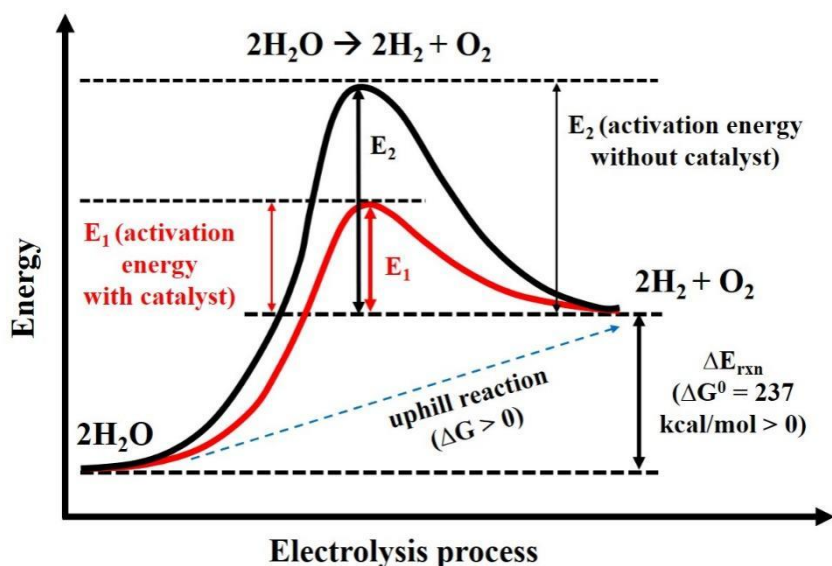


Figure 1. 5 The illustration of the role of the catalyst in the electrolysis progress.

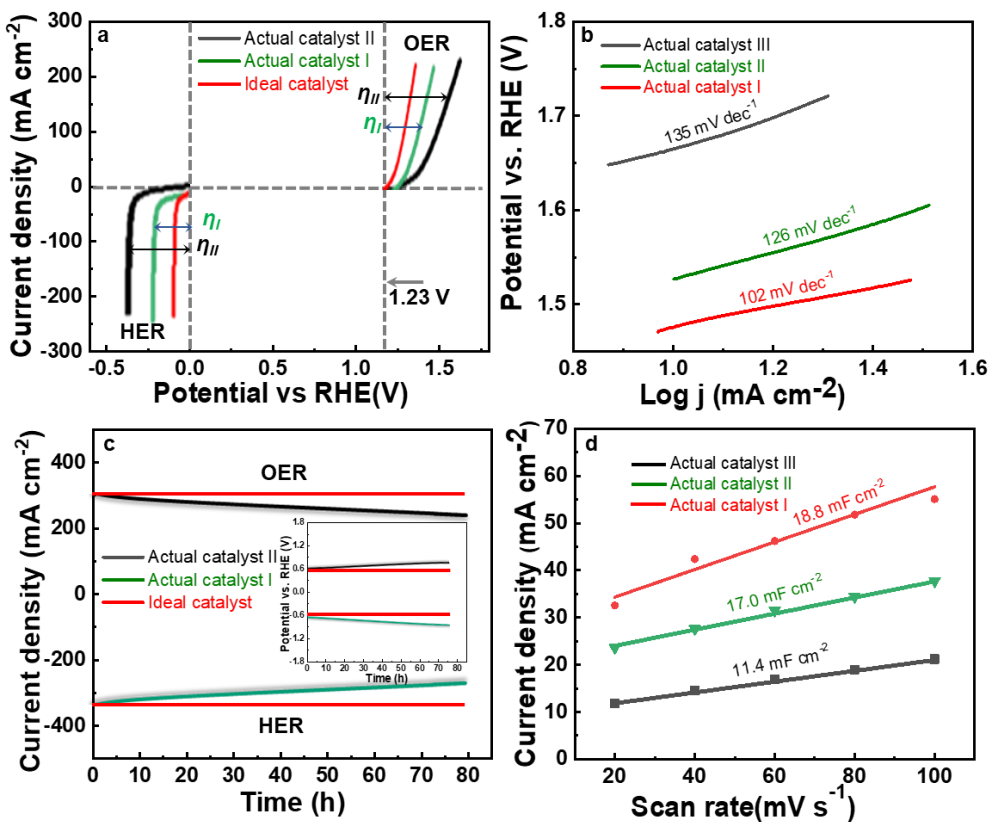


Figure 1.6

Figure 1. 6 Illustrations of critical parameters of ECWS. (a) Overpotential, (b) Tafel slope, (c) Stability in terms of I-t (inset: E-t), and (d) Electrochemical active surface area (ECSA).

The T_s is another key parameter to characterize the performance from the overpotential against the kinetic current, which is described by the Eqn. 1.6:

$$\eta = a + T_s \times \log J_c \quad (\text{Eqn. 1.6})$$

where ‘ a ’ denotes a constant, ‘ T_s ’ denotes Tafel slope, and ‘ J_c ’ denotes current density. In **Figure 1. 6b**, it is observed that the linear correlation between η and $\log J_c$, denoting J_c change as a function of η varies. A smaller T_s suggests faster kinetics of ECWS and a better catalyst.

In practice, there is another critical parameter to characterize the catalyst. Longer stability is expected for a superior catalyst. Typically, two different strategies were performed to express the

stability of one catalyst, which were chronopotentiometry (E-t plot) and chronoamperometry (I-t plot) (**Figure 1. 6c**). The increment of current or potential with time under a fixed potential or current is recorded in the stability test. Usually, researchers set a $J_c \geq 10 \text{ mA cm}^{-2}$ for dozens of hours to evaluate the stability of the catalyst. The more negligible decay of the recorded potential or current, the more stable the tested catalyst.

To investigate the surface activity of a catalyst, ECSA is necessary to be measured. The bigger ECSA, the better catalytic activity. When a catalyst is deposited on an electrode surface, it can be recognized as a capacitor including a double-layer between catalyst film and electrolyte. Double-layer capacitance (C_{dl}) was determined by utilizing cyclic voltammetry (CV) measurement in a non-Faradaic potential area with the following equation:

$$i_c = \nu C_{dl} \quad (\text{Eqn. 1.7})$$

where ' i_c ' denotes the current, ' ν ' denotes scan rate. Then, ECSA is correlated with ' C_{dl} ' (**Figure 1. 6d**) which suggests the amount of active catalytic atoms and may be determined using the following calculation:

$$ECSA = C_{dl} / C_s \quad (\text{Eqn. 1.8})$$

where ' C_s ' denotes a specific capacitance of the electrode and varies in different electrolytes. In this work, C_s is taken as 0.04 mF cm^{-2} . Hence, it is easy to summarize the bigger C_{dl} , the bigger ECSA due to the positive proportional relationship between C_{dl} and ECSA.

1.2.3 Mechanisms for ECWS

As aforementioned, ECWS converts electricity to chemical energy in form of H_2 , a sustainable, renewable, and CO_2 -free fuel. It includes anodic reaction (OER) and cathodic reaction (HER). The anodic reaction is a proton-coupled process with sluggish kinetics and acts as the bottleneck of the overall catalytic process.[16] To solve this issue, a deep understanding of the mechanism is required. As shown in **Figure 1. 7**, the OER and HER occur in different steps under different media. In the case of OER which is located on the left part of the figure, it displays two reaction circles: the inner circle includes the reactions which happen in the alkaline condition and the outer circle includes the reactions which happen in acid conditions. To note, 'M' stands for active metal sites, 'MOH' stands for metal-hydroxide, 'MO' stands for metal oxide with one-electron oxidation of MOH, 'MOOH' stands for an intermediate which results from the OH^- attacks MO,

and lastly, two MO are combined to produce O₂ and M. The mechanism of OER under acid medium is also expressed in the outer circle which displays immediate such as ‘M’, ‘MOH’, ‘MOOH’ and ‘MO’. MO reacts with H⁺ instead of OH⁻ in an alkaline medium [17]. For HER which is located on the right side. Under the alkaline condition, the H₂O molecule absorbs electrons to provide adsorbed H deposited on the metal M (labeled as MH_{ad}), and two H_{ad} can be combined to create H₂. In addition, the only difference for the acid case is H₃O⁺ which is consumed instead of H₂O[18].

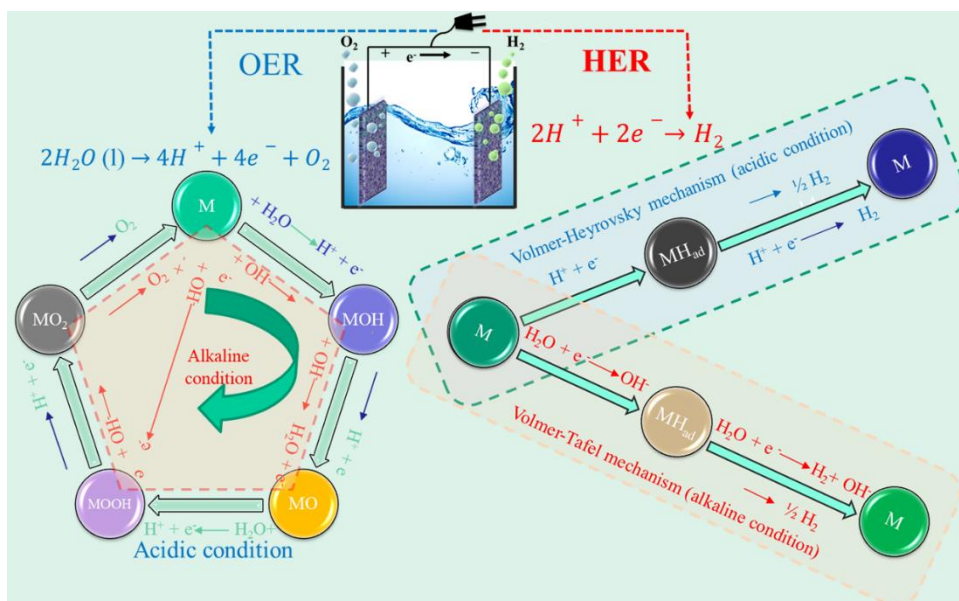


Figure 1. 7 Simplified illustrations of the mechanism of ECWS.

1.3 Catalysts Based on Transition Metal Compounds (TMC)

ECWS is one type of potential strategy for the provision of sustainable energy resources including H₂/O₂ production in the field of rechargeable energy devices[19]. Based on recent research, RuO₂/IrO_x and Pt are the only efficient materials for OER and HER of ECWS[18]. These noble catalysts are relatively precious, rarely found, and suffer stability in the environment. Therefore, the exploitation of non-noble, earth-abundant, active, and stable catalysts for ECWS is of utmost importance. So far, great attention has been attracted to TMC due to its excellent features such as being earth-abundant, readily available, and low-cost. Various TMCs including

transition metal hydroxides,[20] oxides,[17] and selenides[21] have been used as electrocatalysts for ECWS in an alkaline medium. Among them, cobalt hydroxide, manganese hydroxide, cobalt manganese layer double hydroxide, cobalt oxide, manganese oxide, cobalt manganese spinel-type oxide (Co_2MnO_4), nickel, and cobalt diselenide (NiCoSe_2) are reported as promising and effective electrocatalysts for ECWS due to their superior performance, high efficiency, and good stability in 1 M KOH.[22]

1.3.1 Literature Review for TMC

Most of the highly efficient catalytic materials used in electrolyzed water technology that has been researched and developed by their predecessors. In general, Pt, and $\text{RuO}_2/\text{IrO}_2$ were the benchmark for HER and OER, respectively. These materials not only have limited reserves but are also quite a high cost.[23–25] Recently, researchers speculate that the oxides, hydroxides, sulfides,[26] phosphides [27–29], and selenides[30–32] of Ni, Co, and Fe have high theoretical catalytic capabilities due to they belong to the same group as Ru, Ir, and Pt.

Among the various TMCs (**Figure 1. 8**), layered double hydroxide (LDH) is particularly attractive and has been recognized as the superior candidate for alkaline ECWS[33–35]. The catalytic efficiency of these materials can be improved by controlling the shape of nanostructures [36]. Komal and her co-workers prepared Ni-Co LDH nanowires through the HT method [35]. The high catalytic performance was the consequence of a relatively open LDH structure that allowed access to abundant active sites resulting in faster electron transfer [37,38]. Zhou et al. developed a catalyst with heterojunction that has a very low overpotential ($\eta_{10} = 209 \text{ mV}$)[39]. $\text{CoNi}_2\text{S}_4@\text{NiMn-LDH}$ have good performance and a low overpotential ($\eta_{100} = 269 \text{ mV}$) [40]. However, LDH with low conductivity is negative for charge transfer [41–43]. Additionally, bi- or multi-metallic transition metal-based oxides (TMO) exhibit better performance as compared to that of a single component [44,45]. Some successful studies have been achieved[46–49]. This includes spinel transition metal-based oxides (e.g. NiMn_2O_4 ,[50] FeCo_2O_4 ,[51] CoMn_2O_4 ,[52]

Co_2MnO_4 [53]). For instance, Menezes and co-workers synthesized nickel-manganese oxides with predesign ratios of Ni: Mn to boost the efficiency of OER[54]. K. Lankauf et al. prepared the Mn-Co oxides with a low overpotential ($\eta_{10} = 327$ mV)[55]. Similarly, Peng and co-workers reported NiCo_2O_4 with a lower overpotential ($\eta_{10} = 280$ mV)[56]. However, the overpotential and electronic resistance could be decreased to further improve the catalytic activity.

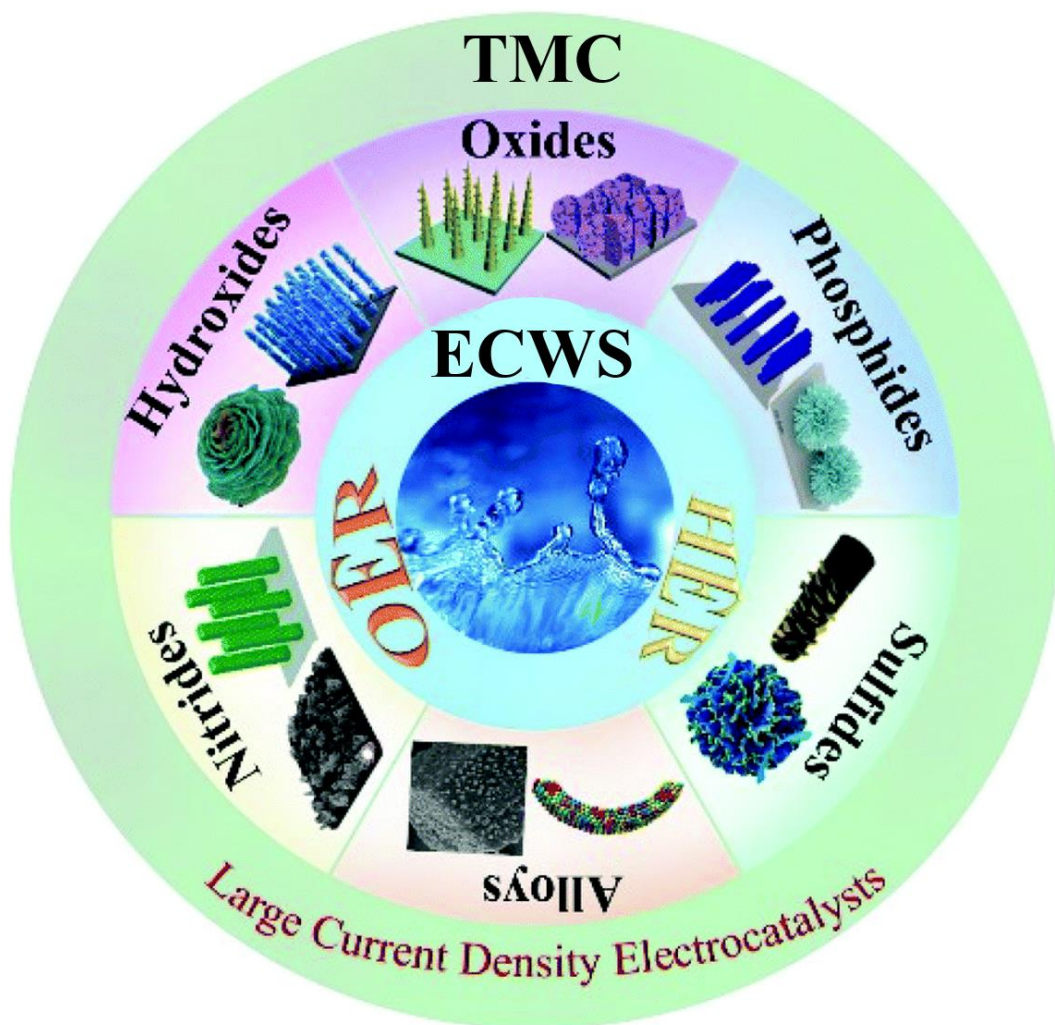


Figure 1. 8 Electrocatalysts based on TMC for ECWS[57].

1.3.2 Strategies to Boost Electrocatalytic Performance of TMC

Despite nanostructured TMC exhibiting a large ratio between the surface area and volume, fast charge separation and transport, catalytic properties, and long-term stability are required. Developing ways to boost the electrocatalytic performance of TMC with chemical stability, abundant active sites, and favorable adsorption energy on the surface has been attracting the attention of researchers. As previously reported, the ways to improve the catalytic activities of catalysts are explained as follows:[58–60]

- i) core-shell nanostructure formation;
- ii) hierarchical nanostructure;
- iii) heteroatomic doping;
- iv) cocatalyst with protective layers;
- v) nanocomposite formation;
- vi) noble metal decoration.

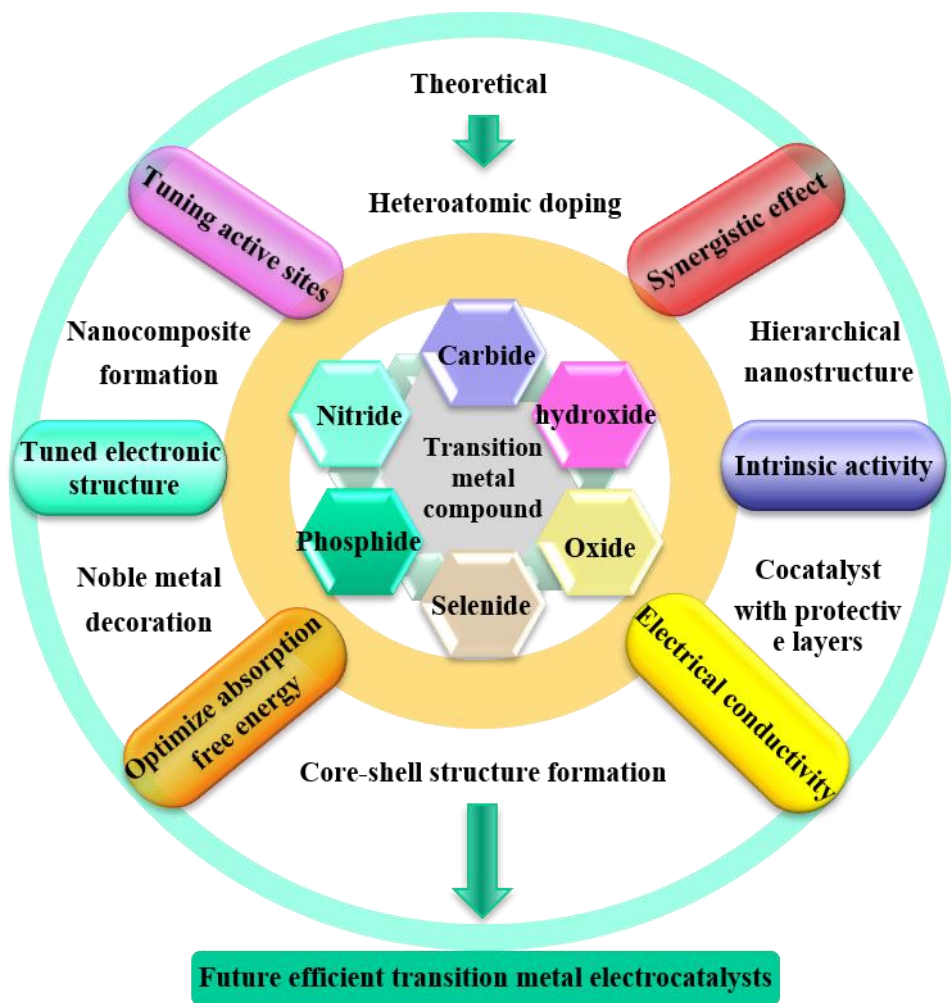


Figure 1. 9 Strategies for obtaining efficient transition metal electrocatalysts.

1.3.3 TMC Investigated for ECWS in This Research Work

Fundamental studies play a significant role in primary research by contrasting the research of leading companies in the corresponding field to develop techniques that can be utilized to develop catalysts with high efficiency and superior performance. Evaluating new catalysts that bear potential for ECWS is very interesting and expected in basic research programs.

New catalysts based on TMC and some previously reported TMC have been utilized as reference catalysts. They are investigated and collected in this work as recorded in **Table 1. 2**.

Table 1. 2 New catalysts based on TMC and reference catalysts.

Type	New catalysts	Reference catalysts
Transition metal hydroxides (TMH)	CoMn-LDH@Ni(OH) ₂	Bare NF Series of CoMn-LDH
Transition metal oxide (TMO)	Iron-doped cobalt manganese oxide (CoMnFeO ₄)	Bare NF Cobalt oxide, Manganese oxide Series of CoMn-O ₄ Series of Fe- Co ₂ MnO ₄ Series of NiMn-O ₄ Series of FeMn-O ₄

1.4 Methodologies Used for Deposition of TMC

In our research, we proposed HT, ED, and chemical bath deposition (CBD) routes to fabricate TMCs such as TMH and TMO with different nanostructured morphologies. Thereby, the overall fabrication process of TMC could be primarily divided into two steps (further discussed in the following chapters). Firstly, the formation of fundamental catalysts; secondly, improving the catalytic activity by using the ways of a hierarchical nanostructure, core-shell nanostructure formation, and heteroatomic doping. We followed these methods for the synthesis of TMC and found outstanding results concerning application and properties.

1.5 Objectives of This Thesis

Globally, the energy crisis is rising. The critical question is how to fulfill the energy demand without causing an environmental problem. This reflects the requirement for sustainable, renewable, and affordable energy resources that can provide carbon-free energy. If the energy needed to drive electrolysis is provided by sustainable energy resources, then ECWS would bear

the potential to fulfill these requirements. Electrocatalytic H₂ production is a challenging subject because of the issues encountered in the process of ECWS, where efficient and stable electrocatalysts are still needed to make an entire process more economically accessible. Based on the recent literature on the development of different nanostructures for ECWS, the main objectives of the research work are as follows:

- (1) Development of nanostructured earth-abundant electrocatalysts for OER and HER reactions via simplistic synthetic routes
- (2) Study their physico-chemical properties to understand their electrocatalytic performance. Also, to study the influence of various preparative parameters on surface structure, oxidation states, physical, and other chemical properties in concerns with used deposition method.
- (3) Rational design of novel catalysts possessing enhanced catalytic performance by fine-tuning the aforementioned characteristics.

Specifically, this work gives insights into the synthesis of TMC-based nanostructured electrocatalysts to understand ECWS by heterogeneous catalysis, for the production of sustainable hydrogen fuel. The following points have been used as guidelines for this research work:

- (1) Synthesize and characterize core-shell nanowires of CoMn-LDH@Ni(OH)₂ catalysts via the HT method. Study the effect of preparative parameters such as solution concentration, and metal molar ratio on the chemical and electrical properties of the obtained catalysts.
- (2) HT deposition of nanowire-nanosheet-like dual structured CoMnFeO₄ catalyst on NF substrate. To investigate the formation mechanism behind CoMnFeO₄ catalysts and the influences of various synthesis parameters e.g. Fe concentration, atmosphere conditions, annealing temperature, and time on their growth and catalytic properties.
- (3) Study the stability of obtained electrocatalysts during catalytic activity and unravel the reason behind performance improvement.
- (4) Compare the different OER and HER performances of obtained electrocatalysts to connect the properties of the catalysts with studied parameters, finding the correlation between them to open new outlooks.

To accomplish the above-stated objectives, this research consists of five main chapters. The first chapter proposed the research background, as TMC-based nanostructured electrocatalysts are chosen here as the active material owing to their high catalytic activity and earth-abundant nature. Chapter two described the advanced synthesis and characterization techniques used in this study. Physical characterizations and performance evaluation of the catalyst materials in terms of OER, HER, and ECWS have been evaluated in chapters three and four, respectively. Chapter five presents the main conclusion and future work. The ultimate goal is to contribute to higher energy efficiency in ECWS for the utilization of sustainable energy sources.

1.6 Flow Chart of This Research Work

Herein, we aim to fabricate new catalysts based on TMC via HT, and ED. The formation mechanism of catalysts based on TMC will be discussed by analyzing multiple characterization techniques e.g. XRD, Raman, FTIR, XPS, FE-SEM, EDS, and TEM. In addition, the overpotential, Tafel slope, ECSA, stability, EIS, MA, and SA properties will be investigated. As shown in **Figure 1. 10**, describes the overall objectives of the whole research process. The details of the main materials which were used to synthesize new TMC have been attached in Appendix “A”. Further, Appendix “B” contains a list of all instruments used to characterize the microstructure and properties.

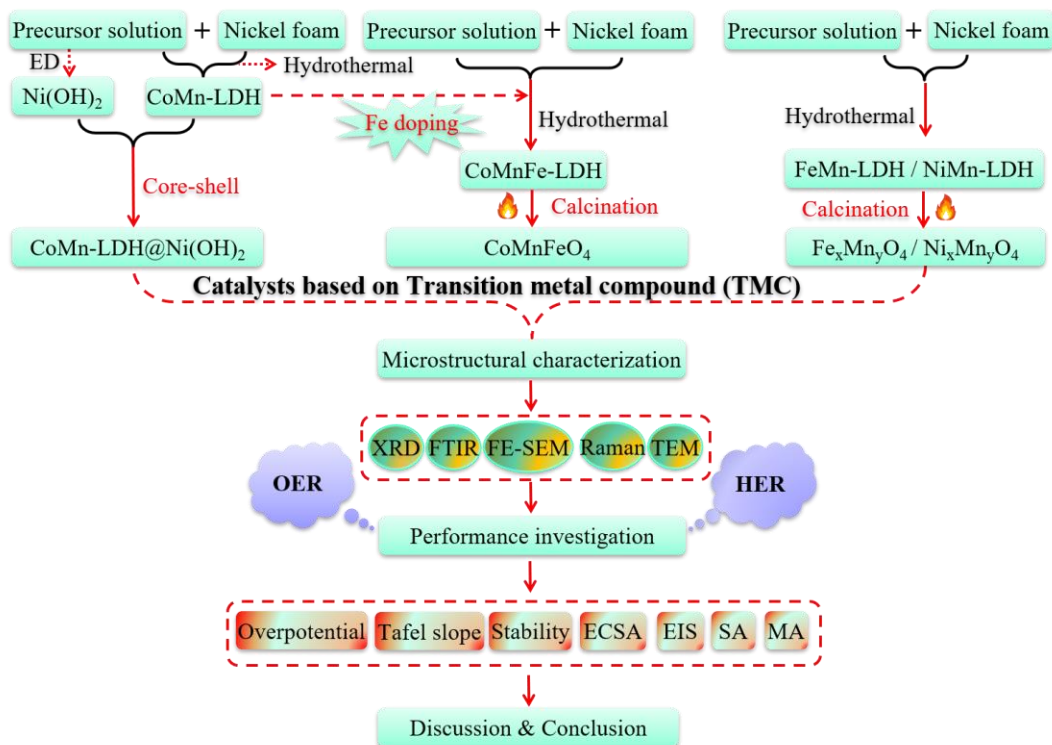


Figure 1. 10 Flowchart illustrating the whole work.

2. Synthesis and Characterization Techniques

2.1 Synthesis of TMC

Nanostructured material is greatly attractive owing to its exclusive physicochemical properties and viability in the field of ECWS. The outstanding electrocatalytic activity of nanostructured catalysts results from the following reasons: i) abundantly exposed surface atoms and catalytic active sites; ii) easily achievable defect and structural engineering; iii) rapid charge transfer. These unique properties of nanostructured catalysts have attracted researchers' great attention to the synthesis of such TMC-based-catalysts. Consequently, several different synthesis routes e.g. the HT method, ED, and CBD have been adopted to obtain nanostructured catalysts with unique morphologies (such as nanowires, nanosheets, and nanospheres) and tailored properties.

Nanostructured TMC can generally be produced by different basic techniques including the top-down and bottom-up approaches which consist of assembling atoms to produce macroscopic materials with the merits of control over crystallite size and/or morphology (**Figure 2. 1**). Among bottom-up approaches, the most common chemical approaches e.g. HT method, ED, as well as CBD have been employed due to their low-cost, high efficiency, and easy operation. Consequently, the details of these approaches are displayed in the following sections.

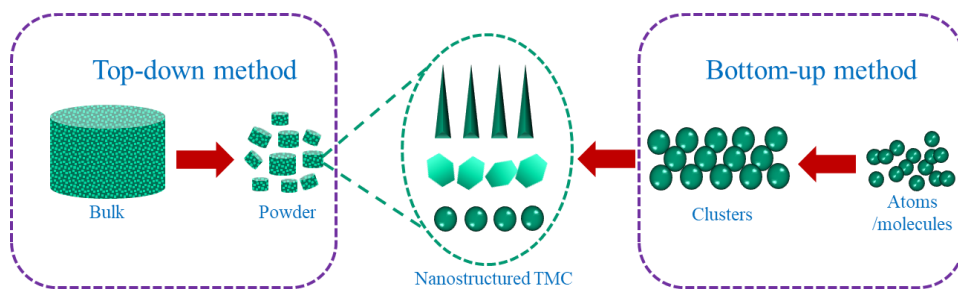


Figure 2. 1 The two basic approaches used for the synthesis of nanostructured TMC.

2.1.1 HT Method

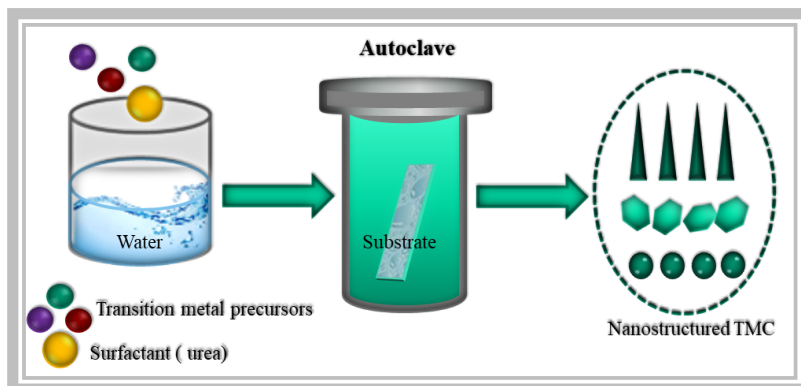


Figure 2. 2 Schematic of the HT method.

An HT method is a large pressure solution-phase fabrication in which H_2O is used as a solvent and an autoclave as a reaction vessel.[61] A schematic of the HT method is displayed in **Figure 2. 2**. To control the morphologies of the catalysts, various parameters such as precursor molar concentration, reaction time, temperature, and surfactant type can be employed according to the types of the main component during the chemical reaction. In addition, nanostructured TMC can be prepared with certain morphology, size, and composition by using different types of surfactants (such as urea, and acetyl alcohol) and modifying the reaction temperature and/or time. There are significant successes in preparing nanostructured TMCs by using this technique. M. L. M. Napi et al. successfully deposited nanoneedles like structured fluorine-doped zinc oxide films by fine-tuning the reaction time and bath temperature of the HT reaction.[62] L. Ma and coworkers discussed the influences of Co concentration on the $ZnMn_2O$ nanocrystals which were prepared with hollow nanospheres by using HT synthesis.[63]

2.1.2 ED method

ED is an economically and technologically viable technique to prepare void-free TMC as thin film by depositing nanostructured material onto conductive substrates (e.g. NF, copper foam, stainless steel, and FTO glass) from a precursor solution.[64] ED has several merits over other nano-processing approaches as follows: [65] i) low cost; ii) wide-scale application for the preparation of pure metals and composite nanomaterials; iii) high synthesis rate; iv) easy technology transfer between laboratory and industries; v) easy to control the morphology (especially the thickness) and composition of the thin film. As shown in **Figure 2. 3**, there are

three electrodes in a typical ED setup, including a reference electrode (RE), a counter electrode (CE), and a working electrode (WE). These electrodes are assembled into a potentiostat. Then, the WE is immersed in the precursor solution with a certain electric field applied to transfer electrons to ions. Consequently, uncharged molecules were deposited on the surface of a substrate. Many works of literature reported the successful synthesis of nanostructured TMC by using ED. E Hatami et al. fabricated an active Ni-Fe thin film on a copper substrate with a unique structure of nanocones. [66] Hao Feng et al. fabricated Co-Fe layered double hydroxide nanosheets which significantly boost the OER performance of CoP nanowires. [67]

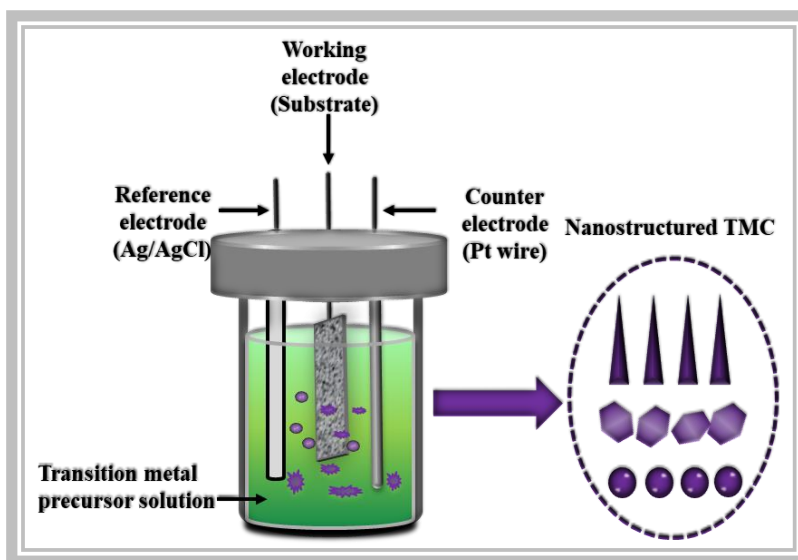


Figure 2. 3 Schematic of ED method.

2.1.3 CBD Method

CBD is another economically and relatively simple technique to produce nanostructured TMC as coating or other by depositing nanostructured material onto a conductive substrate (e.g. NF, copper foam, and stainless steel). There are many merits of CBD which include low temperature, low cost, gentleness, and greenness. [68] Typically, CBD occurs at a relatively slow reaction rate of 1~10 nm/min to form a thin film or the other solid product on a substrate. [69] Hence, this technique is more suitable for thin-film synthesis. In addition, the CBD system is relatively simple, does not require high-cost accessories or a strict vacuum atmosphere, and only needs a hot plate with/ without a magnetic stirrer. The chemical reaction also occurs in dissolved precursor solution at a low temperature of 30~80°C. [70] **Figure 2. 4** illustrates the schematic of

CBD. Herein, a precursor solution is stirred and heated by using a hot plate. Consequently, the thin film is formed through the following steps: i) formation of ionic species; ii) carriage for created ions; iii) ions deposition on the substrate. Besides, the morphology, structure, and properties of TMC can be modified by tuning deposition time, bath temperature, molar concentration, and pH of precursor solution [71].

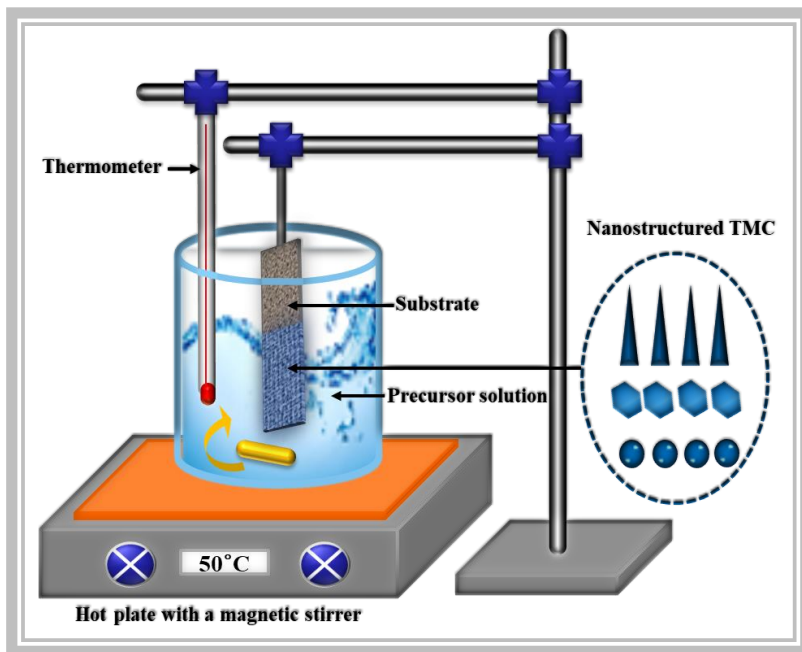


Figure 2. 4 Schematic of CBD method.

2.2 Advanced Characterization Techniques

2.2.1 XPS

XPS is a common and simple quantitative spectroscopic system for measuring the valuable elemental composition and chemical state of their elements in the solid material. With the help of monoenergetic X-rays, the sample is irradiated and analyzed by measuring the escaped electrons and their kinetic energy. Moreover, such kinetic energy is detected and the intensity can provide the information of concentration for the tested elements. But there is a limitation of the sample investigation thickness (< 20 atomic layers of sample surface) owing to photoelectrons

with a short non-elastic free path (< 5 nm).[72]

To examine the surface chemical state of catalysts based on TMC, samples before and after the catalytic chemical reaction were characterized by XPS. These XPS analyses were verified with a VG Multilab 2000 instrument (1253.6 eV for monochromatic radiation of Mg $K\alpha$, Thermo VG Scientific, U.K.).

2.2.2 XRD

To compare crystallographic information of nanostructured catalysts, XRD was carried out on the as-prepared catalysts. It is a destruction-free technique, which uses the elastic scattering of X-rays. A brief description of the principle of XRD is as follows.[73]

X-rays, when an incident, are scattered by the electrons of the atoms of a crystalline material in which the atoms are arranged in a regular pattern. Moreover, the distance between the atomic facets is comparable to the wavelength of X-rays. As the result, the scattered X-rays interfere either constructively or destructively. Diffraction is due to the distance between planes, which is unique to a particular material. This unique inter-plane spacing gives the diffracted X-rays a unique characteristic angle.

In this work, X'pert PRO is used to record the XRD diffraction patterns (Philips, Eindhoven, Netherlands) at 40 kV and 30 mA radiation of Cu $K\alpha_1$, with a wavelength of 0.154060 nm and a scanning angle of 5° – 80° with a step of 0.02° .

2.2.3 FE-SEM

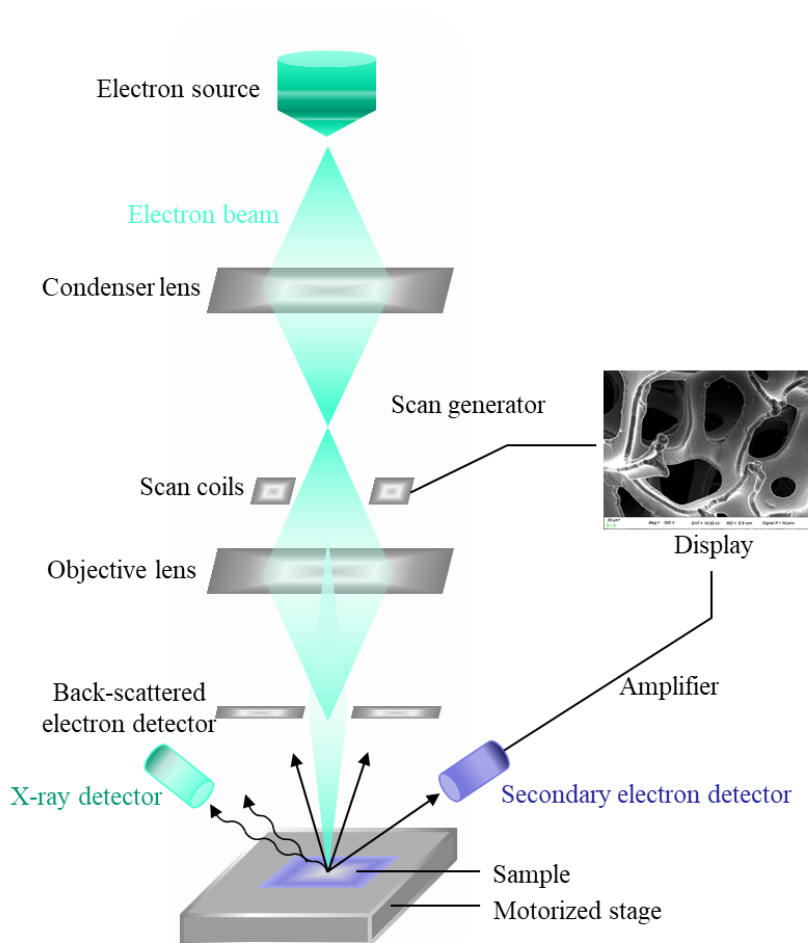


Figure 2. 5 Schematic of FE-SEM [74].

In FE-SEM, high-energy electron beams are used to scan the surface of a sample under vacuum conditions.[75] This technique is been widely used to examine the quality, morphology, crystal orientation, as well as composition of the investigated material. FE-SEM can provide images in the range of a few nanometers to micrometers with a high spatial resolution of 50~100 nm by using an accelerating voltage of electrons of 5~20 kV.[76] A typical FE-SEM system is shown in **Figure 2. 5**. To confirm the morphology of as-prepared catalysts, FE-SEM images were verified by utilizing a microscope of JSM-6701F (JEOL, Japan).

2.2.4 TEM

The TEM is critical electron microscopy in which TEM images are mainly obtained from ultrathin specimens using the transmitted signals. The high resolution of TEM (atomic scale) results in the development of a major analytical method in many research fields, including biomedical science, materials science, chemistry, biology, and paleontology[77]. Higher magnification resolution information can be given by TEM in terms of multi-direction, while there are some certain limitations: i) the procedure of sample preparation is particularly difficult and time-consuming; ii) the sample will be damaged during the measurement; iii) the local information only about selected spot of the sample can be obtained. In this work, TEM images were verified by an instrument (JEOL-3010, 300 kV of accelerating voltage), and a copper grid was used for sample preparation. EDS is a common technique that was applied to study chemical constituents of catalysts. Typically, an EDS setup consists of four basic units, an electron beam, an excitation source, an analyzer, and a pulse processor.

2.2.5 Raman Spectroscopy

Raman spectroscopy has become the most useful way to probe the vibrational modes of catalysts' molecules. It is also called Raman scattering due to relying on the inelastic scattering of photons. Usually, single-wavelength light involving laser in visible, near-ultraviolet/-infrared, even x-ray is performed. In Raman spectroscopy, laser light is used to excite the material, then the electromagnetic energy is captured by the objective lens and delivered to the monochromator. The elastic scattering related to Rayleigh scattering was filtered out on the detector by a notch filter.[78] In this work, the Raman spectrum was performed by a spectrometer of Horiba Jobin-Yvon LabRAM HR 800 UV, and an excitation source of 532.0 nm Ar-ion laser. In addition, the laser power is modified with 5.4 mW, the objective lens is attuned towards 100 \times and a resolution of 0.28 cm^{-1} in 100-1000 cm^{-1} is employed.

2.2.6 FTIR

FTIR is a single-beam device in which the transmission spectrum has been obtained via rationing a single beam spectrum of the material against that of the background. [79] These two spectra have been produced precisely by figuring out the Fourier transform which results from their corresponding interferograms. [80] In this thesis, the FTIR was performed by PerkinElmer Spectrum 10.5.2 system at $400\text{--}4000\text{ cm}^{-1}$.

2.3 Electrochemical Characterization

2.3.1 Linear Sweep Voltammetry (LSV) Measurement

LSV is a common technique involving a single linear sweep from lower to higher potential limit (**Figure 2. 6**). This is helpful for an irreversible system in which a reverse sweep can't reveal enough information.[81] Generally, the electrochemical system included two-electrode and three-electrode cells which compose of a CE, WE, and RE. These electrodes are assembled to a potentiostat with a medium. The potentiostat controls potential and records the current of the CE from which a curve of potential against the current can be plotted. A dip or peak is observed at the potential in which reduction/oxidation starts. LSV is utilized to estimate the current on the peak, the potential to deliver half-peak current, and peak current.[82]

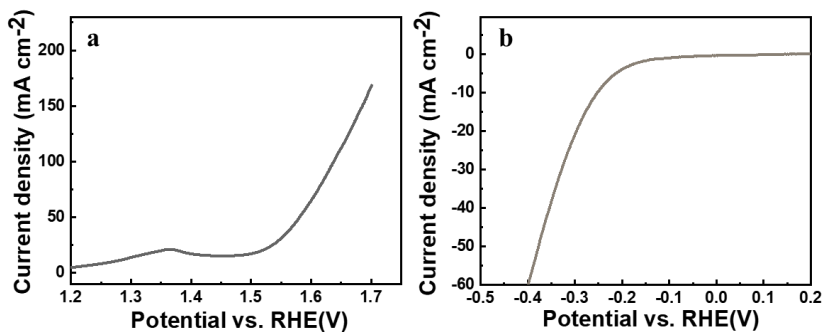


Figure 2. 6 LSV plot of (a) OER and (b) HER.

2.3.2 CV Measurement

CV is a simple electrochemical measurement that reveals evidence related to the electric performance of the catalyst in a cell and evaluates electrode kinetics. A characteristic CV curve is illustrated in **Figure 2. 7**. Some researchers have extended the theory of CV to include electron transfer chemical reactions. Results of these theoretical calculations resulted in using CV possibly to evaluate constants of the standard rate for electron transfer.[83] In a CV measurement, a ‘cyclic’ sweep of potentials involves half cycle-potential from a predetermined beginning potential to a switching value and another half-cycle-potential from a reverse scan. Thus, the current versus potential plot derived from the value is called a cyclic voltammogram. Moreover, the shape of the cyclic voltammogram extremely depends on the experimental conditions and analytes concentrations. By tuning the factors, CV can provide information related to the stability of TMC oxidation rate, and reversibility of the electron transfer chemical reaction.[84]

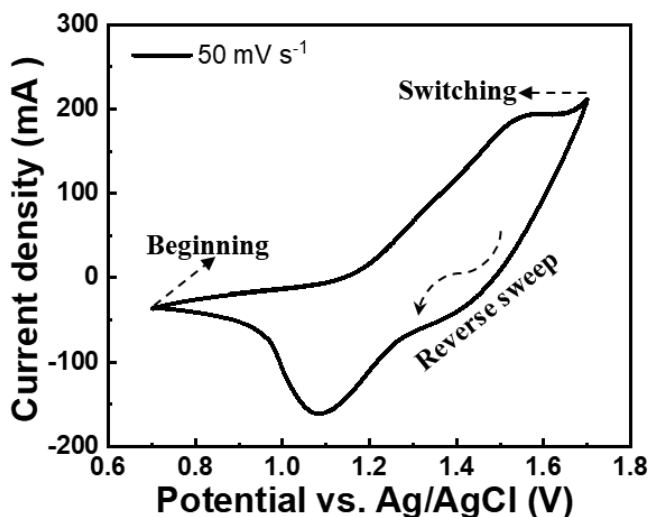


Figure 2. 7 A typical CV curve.

2.3.3 EIS Measurement

EIS is an effective, and simple system for evaluating ECWS cells' performance. Indeed, a quantitative explanation of the impedance data can be gained by utilizing significant equivalent circuits. When using such systems, the generation of maximum power has limitations due to their relatively high internal resistance. [85] The influence of such various resistances on the total internal resistance is determined by using EIS measurement, which is significantly essential for the engineering of efficient electrocatalysts for better performance. EIS has been successfully utilized in many ECWS research for the development of many novel electrocatalyst designs with greater catalytic activity.[86]

Practically, in the half-cell systems such as OER or HER of ECWS, the catalytic activities are restricted by their internal resistances (anodic or cathodic impedance) which makes it possible to analyze various factors of internal resistance and adopt applicable methodologies to improve the catalytic activity. Moreover, the internal resistance can be analyzed including the resistance

of charge transfer (R_{ct}) and electrolyte solution (R_s) (**Figure 2. 8**). The R_{ct} is the major kinetic limitation. In this thesis, EIS was performed at certain potential conditions within $1 \times 10^{-1} - 1 \times 10^5$ Hz (frequency) and 10 mV (amplitude).

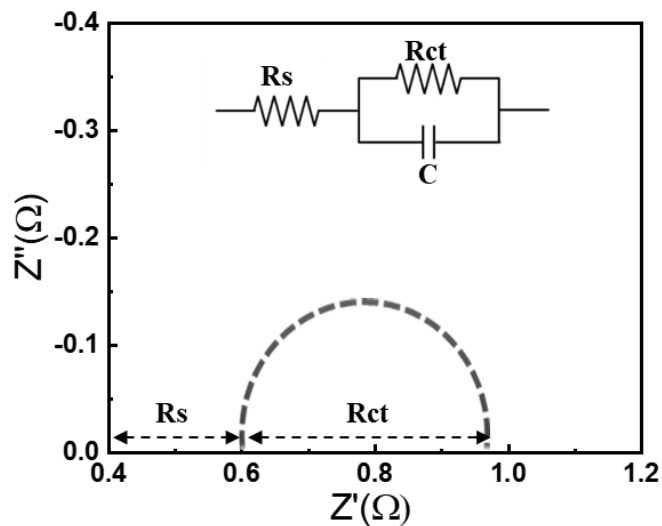


Figure 2. 8 Nyquist plot of EIS and corresponding equivalent circuit model (inset).

3. Synthesis and Characterization of Electrocatalysts

3.1 Substrate Cleaning

Before material fabrication, the rinsing process was carried out to remove the contaminants and oxide layers present on the surface of the substrate, avoiding any damage to it. The cleaning procedure is critical due to the negative effect of the contaminated surface of the substrate on the reproducibility of the experiment. In detail, NFs were cleaned with a 1 mol L⁻¹ hydrochloric acid solution to eliminate the contaminants and NiO_x layer. Then, NFs were placed in ethanol and ultrapure water and rinsed thoroughly under sonication for 15 min each. All the rinsing processes were completed in the ultrasonic cleaner, which provides an efficient cleaning via cavitation effect to get high-quality deposition. Then the catalyst was dried at 55 °C for 5 hours.

3.2 Core-shell Nanowires of CoMn-LDH@Ni(OH)₂ Catalysts

3.2.1 HT Synthesis of CoMn-LDH

To prepare CoMn-LDH, cleaned NFs were immersed in a precursor solution which was contained in the stainless-steel reactor with Teflon lining via a facile HT method. The precursor solution consisted of MnSO₄·H₂O (0.0811 g), Co(NO₃)₂·6H₂O (0.5588 g), ammonia fluoride (0.0844 g), urea (0.7207 g), and 60 mL ultrapure water. And then, the mixture was gently stirred for 20 min by a magnetic stirrer. The sealed reactor was located in a furnace and heated to 120 °C holding for 6 hours. Then, the stainless-steel reactor was cool down to room temperature. The deposited NF was then rinsed using ethanol and ultrapure water three times and subsequently dried at 55 °C for 5 hours. For a comparative study, only Co(NO₃)₂·6H₂O or MnSO₄·H₂O was also a precursor to fabricate Co(OH)₂ or Mn(OH)₂ under the same conditions.

3.2.2 ED Synthesis of Ni(OH)₂

For synthesizing CoMn-LDH@Ni(OH)₂, nickel hydroxide (Ni(OH)₂) was deposited onto the aforementioned resulting NF by a simple ED method. The electrolyte was 70 mL NiCl₂·6H₂O aqueous solution with a molar concentration of 0.1 M and the deposition was obtained under the

cyclic voltammetry technique (CV) in 10 segments at 20 mV s^{-1} by sweeping from -0.4 to -1.3 V. The as-prepared sample was rinsed and dried as aforementioned. The mass loading of the CoMn-LDH@Ni(OH)_2 was calculated by measuring the NF before & after depositing the active materials. For comparative study, only Ni(OH)_2 was also yielded onto NF under similar conditions. **Figure 3. 1** shows the fabrication process of the electrocatalysts.

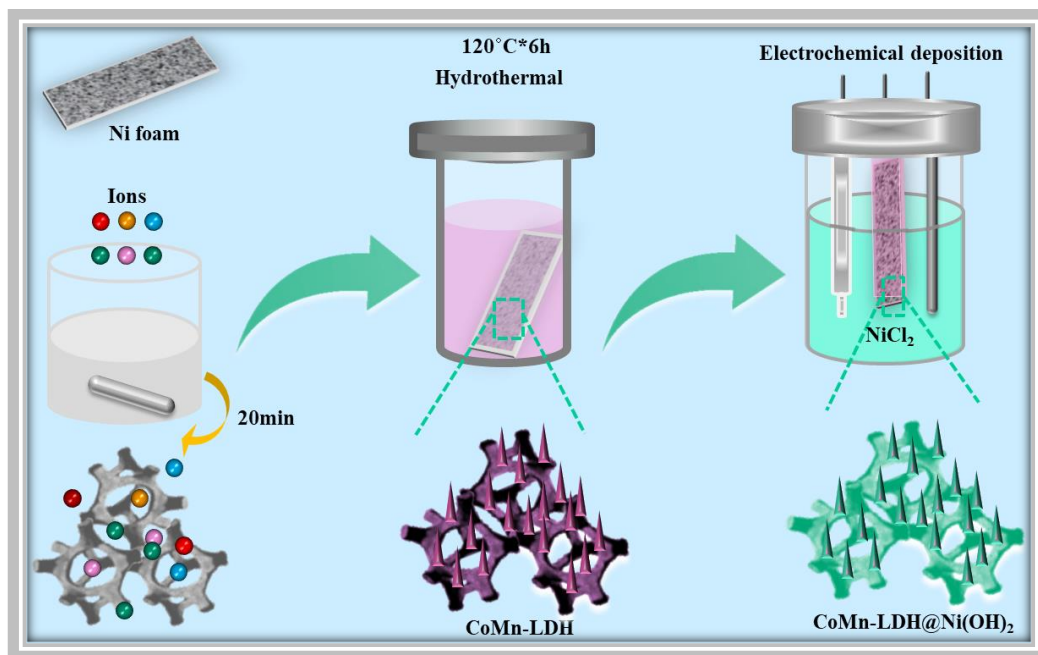
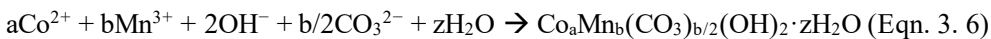


Figure 3. 1 Schematic diagram of synthesis procedures of CoMn-LDH@Ni(OH)_2 .

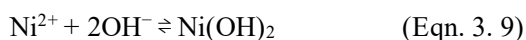
3.2.3 Formation Mechanism

Core-shell nanowires of CoMn-LDH@Ni(OH)_2 were anchored on NF via a facile HT method followed by ED method. During the HT procedure, the possible reactions could be suggested as follows:





When the temperature was raised to 120 °C, the $\text{CH}_4\text{N}_2\text{O}$ started to decompose and released OH^- (Eqn. 3. 1 and 3. 2) [87]. At the same time, ammonium fluoride (NH_4F) occurred in hydrolyzed reaction and provided the F^- (Eqn. 3. 3), reacted with Co^{2+} formed $\text{CoF}_x^{(x-2)-}$ solution. Over time, the hydrolytic reactions of $\text{CoF}_x^{(x-2)-}$ & $\text{CoF}_{x-y}(\text{OH})_y^{(x-2)-}$ occurred (Eqn. 3. 4 and 3. 5). As the reaction progressed, $[\text{CoF}_{x-y}(\text{OH})_y]^{(x-2)-}$ was slowly hydrolyzed to $[\text{Co}(\text{OH})_x]^{(x-2)-}$ producing $\text{Co}(\text{OH})_2$ nuclei, and then grew into the parent particles, which precipitated on the NF substrate. As the $\text{Co}(\text{OH})_2$ parent particles aggregated, then started to crystallize. Subsequently, crystals grew along the c-axis, progressively producing the nanowire's structure [88]. During this time, the Mn^{3+} ions were inserted into the crystal lattice. The Mn^{3+} ions displaced some Co^{2+} ions in the $\text{Co}(\text{OH})_2$ laminates. Finally, CoMn-LDH nanowires were synthesized on the substrate surface (Eqn. 3. 6) [89]. In the electrodeposition step, $\text{Ni}(\text{OH})_2$ was coated onto CoMn-LDH nanowires. The detailed reactions can be described as follows:



Cl^- ions from the NiCl_2 solution were oxidized at the anode surface (Eqn. 3. 7). Before electrons are transported to the CoMn-LDH surface to reduce it to a metal phase, H_2O molecules are reduced to hydrogen and OH^- at the cathode surface [90] (Eqn. 3. 8). Then, OH^- assembled and reached a certain threshold. Driven by the difference in concentration and the electric field force, $\text{Ni}(\text{OH})_2$ was easily fabricated by Ni^{2+} ions at the cathode-electrolyte interface reacting with those excessive OH^- (Eqn. 3. 9).

3.2.4 Structural Analysis

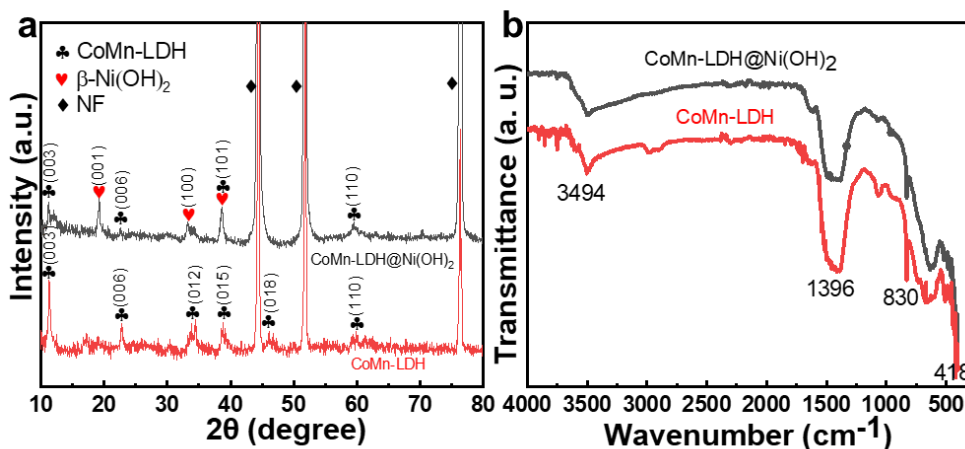


Figure 3. 2 Structural analysis of CoMn-LDH@Ni(OH)_2 and CoMn-LDH : (a) XRD patterns and (b) FTIR spectra.

Figure 3. 2a shows the XRD spectra of the prepared samples. The three peaks around $2\theta = 44.32^\circ$, 51.64° , and 76.33° can be indexed to NF substrate (JCPDS card no. 04-0850)[91]. The other detectable peaks located $2\theta = 11.32^\circ$, 22.34° , 34.42° , 38.91° , 46.62° , and 60.33° match properly with crystal facets (003), (006), (012), (015), (018), and (110) of typical LDH (JCPDS card no. 10-0144), suggesting the CoMn-LDH was successfully deposited on the NF [92]. New peaks at $2\theta = 19.31^\circ$, 32.93° , and 38.94° emerge following ED method peaks which can be indexed well to crystal facets (001), (100), and (101) of $\beta\text{-Ni(OH)}_2$ (JCPDS card no. 14-0117)[93]. In addition, there is a distinct observation of original LDH peaks which decrease in intensity because the mild ED environment results in a little inevitable damage and change to the LDH crystal structure.[94] To investigate the surface functional group for obtained electrodes, the FTIR spectra for them were carried out and exhibited in **Figure 3. 2b**. The peak around $\sim 3494\text{ cm}^{-1}$ is the typical peak of LDH and is ascribed to the O-H stretching mode of water to OH^- species[95]. The peak at $\sim 1425\text{ cm}^{-1}$ is attributed to the intercalated CO_3^{2-} which maybe come from the reactant of $\text{CH}_4\text{N}_2\text{O}$ [96,97]. The peaks associated with the metal oxide vibrational modes of the brucite-like structure are observed around $\sim 830\text{ cm}^{-1}$ and 418 cm^{-1} . Therefore, the presence of the CoMn-LDH@Ni(OH)_2 is further confirmed by the FTIR analysis which coincides with the XRD analysis.

3.2.5 Morphological and Compositional Analysis

FE-SEM and TEM were performed to study the morphology of the as-prepared electrodes. **Figure 3. 3a&b** show a low magnified FE-SEM image of Bare NF, which has an obvious porous structure, stable backbone, and a very smooth surface with a lot of grain boundaries. As displayed in **Figure 3. 3c&d**, it is markedly observed that deposited CoMn-LDH@Ni(OH)₂ is uniformly and densely grown on the NF.

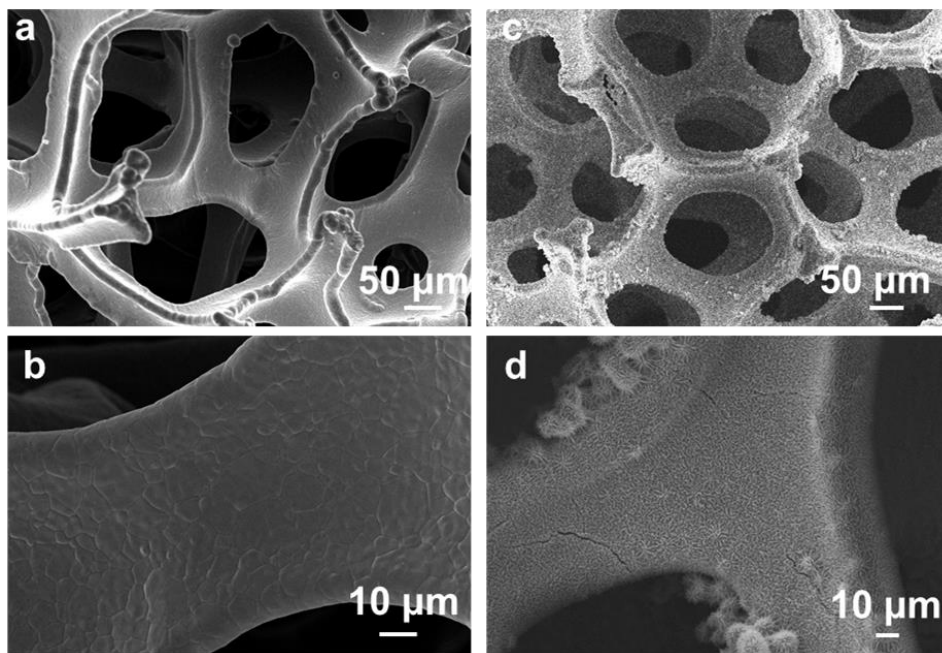


Figure 3. 3 FE-SEM images of (a, b) bare NF and (c, d) CoMn-LDH@Ni(OH)₂.

From **Figure 3. 4(a, b)**, FE-SEM images of the LDH are illustrated. It exhibits orderly aligned nanowires (approximate diameter ~ 40 nm) with a distinctly smooth surface. However, the well-organized nanostructure changes a little with a distinctly rough and fluffy surface from the further electrochemically depositing of Ni(OH)₂ thin film on the CoMn-LDH nanowire (**Figure 3. 4(c, d)**).

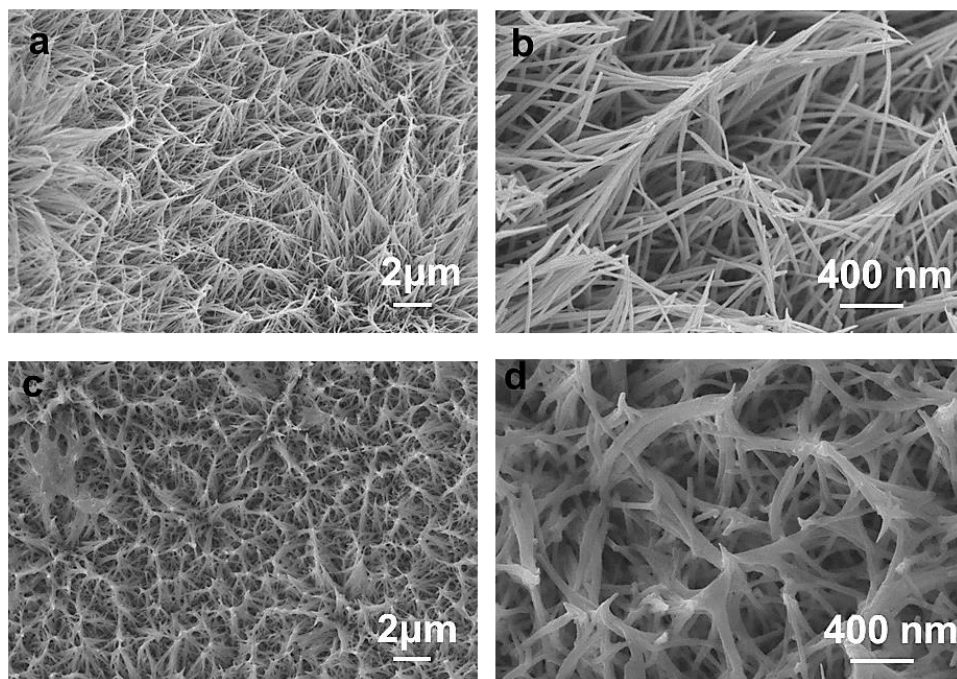


Figure 3. 4 The FE-SEM images of (a, b) CoMn-LDH nanowires; (c, d) CoMn-LDH@Ni(OH)₂ at different high magnifications.

To further determine the nanostructures of CoMn-LDH@Ni(OH)₂, the obtained CoMn-LDH (**Figure 3. 5**) and CoMn-LDH@Ni(OH)₂ samples (**Figure 3. 6**) were estimated by TEM analysis. As shown in **Figure 3. 5a&b**, highly uniform one-dimensional (1D) nanowires with a smooth surface are investigated clearly, which is consistent with FE-SEM analysis. Moreover, the EDS spectrum displays that elements of Co, O, and Mn are copresence in the material, also Co and Mn are in an atomic ratio of ~ 4: 1, matching the molar ratio of precursor. From **Figure 3. 5c**, it is observed that lattice fringes of ~ 0.15 nm and ~ 0.26 nm, indexing to the crystal facets (110) and (012) of the CoMn-LDH [98]. As exhibited in **Figure 3. 5d-g**, there is a homogeneous distribution of Mn, Co, and O over the entire material from the EDS elemental mapping analysis.

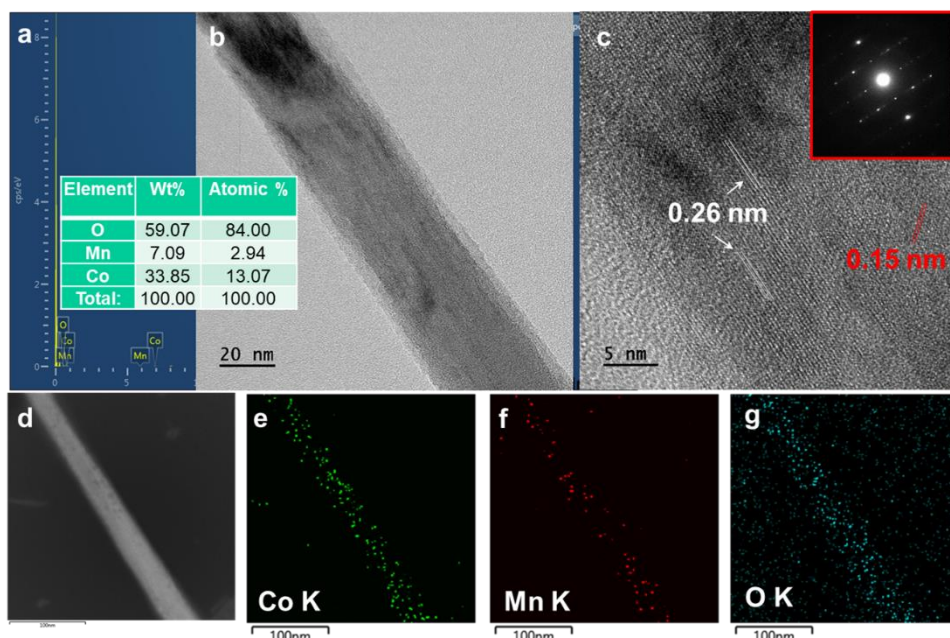


Figure 3. 5 (a) EDS analysis, (b) TEM image, (c) HRTEM image, and (d-g) EDS elemental mapping of CoMn-LDH nanowires.

Figure 3. 6a displays that the 1D morphology is maintained well for the CoMn-LDH@Ni(OH)₂ sample, but the sample's surface emerges with abundant rough and fluffy clouds-like nanosheets (marked with red dotted circles). From **Figure 3. 6b** of a high-resolution TEM (HRTEM) image, the ultrathin Ni(OH)₂ nanosheets (located in the area marked with yellow dotted lines) are present clearly over the surface of nanowires. Besides, an interface between the core (CoMn-LDH) and shell (Ni(OH)₂) was observed distinctly (marked with the black dotted line). Besides, it is observed that lattice fringes of ~ 0.15 nm and ~ 0.26 nm, indexing to the crystal facets (110) and (012) of the CoMn-LDH core[98]. Moreover, Ni(OH)₂ phase has a lattice spacing of ~ 0.23 nm, assigned to the crystal facet (101) [99]. Uniformly arranged spots were distinctly observed in the selected area electron diffraction (SAED) pattern, confirming the polycrystalline nature of CoMn-LDH@Ni(OH)₂ with a uniform distribution of shell (Ni(OH)₂) over the core (CoMn-LDH) [92],[100],[101]. Moreover, the EDS spectrum of CoMn-LDH@Ni(OH)₂ displays that elements of Co, O, Mn, and Ni are copresence in the material, also Co and Mn are in an atomic ratio of ~ 4: 1, matching the molar ratio of precursor (**Figure 3. 6c**). As exhibited in **Figure 3. 6d-h**, there is a homogeneous distribution of Mn, Co, O, and Ni over the entire material from the EDS elemental mapping analysis. In detail, there is a small cloud of

nanosheet near the nanowire which contains the Ni element. It can confirm the presence of Ni(OH)₂(marked with a green line)(as shown in **Figure 3. 6d**). In **Figure 3. 6e&f**, Co&Mn distributes with a relatively smaller diameter, suggesting the CoMn-LDH as the core. While, Ni distributes with a larger diameter in the whole region, suggesting Ni(OH)₂ as the shell (**Figure 3. 6h**). The morphological manipulation of CoMn-LDH@Ni(OH)₂ displays a core-shell structure that provides conduction channels for electron transfer and O₂ release. Therefore, this arrangement may strongly affect the catalytic performance of the catalyst [102].

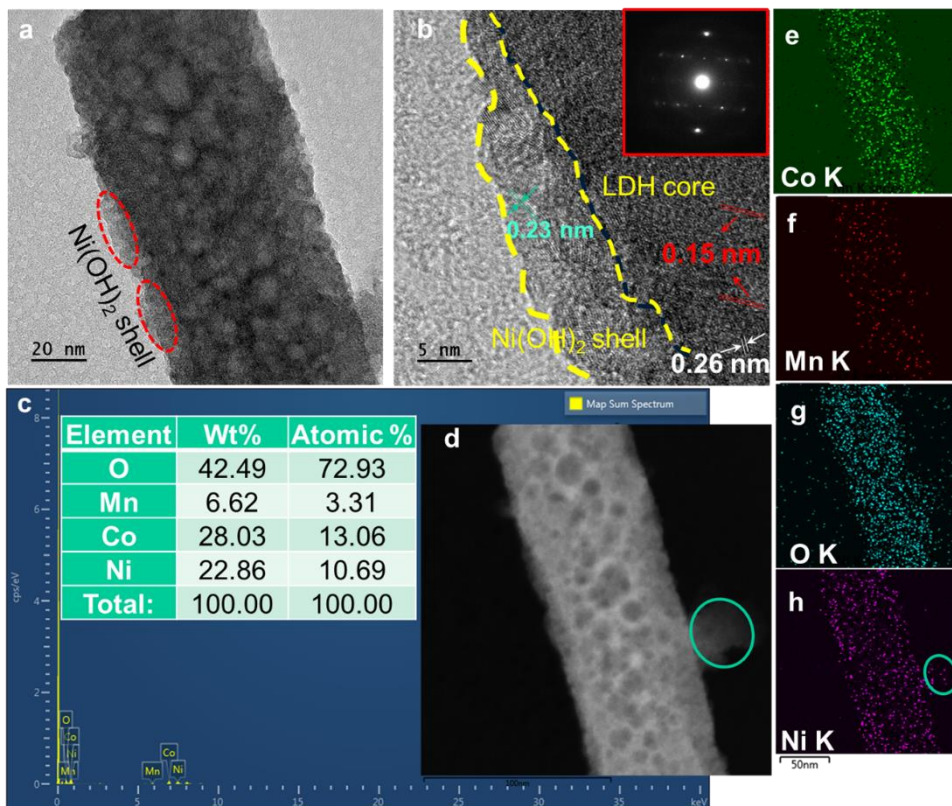


Figure 3. 6 (a) TEM image (b) HR-TEM image (inset: corresponding SAED). (c) EDS analysis and (d-f) Elemental mapping of CoMn-LDH@Ni(OH)₂.

3.2.6 XPS Analysis

From **Figure 3. 7**, the XPS spectra of Ni(OH)₂ are exhibited. The Ni 2p spectrum of Ni(OH)₂ is deconvoluted into 2p_{3/2} (855.3 eV) and 2p_{1/2} (873.2 eV) as displayed in **Figure 3. 7b**. The O 1s spectrum was fitted into two different peaks (**Figure 3. 7c**). The peak located at 530.9 eV is properly matched to oxygen bonding with Ni, while the peak located at 532.5 eV is assigned to

absorbed oxygen in terms of OH^- and CO_3^{2-} at/near the $\text{Ni}(\text{OH})_2$ surface [103].

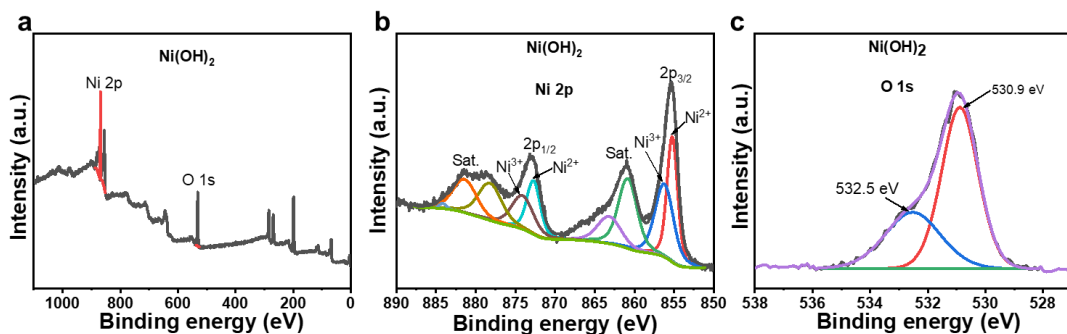


Figure 3. 7 (a) Full scan XPS spectrum of $\text{Ni}(\text{OH})_2$ and high-resolution XPS spectra of (b) Ni 2p, and (c) O 1s.

Figure 3. 8 displays the XPS spectra of CoMn-LDH. The Co 2p spectrum is deconvoluted into $2p_{3/2}$ (781.1 eV) and $2p_{1/2}$ (780.8 eV) (**Figure 3. 8b**). The Mn 2p spectrum shows two different peaks, suggesting the copresence of Mn^{2+} , Mn^{3+} , and Mn^{4+} states (**Figure 3. 8c**)[104,105]. Besides, the O 1s spectrum was fitted into two different peaks (**Figure 3. 8d**). The peak centered at 531.3 eV was assigned to oxygen bonding with Co&Mn, while the peak located at 532.6 eV corresponded to physisorbed & chemisorbed H_2O molecules at/near the sample's surface [106],[103].

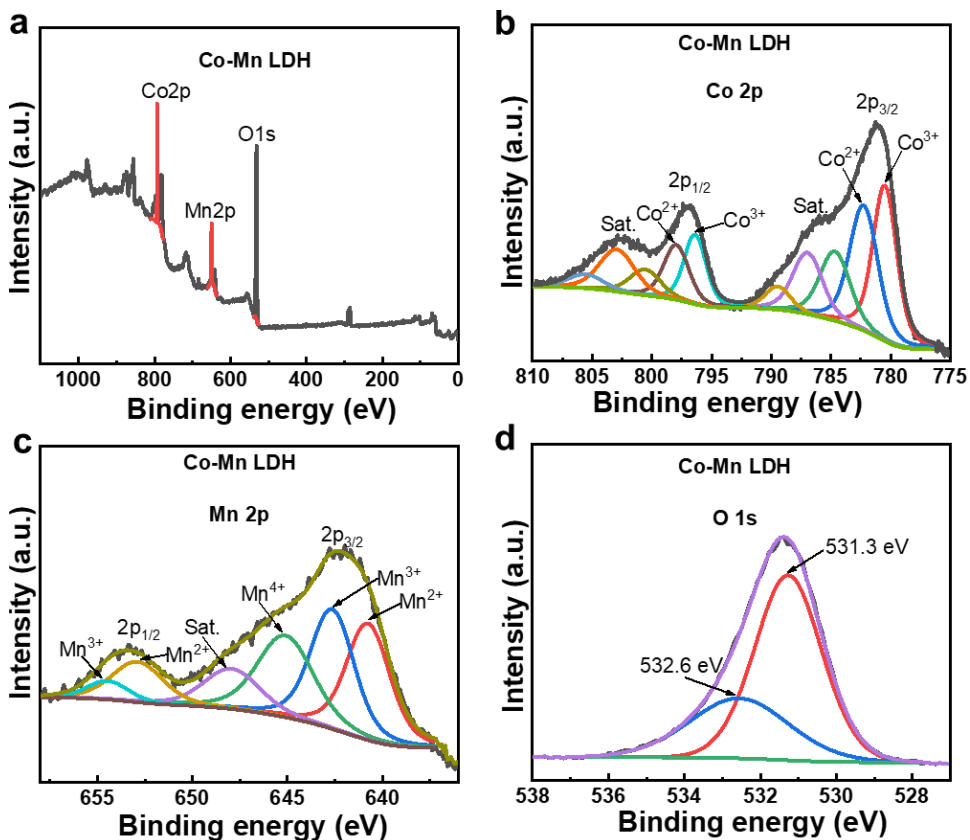


Figure 3. 8 (a) Full-scan XPS spectrum of CoMn-LDH, and XPS spectra of (b) Co 2p, (c) Mn 2p, and (d) O 1s.

As shown in Figure 3. 9, the full-scan XPS spectrum of CoMn-LDH@Ni(OH)₂ revealed the copresence of Co, Ni, O, and Mn elements in the sample.

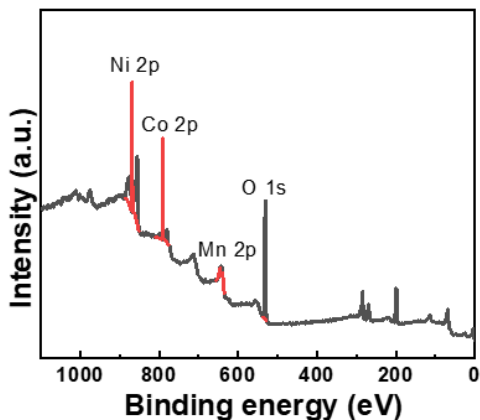


Figure 3. 9 XPS survey spectrum of CoMn-LDH@Ni(OH)₂.

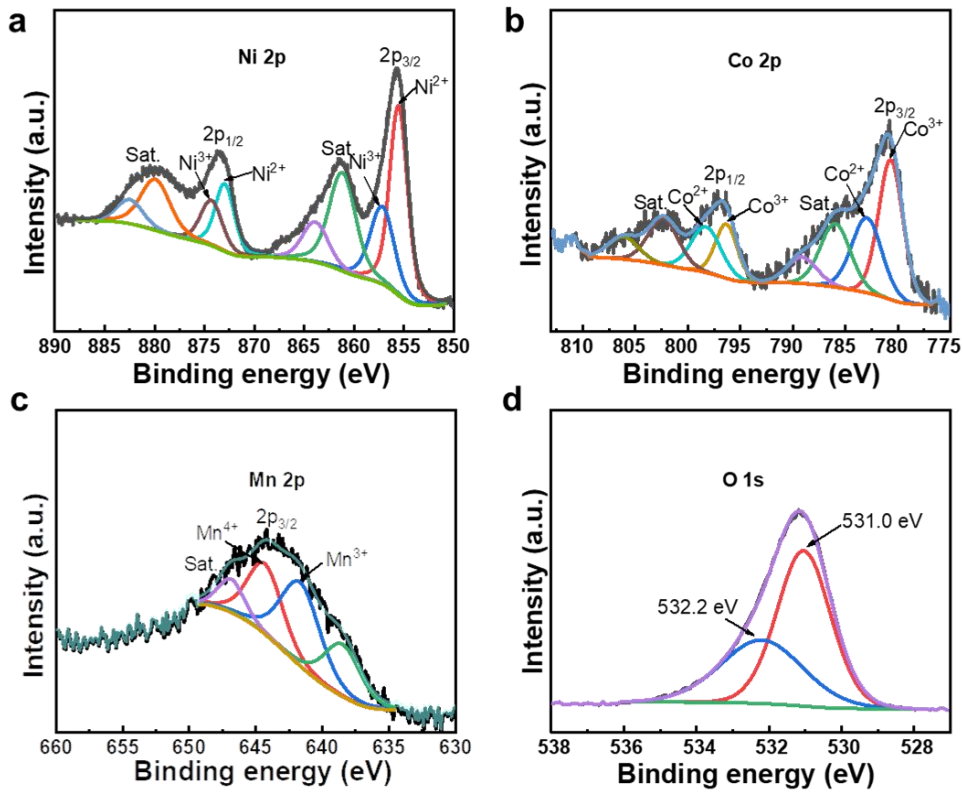


Figure 3. 10 High-resolution XPS spectra of CoMn-LDH@Ni(OH)₂. (a) Ni 2p, (b) Co 2p, (c) Mn 2p, and (d) O 1s.

Figure 3. 10a shows the Ni 2p spectrum of CoMn-LDH@Ni(OH)₂ which can be split into 2p_{1/2} (873.5 eV) and 2p_{3/2} (855.6 eV) accompanied by their satellite bands at 879.8 and 861.7 eV, confirming the presence of Ni²⁺ [93]. As compared to the Ni 2p spectrum of Ni(OH)₂, the above peaks are showing a positive shift to a higher binding energies direction. The Co 2p pattern displays two distinct peaks attributed to 2p_{1/2} (796.7 eV) and 2p_{3/2} (780.8 eV) accompanied by the satellite spin-orbit doublets, suggesting the copresence of Co³⁺ and Co²⁺, respectively [98] (**Figure 3. 10b**). These peaks of Co 2p show a ~ 0.3 eV negative shift as compared to those of CoMn-LDH. The peak shift demonstrates an intense electronic interaction between the core and shell at the interface [107,108]. The Mn 2p spectrum shows a single peak located at around 643.8 eV. The fitting peaks at 641.6 and 644.3 eV are confirming the copresence of Mn³⁺ and Mn⁴⁺ (**Figure 3. 10c**) [104,105]. In **Figure 3. 10d**, the O 1s spectrum is fitted into two different peaks. The peak positioned at 531.0 eV is attributed to oxygen bonding with Mn and Co, while the peak (532.3 eV) corresponds to absorbed H₂O molecules at/near the sample's surface [106],[103].

3.3 Nanowire-Nanosheet-like Dual Structured CoMnFeO₄

3.3.1 HT Synthesis of M_xMn_yO₄ (M = Co, Fe, and Ni)

Figure 3. 11 illustrates the fabrication process of the M_xMn_yO₄.

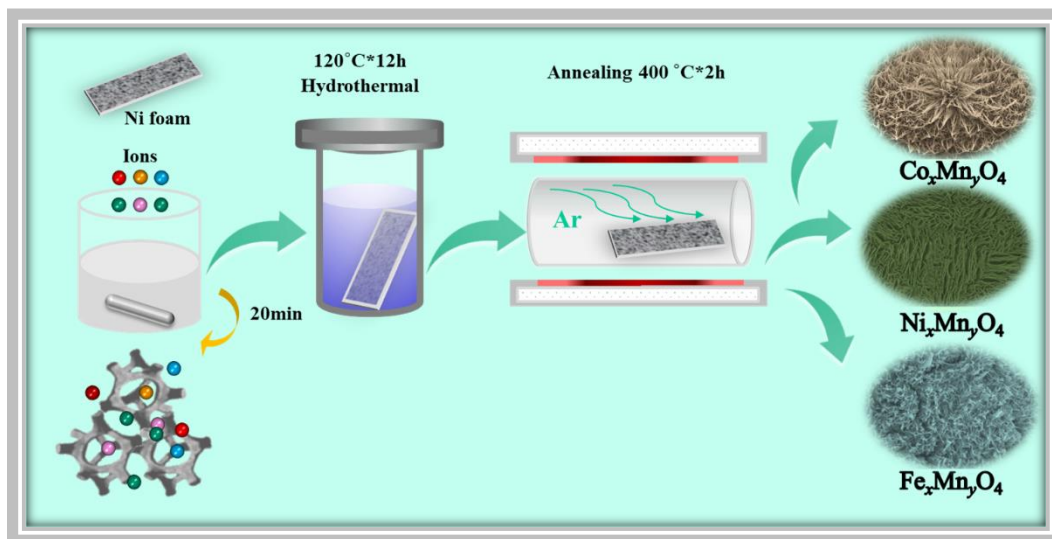


Figure 3. 11 Schematic for the preparation of M_xMn_yO₄ catalysts.

The precursor was deposited over NF by a facile HT method. Homogeneous CoMn-LDH precursor solutions were prepared by dissolving 0.5~3.5 mmol Co (NO₃)₂·6H₂O, 0.5~1.0 mmol MnSO₄·H₂O, 6 mmol CH₄N₂O, and 5 mmol NH₄F in 40 mL DI water. Especially, five different molar ratios of Co/Mn *viz.* 7: 1, 5: 1, 4: 1, 2: 1, and 1: 2 were prepared to decide the optimum design of Co/Mn for electrochemical catalytic activity. Similarly, FeMn-LDH (NiMn-LDH) precursor solutions were prepared by dissolving 0.5~3.5 mmol Fe (NO₃)₃·9H₂O (Ni (NO₃)₂·6H₂O), 0.5~1.0 mmol MnSO₄·H₂O, 6 mmol CH₄N₂O, and 5 mmol NH₄F in 40 mL DI water. Especially, five different molar ratios of Fe/Mn *viz.* 7: 1, 5: 1, 4: 1, 1: 2 (Ni/Mn *viz.* 7: 1, 5: 1, 4: 1, 1: 2) were prepared to determine the optimum design of Fe/Mn and Ni/Mn for electrochemical catalytic activity. After 25 min of continuously stirring, the precursor solution and rinsed NF substrates were placed in a stainless-steel reactor with a Teflon lining. The reactor was tightly sealed, placed into the oven, and heated to 120°C holding for 12 hours. Then, the reactor was cool naturally to 20°C. The resulting NF was rinsed with ethanol and DI water several times and then dried at 55°C for 5 hours. For a comparative study, a similar procedure was used to synthesize M_xMn_yO₄ with different molar concentrations *viz.* 1, 4, and 8 mM. The precursor was calcinated in Ar at 350°C for 1 hour, and a schematic for the calcination device was exhibited

in Figure 3. 12.

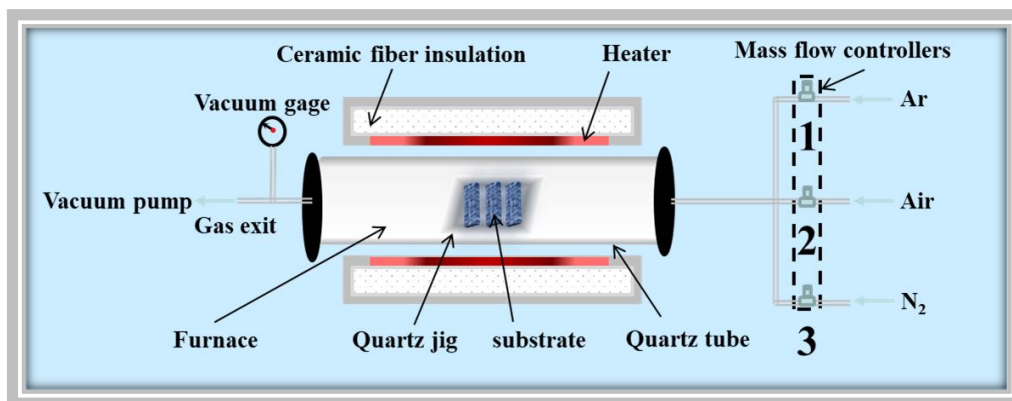


Figure 3. 12 Schematic of calcination device.

3.3.2 HT Synthesis of CoMnFeO_4

A homogeneous precursor solution was then prepared via dissolving $\text{Co}(\text{NO}_3)_2 \cdot 6\text{H}_2\text{O}$ (2 mmol), $\text{MnSO}_4 \cdot \text{H}_2\text{O}$ (0.5 mmol), $\text{FeCl}_3 \cdot 6\text{H}_2\text{O}$ (0~2 mmol), $\text{CH}_4\text{N}_2\text{O}$ (6 mmol), and NH_4F (5 mmol) in DI water (40 mL). After 25 min of continuously stirring, the pre-made solution and pretreated NF substrates were placed in a stainless-steel reactor with a Teflon lining. The reactor was sealed firmly, placed into an oven, and heated to 120°C holding for 12 h. Then, the precursor was calcinated in Ar at 300°C for 1 hour. A similar preparation method was used to synthesize Co_2MnO_4 without adding $\text{FeCl}_3 \cdot 6\text{H}_2\text{O}$, and a series of CoMnFeO_4 under different calcination temperatures and time were also prepared for a comparative study. The fabrication process of the CoMnFeO_4 is illustrated in **Figure 3. 13**.

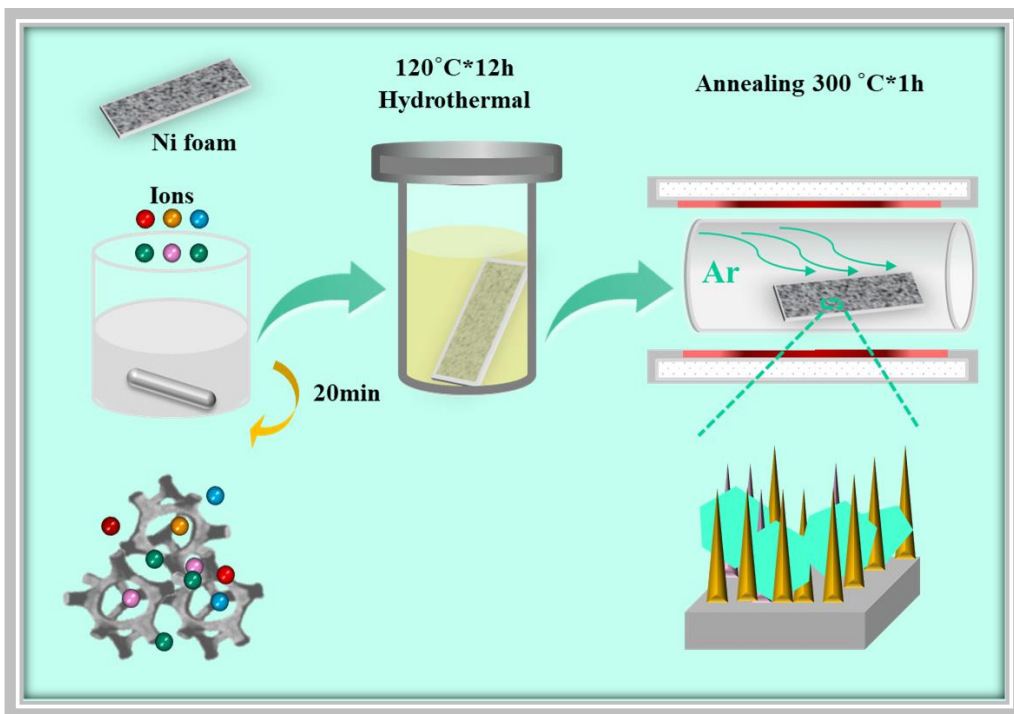
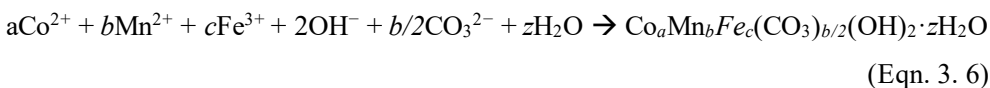


Figure 3. 13 Schematic for the preparation of CoMnFeO₄ catalysts.

3.3.3 Formation Mechanism of CoMnFeO₄

A one-step HT fabrication process followed by a calcination strategy for CoMnFeO₄ synthesis is illustrated in the above section. At first, the dissolved metallic cations react with OH⁻ generated via hydrolysis of CH₄N₂O, thereby fabricating seed crystal[88]. Next, the freshly formed seed crystals deposit on bare NF. This is followed by adjoining nanostructure particles and growth along a particular axis to form a certain nanostructure. The optical image of the samples is shown in **Figure 3. 14**. A possible mechanism is as follows: [19]



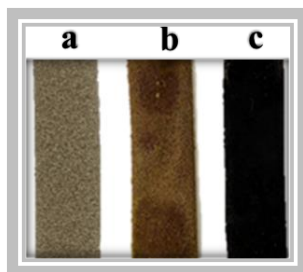


Figure 3. 14 The optical image of the samples: (a) bare NF, (b) precursor after HT, and (c) CoMnFeO_4 after annealing.

3.3.4 Morphological Analysis of $\text{M}_x\text{Mn}_y\text{O}_4$ (M = Co, Fe, and Ni)

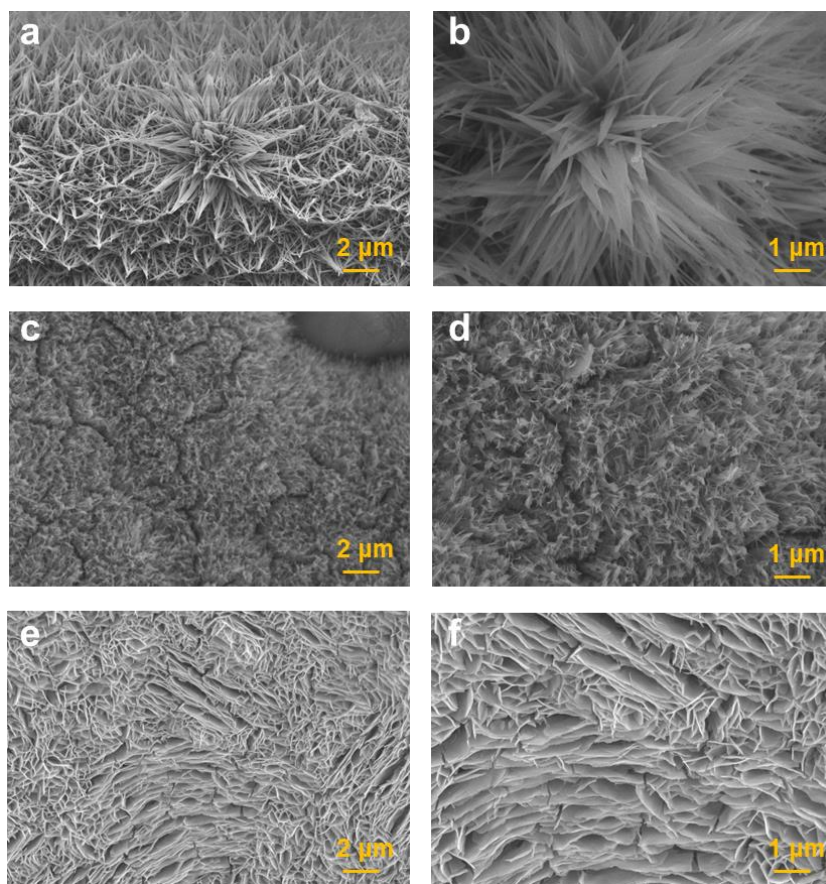


Figure 3. 15 FE-SEM images at different magnifications of (a, b) Co_2MnO_4 , (c, d) Fe_2MnO_4 , and (e, f) Ni_2MnO_4 .

The morphological properties of electrodes were studied by FE-SEM and TEM. Typically,

the morphologies of $M_xMn_yO_4$ were investigated and shown in **Figure 3. 15**. It was observed that Co_2MnO_4 , Fe_2MnO_4 , and Ni_2MnO_4 have entirely different morphology. In detail, the morphology of Co_2MnO_4 is one-dimensional nanowire, while that of Fe_2MnO_4 and Ni_2MnO_4 are nanowire-nanosheet coexisting structures and nanosheet, respectively. As the precursor parent particles aggregated, they began to crystallize and crystal planes grew along the a- or c-axis, gradually producing nanosheet or nanowire structure[109].

3.3.5 Structural Analysis of $CoMnFeO_4$

Figure 3. 16a shows the XRD patterns of Co_2MnO_4 and $CoMnFeO_4$. The three apparent peaks at $2\theta = 44.4^\circ$, 51.7° , and 76.2° can be indexed to NF (JCPDS card no. 04-0850)[91]. Except that, some spinel characteristic peaks at 2θ 31.1° , 36.6° , 58.9° , and 64.7° coincide well with (220), (311), (511), and (440) crystal planes of Co_2MnO_4 for both samples (space group Fd-3m with JCPDS card no. 84-0482)[53][110]. As clearly illustrated in **Figure 3. 16b** (amplified the area in the red dotted cycle of Figure 3.16a), it is obvious that the main peaks of $CoMnFeO_4$ show a slightly negative shift, indicating the expansion of the lattice constant due to a relatively larger ionic radius of Fe ($Fe^{2+} \sim 0.076$ nm, $Fe^{3+} \sim 0.065$ nm) compared with that of Co ($Co^{2+} \sim 0.072$ nm, $Co^{3+} \sim 0.055$ nm) [111]. Besides, broad and weak peaks of $CoMnFeO_4$ result from poor crystallization, high structural disorder, and high concentration of active sites. This is possibly beneficial for boosting electrocatalytic performance[46]. In addition, the XRD patterns of the $CoMnFeO_4$ series with different Fe contents are also shown in **Figure 3. 16c**.

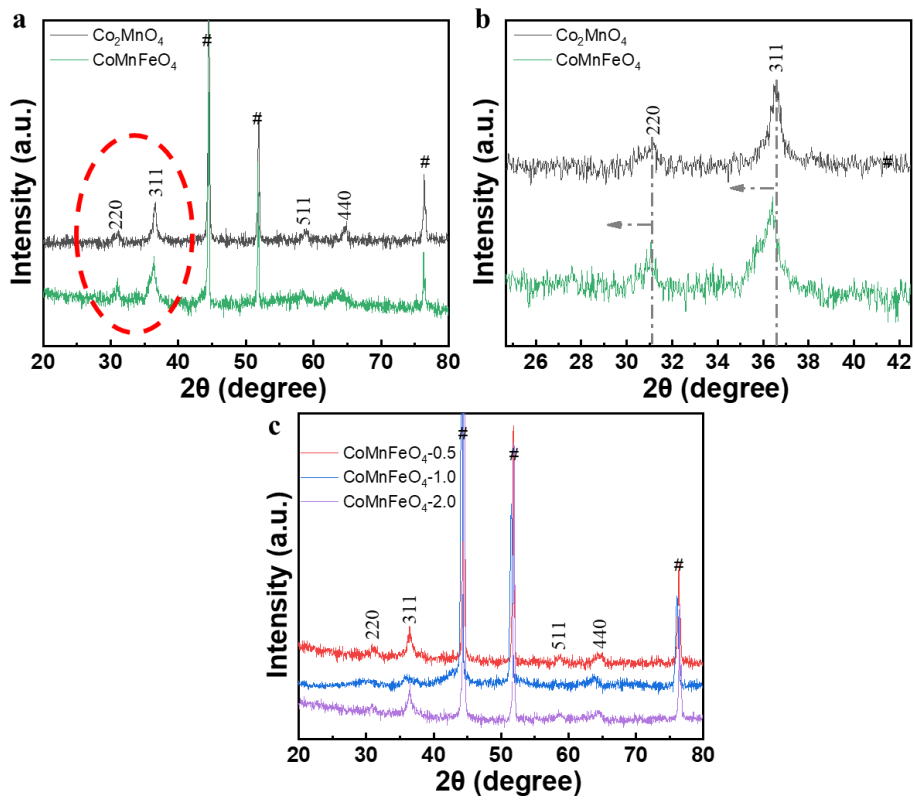


Figure 3. 16 XRD patterns of (a, b) Co_2MnO_4 and CoMnFeO_4 and (c) CoMnFeO_4 series.

3.3.6 Morphological Analysis of CoMnFeO_4

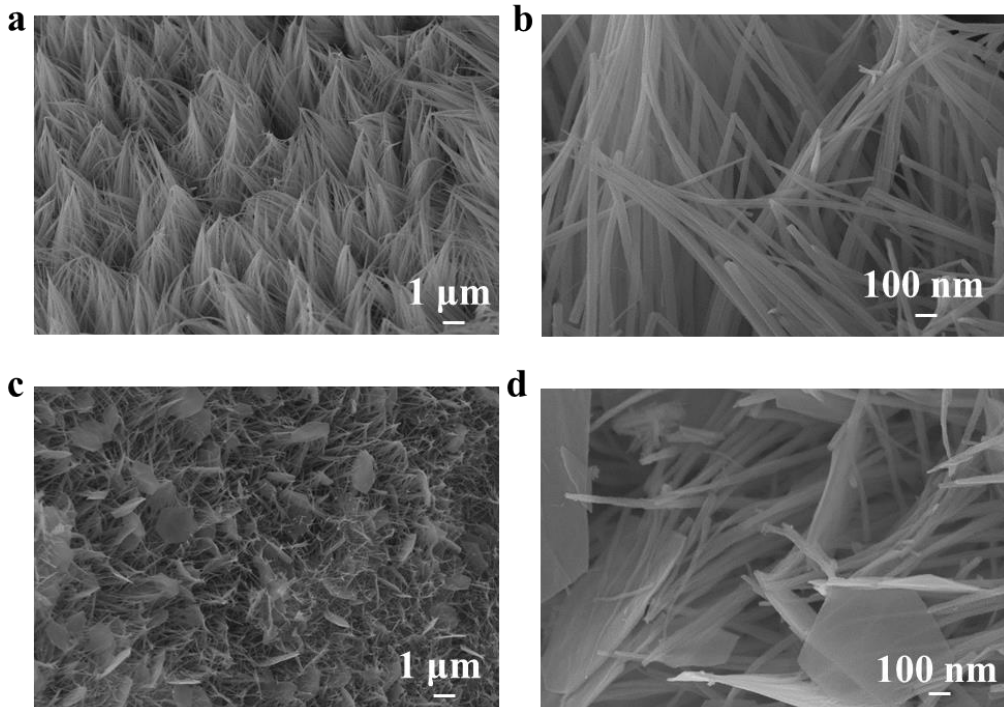


Figure 3. 17 (a) FE-SEM images of (c, d) Co_2MnO_4 nanowires and (e, f) CoMnFeO_4 at different magnifications.

Figure 3. 17(a, b) shows the FE-SEM images of Co_2MnO_4 , revealing only nanowires deposited on bare NF. **Figure 3. 17(c, d)** shows the FE-SEM images of CoFeMnO_4 , revealing nanowire-nanosheet dual structured morphology of CoFeMnO_4 , suggesting the Fe addition affects crystal planes of material generation.

A difference in nanostructures could be seen among the electrodes with various Fe contents (**Figure 3. 18**).

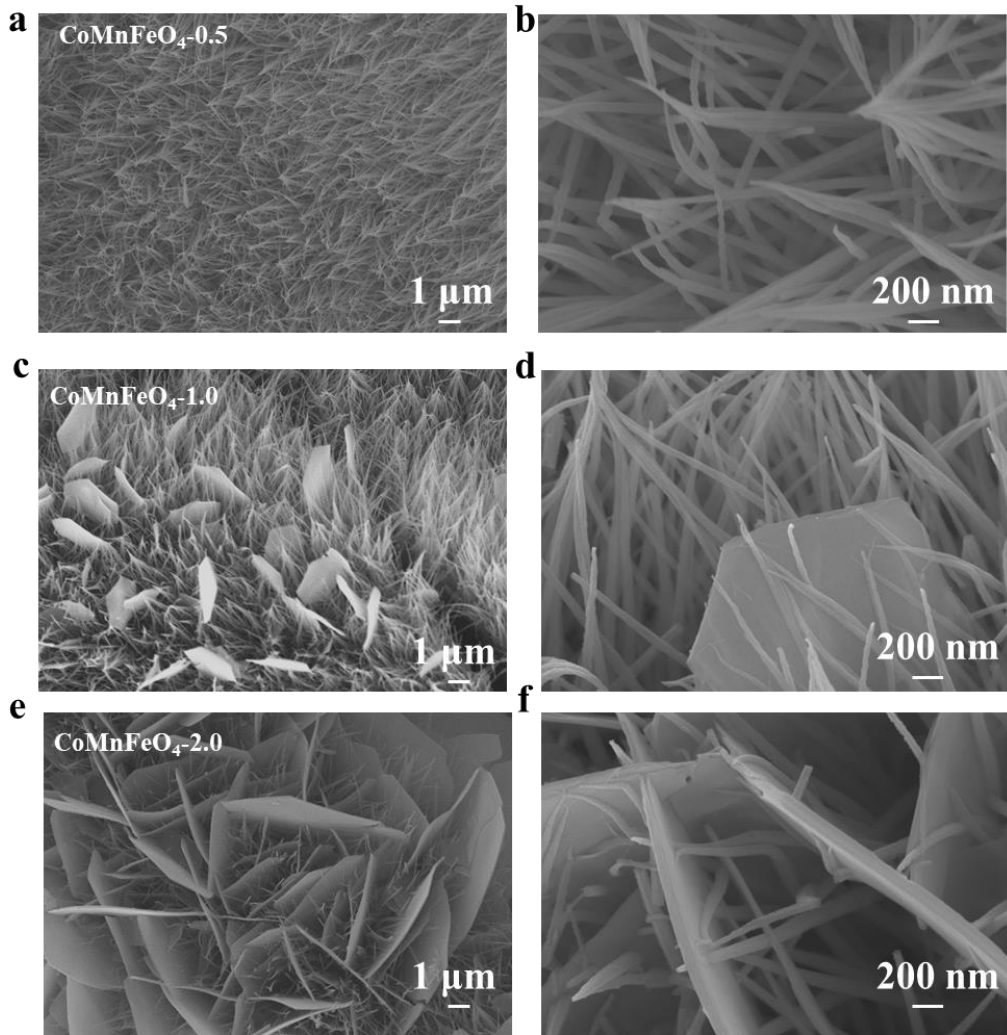


Figure 3. 18 FE-SEM images of CoMnFeO_4 with Fe concentration of (a, b) 0.5, (c, d) 1.0, and (e, f) 2.0 mmol.

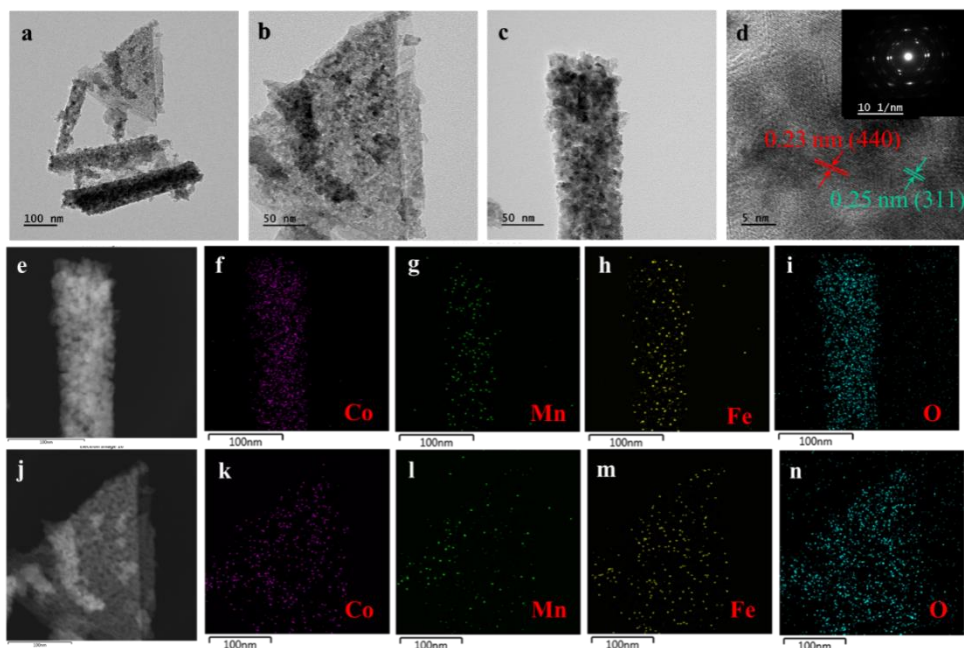


Figure 3. 19 (a-c) TEM image (d) HR-TEM image (inset: corresponding SAED). (e-n) EDS profiles and elemental mapping of CoMnFeO₄.

TEM was carried out to further confirm the unique nanostructure of CoMnFeO₄. The coexistence of both nanowires and nanosheets is apparent in **Figure 3. 19a-c**, which coincides well with the FE-SEM results. The lattice fringes with an interlayer spacing of 0.23 and 0.25 nm were indexed to (440) and (311) planes, respectively (**Figure 3. 19d**). The SAED pattern displayed distinct diffraction rings, suggesting single crystallinity of CoMnFeO₄ (inset of Fig. 3d). EDS elemental mappings were used to investigate the elemental distribution and compositions. **Figure 3. 19e-n** and **Figure 3. 20** show uniformly distributed and coexisted Co, Fe, Mn, and O.

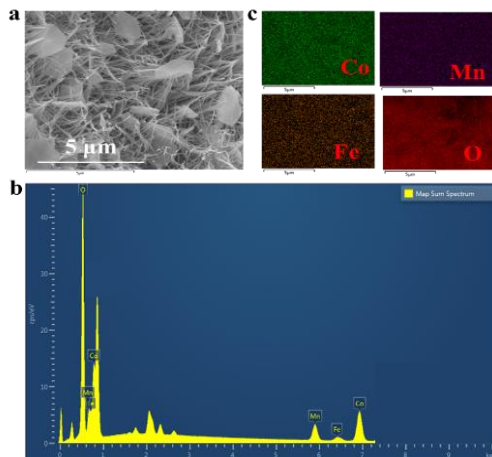


Figure 3. 20 (a) SEM image, (b) EDS profile, and (c) elemental mapping of CoMnFeO_4 .

3.3.7 XPS Analysis of CoMnFeO_4

XPS measurements were carried out to check the elemental compositions and chemical valence states. The corresponding full-scan XPS spectra indicated the formation of oxides of Co, Mn, Fe, and O (**Figure 3. 21**).

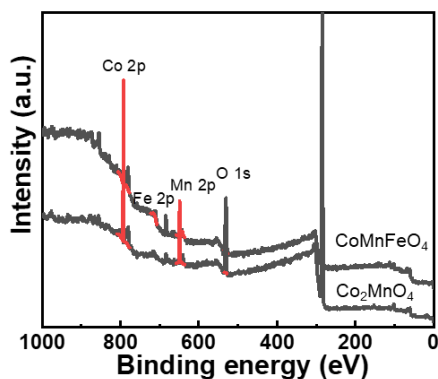


Figure 3. 21 XPS survey spectra of CoMnFeO_4 and Co_2MnO_4 .

The high-resolution Co 2p spectra of CoMnFeO_4 are split into Co $2p_{3/2}$ (781.02 eV) and Co $2p_{1/2}$ (796.42 eV) accompanied by two satellite bands, suggesting the presence of Co^{2+} and Co^{3+} (**Figure 3. 22a**)[112]. It should be worthy to mention that these peaks of Co 2p spectra for CoMnFeO_4 show a negative shift (slightly shifted to the direction of low binding energies) of around 0.18 eV than those of Co_2MnO_4 . As presented in **Figure 3. 22b**, the high-resolution Mn

2p spectra of CoMnFeO_4 are split into Mn $2p_{3/2}$ (639.03 eV) and Mn $2p_{1/2}$ (653.35 eV). The corresponding two identified peaks at 641.49 and 645.09 eV suggested the presence of Mn^{3+} and Mn^{4+} , respectively[53][111]. Similarly, the negative shift of Mn 2p can also be observed as compared to the Mn 2p spectra of Co_2MnO_4 . The negative shift of high-resolution Co 2p and Mn 2p spectra demonstrated a strong electronic interaction and extra electron transfer on Co and Mn ions of CoMnFeO_4 compared to those of Co_2MnO_4 [107][46]. The high-resolution Fe 2p spectrum of CoMnFeO_4 is split into Fe $2p_{3/2}$ (710.29 eV) and Fe $2p_{1/2}$ (721.13 eV), indicated the presence of Fe^{2+} and Fe^{3+} , respectively (**Figure 3. 22c**). In addition, the O 1s spectra of CoMnFeO_4 showed two separate peaks at 529.76 and 531.31 eV, which were fitted into four peaks (**Figure 3. 22d**). Typically, the peak located at 532.21 eV was ascribed to oxygen ions in a state of oxygen vacancies[113], and the peak centered at 531.32 eV was ascribed to physisorbed and chemisorbed water at/ near the surface of the samples[103,106], the peaks located at 529.91 and 529.33 eV was indexed to metal-oxygen bond[56]. Overall, the aforementioned results confirmed the successful fabrication of pure CoMnFeO_4 .

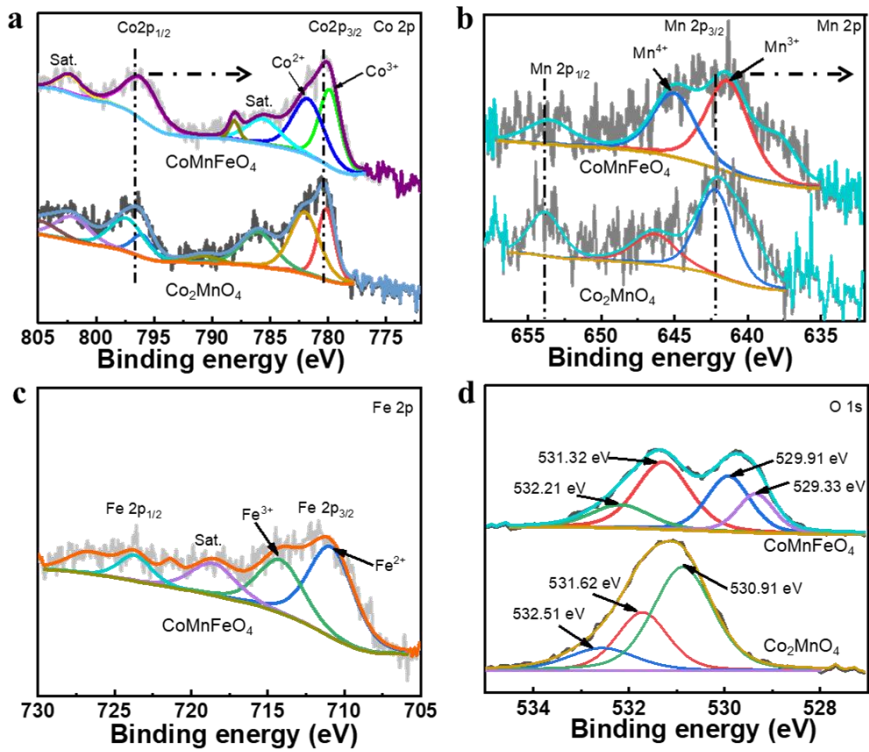


Figure 3. 22 High-resolution XPS spectra of CoMnFeO_4 and Co_2MnO_4 . (a) Co 2p, (b) Mn 2p, (c) Fe 2p, and (d) O 1s.

3.4 Summary

In this chapter, hierarchical heterostructure with core-shell nanowires of CoMn-LDH@Ni(OH)₂, unique nanowire-nanosheet-like dual structured CoMnFeO₄, and nanosheets of NiFeCoSe₂ have been successfully fabricated by HT method combined ED, HT method, ED method, respectively. With the systematic variation of the synthesis parameters of deposition methods such as precursor molar concentration, the molar ratio of metal cations, HT time, electrodeposition voltage, and deposition time, the structural and morphological properties can be fine-tuned. For CoMn-LDH@Ni(OH)₂, the obtained XRD and FTIR analysis fully support the formation of β-Ni(OH)₂ and CoMn-LDH. FE-SEM, TEM, and HR-TEM depict that Ni(OH)₂ shell covers the CoMn-LDH nanowire which deposits on the NF surface perpendicularly and densely. For CoMnFeO₄, the XRD patterns indicate the spinel-type CoMnFeO₄ was obtained. Varying the Fe concentration, the number of nuclei of the cation center changes resulting in morphology changes from nanowires to a nanowire-nanosheet dual structure. In the case of NiFeCoSe₂, the XRD and Raman spectra display the obtained nanocomposite is made up of NiSe₂, FeSe₂, and CoSe₂. FE-SEM, TEM, and HR-TEM show the resultant nanostructure is a nanosheet with lattice fringes of 0.25, 0.26, and 0.29 nm which nicely match the (120) crystal plane of NiSe₂, (111) of CoSe₂, and (200) of FeSe₂, respectively.

4. Investigation of Electrochemical Performance of Catalysts and Their Application in Overall Water splitting

4.1 Electrochemical Measurements

All electrochemical measurements including OER and HER were measured using a WonATech, WMPG1000 Multichannel Potentiostat at room temperature in 1 M KOH solution with a standard three-electrode configuration. To construct a three-electrode cell, as-prepared material, Ag/AgCl, and platinum wire were served as WE, RE, and CE, respectively. The OER performances were assessed by LSV curve at a scan rate of 1 mV s⁻¹. Nernst equation (Eqn. 4. 1) was used to convert all potentials in accord with the reversible hydrogen electrode (RHE) [114].

$$E_{RHE} = E_{Ag/AgCl} + (0.197 + 0.059 \times pH) \quad (\text{Eqn. 4. 1})$$

According to the following equation (Eqn. 4. 2), we can calculate the overpotential (η)[115].

$$\eta = E_{RHE} - 1.23 \text{ V} \quad (\text{Eqn. 4. 2})$$

The Tafel slopes obtained from the LSV curves were fitted to the Tafel equation (Eqn. 4. 3):[116]

$$\eta = a + T_s * \log J_c \quad (\text{Eqn. 4. 3})$$

Where ' η , a, T_s , and J_c ' indicate the overpotential, a constant, Tafel slope, and the obtained current density.

Long-term stability was recorded via chronopotentiometry measurement. Unless specified otherwise, the exposed area of the WE was kept constant at 1 × 1 cm² for all electrochemical characterizations.

A typical CV method was used to determine the ECSA via the equation (Eqn. 4. 4) as follows:[117]

$$ECSA = C_{dl} / C_s \quad (\text{Eqn. 4. 4})$$

Where ' C_{dl} ' is the double-layer capacitance, and ' C_s ' is the specific capacitance ($C_s = 0.04$ mF cm⁻² in a 1 M KOH electrolyte)[106]. The slope of the linear relationship between the double

layer charging current and the scanning rate of the CV plots gives the C_{dl} .

The specific activity (SA) is formulated below and is generally expressed in mA cm^{-2} : [118]

$$SA = i / A \quad (\text{Eqn. 4. 5})$$

Where ‘i’ and ‘A’ denote the current and the ECSA of the electrocatalyst, respectively.

The mass activity (MA) is given below and generally expressed in A g^{-1} : [119,120]

$$MA = i / m \quad (\text{Eqn. 4. 6})$$

Where ‘i’ and ‘m’ denote the current and the loading mass of the electrocatalyst, respectively.

This chapter describes a thorough investigation of electrochemical activity for CoMn-LDH@Ni(OH)₂, Co₂MnO₄, Fe₂MnO₄, Ni₂MnO₄, and CoMnFeO₄, respectively. The optimization of molar ratio and concentration of precursor, OER, and HER performance, origin of superior performance, and catalytic mechanism of them were presented.

4.2 Core-Shell CoMn-LDH@Ni(OH)₂ for Overall Water Splitting

4.2.1 Optimization of CoMn-LDH@Ni(OH)₂ via OER Studies

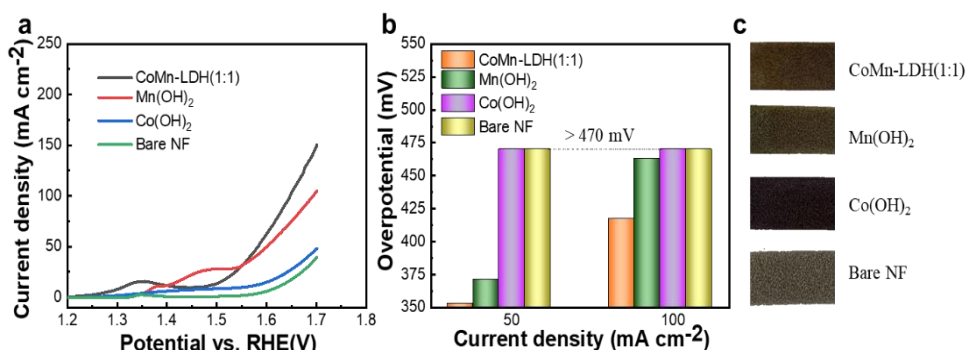


Figure 4. 1 OER polarization curves of CoMn-LDH (1:1), Mn (OH)₂, Co(OH)₂, and bare NF in 1.0 M KOH at a scan rate of 1 mV s⁻¹. (b) Overpotential at a current density of 50 and 100 mA cm⁻² (c) Optical images.

The OER performances and optical photographs of the bare NF, Co(OH)₂, Mn(OH)₂, and CoMn-LDH nanowires with Co: Mn ratio (1:1) are displayed in **Figure 4. 1**. It was found that the electrocatalyst of CoMn-LDH (1: 1) shows better OER performance and lower overpotential than the others. It only needs ~350 and 415 mV of overpotential to deliver 50 and 100 mA cm⁻², obviously outstanding to Mn (OH)₂ (370 mV and 410 mV), Co(OH)₂ (> 470 and > 470 mV), and

bare NF (> 470 and > 470 mV) (**Figure 4. 1a & b**). By comparing the catalytic performances of bare NF, $\text{Co}(\text{OH})_2$, $\text{Mn}(\text{OH})_2$, and CoMn-LDH (1:1), we can conclude that CoMn-LDH with dual cations Co and Mn has the best electrochemical activity with lower overpotential and faster current density response. The enhanced electrochemical catalytic activity for OER of CoMn-LDH is caused by the synergistic effect of heteroatoms. The optical images of the bare NF, $\text{Ni}(\text{OH})_2$, CoMn-LDH , and $\text{CoMn-LDH@Ni}(\text{OH})_2$ nanowires are shown in **Figure 4. 1c**, it is simple to distinct that they exhibit different surface states and colors with different deposited materials.

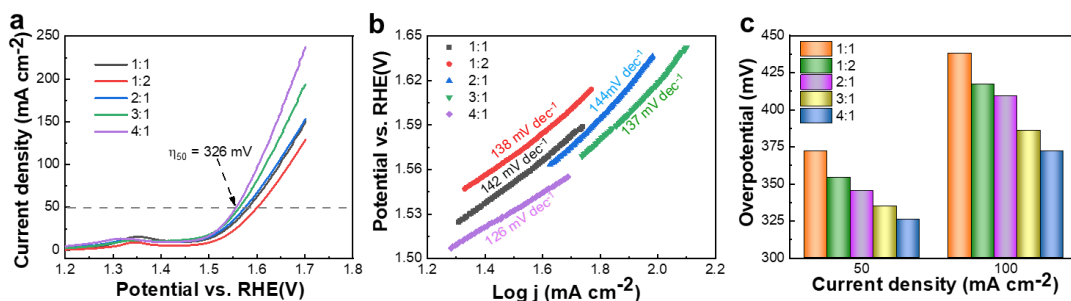


Figure 4. 2 (a) OER polarization curves of CoMn-LDH with different Co: Mn molar ratios in 1.0 M KOH at a scan rate of 1 mV s^{-1} . (b) Tafel plots. (c) Overpotential at a current density of 50 and 100 mA cm^{-2} .

To study further the followed results from the variation of molar ratios on OER performance of catalysts, five different molar ratios of Co: Mn (4: 1, 3: 1, 2: 1, 1: 1, 1: 2) were prepared and better electrochemical activity was determined by finding the optimum value of molar ratio of Co: Mn. **Figure 4. 2** shows the OER performances of CoMn-LDH nanowires as a function of various Co: Mn ratios. Significantly improved catalytic performance was observed for electrocatalysts having a molar ratio of 4: 1 (denoted as CoMn-LDH) compared to electrocatalysts having other molar ratios. The optimum molar concentration of the precursor has a beneficial impact on electrocatalytic activity because it alters ion insertion and electrochemical reaction kinetics, resulting in changes in overall electrochemical performance. [81]. This CoMn-LDH electrocatalyst was further employed to synthesize hierarchically structured $\text{CoMn-LDH@Ni}(\text{OH})_2$, and the synthesis conditions have been provided in detail in chapter 3, (section 3.2)

4.2.2 Electrochemical Activity for OER and HER

The OER activities of CoMn-LDH@Ni(OH)₂ core-shell nanowires were evaluated along with that of bare NF, Ni(OH)₂, and CoMn-LDH under the similar conditions.

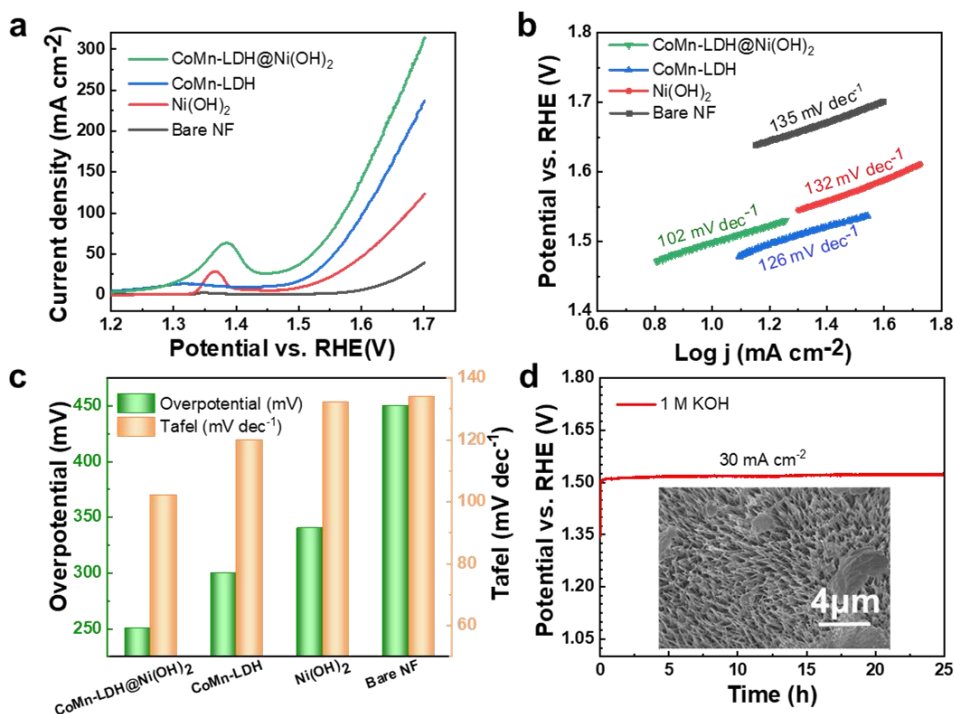


Figure 4. 3 (a) OER polarization curves of all catalysts at a scan rate of 1 mV s⁻¹ in 1 M KOH. (b) Corresponding Tafel plots (c) Comparative plots of overpotential and Tafel slopes of bare NF, Ni(OH)₂, CoMn-LDH, and CoMn-LDH@Ni(OH)₂ at a current density of 30 mA cm⁻². (d) Long-term stability measurement of CoMn-LDH@Ni(OH)₂ at 30 mA cm⁻² for 25 h. inset: FE-SEM images of CoMn-LDH@Ni(OH)₂ after long-term stability test.

The OER polarization curves for all catalysts including bare NF, Ni(OH)₂, CoMn-LDH, and CoMn-LDH@Ni(OH)₂ in **Figure 4. 3a**. A substantial increase in current density and decrease in overpotential was observed in the case of hierarchical CoMn-LDH@Ni(OH)₂ compared to pristine CoMn-LDH electrodes. The overpotentials for OER followed the order CoMn-LDH@Ni(OH)₂ < CoMn-LDH < Ni(OH)₂ < bare NF. The current density of 30 mA cm⁻² was achieved by CoMn-LDH@Ni(OH)₂ while requiring overpotentials of only 250 mV in contrast

with NF bare, Ni(OH)₂, and CoMn-LDH requiring significantly lower overpotentials of 450 mV, 340 mV, and 300 mV, respectively. Interestingly, at a remarkably large current density of 100 mA cm⁻², the overpotential of CoMn-LDH@Ni(OH)₂ nanowire electrode was respectively 29.6% and 8.8% smaller than those of Ni(OH)₂ and CoMn-LDH. Moreover, the estimated values of Tafel slopes shown in **Figure 4. 3b** for bare NF, Ni(OH)₂, CoMn-LDH, and CoMn-LDH@Ni(OH)₂ were 135 mV dec⁻¹, 132 mV dec⁻¹, 126 mV dec⁻¹, and 102 mV dec⁻¹, respectively, indicating a significantly lower value for CoMn-LDH@Ni(OH)₂. The overpotentials and the corresponding Tafel plots for all samples are shown in the bar chart in **Figure 4. 3c**. The lower values of overpotential and Tafel slope of CoMn-LDH@Ni(OH)₂ suggest better OER performance [94]. **Table 4. 1** lists the OER performances of other reported LDH-based catalysts. It can be seen that the OER performance of CoMn-LDH@Ni(OH)₂ is superior.

Table 4. 1 Comparison of OER performances of previously reported OER electrocatalysts.

Electrocatalysts	Substrate	Electrolyte	Overpotential (mV)	Reference
CoMn-LDH	Ni foam	1 M KOH	326	This work
CoMn-LDH@Ni(OH) ₂	Ni foam	1 M KOH	250	This work
CoMn LDH	-	1 M KOH	325	[92]
CoMn LDH	Glass Carbon	1 M KOH	324	[121]
CoMn-LDH/MWCNT	-	1 M KOH	300	[122]
CoMn LDH/CNT	-	0.1 M KOH	355	[104]
CoFe LDH	Ni foam	1 M KOH	300	[34]
NiFe LDH	Glass Carbon	1M KOH	375	[103]

The electrocatalysts have another important factor called long-term stability which must be considered in addition to electrochemical performance. Long-term stability can be evaluated using chronopotentiometry. **Figure 4. 3d** shows the long-term stability (25 hours) of CoMn-

LDH@Ni(OH)₂ at 30 mA cm⁻². The overpotential did not exceed 260 ± 3 mV during continuous electrolysis for 25 hours. It suggests the strong interaction between the NF substrate and CoMn-LDH@Ni(OH)₂ [123],[37].

After 25 hours of continuous electrolysis, FE-SEM (inset of **Figure 4. 3d**) and XPS (**Figure 4. 4**) analyses were performed. Structural analysis through FE-SEM investigations revealed the preserved arrays of nanowires with minute changes on the surface. This suggests that the structure of CoMn-LDH@Ni(OH)₂ was highly stable for catalytic OER. In addition, XPS results indicated the binding energies of CoMn-LDH@Ni(OH)₂ as Co 2p, Ni 2p, Mn 2p, and O 1s after stability. These binding energies are almost the same when compared to the original CoMn-LDH@Ni(OH)₂.

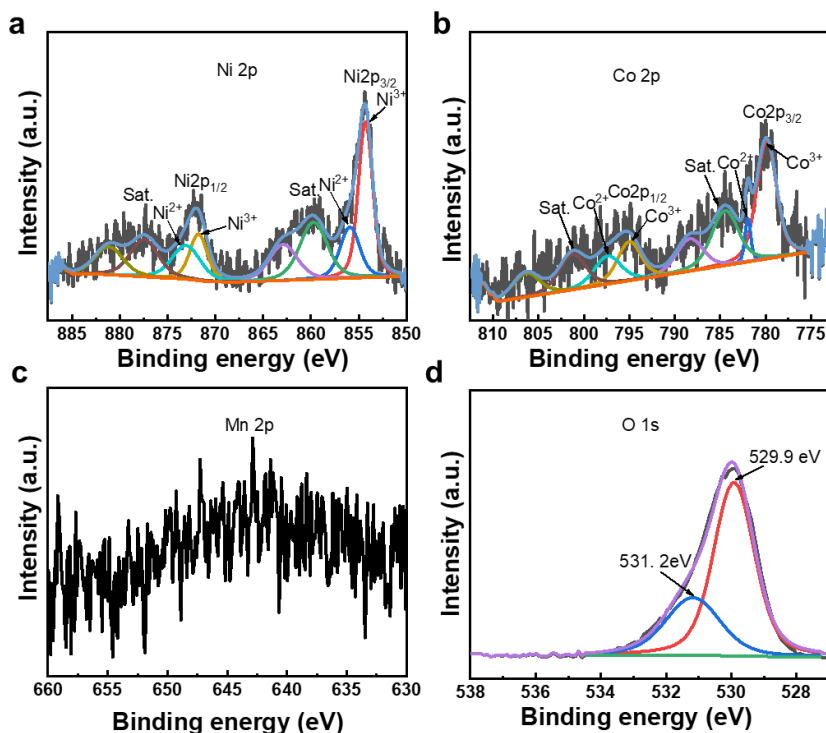


Figure 4. 4 XPS spectra of CoMn-LDH@Ni(OH)₂ after 25 hours stability test. (a) XPS survey spectrum and high-resolution XPS spectra of (b) Ni 2p, (c) Co 2p, (d) Mn 2p, and (e) O 1s.

Figure 4. 5a shows the HER polarization curves of all the electrodes. The current density of the hierarchical CoMn-LDH@Ni(OH)₂ electrode was substantially higher whereas overpotential (η) was significantly lower than that of the pristine CoMn-LDH electrode. The overpotentials for HER followed the order CoMn-LDH@Ni(OH)₂ < CoMn-LDH < Ni(OH)₂ < bare NF. Current density of 10 mA cm⁻² was achieved by CoMn-LDH@Ni(OH)₂ while requiring overpotentials of only 133 mV in contrast with NF bare, Ni(OH)₂, and CoMn-LDH requiring significantly lower overpotentials of 253, 223, and 187 mV, respectively. Interestingly, at a remarkably large current density of 100 mA cm⁻², the overpotential of CoMn-LDH@Ni(OH)₂ nanowire electrode was respectively 25.9% and 17.7% smaller than those of Ni(OH)₂ and CoMn-LDH, respectively (**Figure 4. 5b**). Moreover, the estimated values of Tafel slopes shown in **Figure 4. 5c** for bare NF, Ni(OH)₂, CoMn-LDH, and CoMn-LDH@Ni(OH)₂ were 135, 37, 158, and 27 mV dec⁻¹, respectively, indicating a significantly lower value for CoMn-LDH@Ni(OH)₂. **Table 4. 2** lists the HER performances of other reported LDH-based catalysts. It can be seen that the OER performance of CoMn-LDH@Ni(OH)₂ is superior.

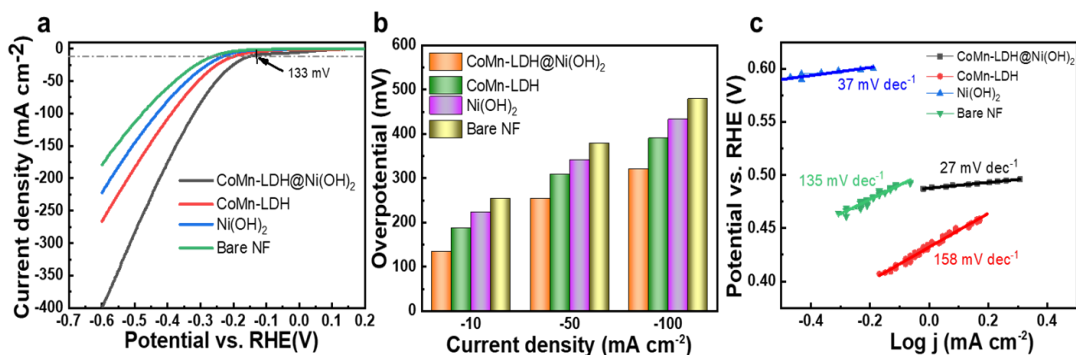


Figure 4. 5 (a) HER polarization curves of all catalysts at a scan rate of 1 mV s⁻¹ in 1 M KOH. (b) Comparison of overpotentials at current densities of -10, -50, and -100 mA cm⁻² (c) Corresponding Tafel plots.

Table 4. 2 Comparison of HER performances of previously reported HER electrocatalysts.

Electrocatalysts	Substrate	Electrolyte	Overpotential (mV) ^a	Reference
CoMn-LDH@Ni(OH) ₂	Ni foam	1 M KOH	133	This work
CoMn-LDH@g-C ₃ N ₄	-	1 M KOH	406	[92]
CoMn LDH	-	1 M KOH	491	[92]
Cu@NiFe-LDHs	-	1 M KOH	116	[124]
NiCoFe-LTHs	CFC	1 M KOH	200	[125]
CoSe/NiFe-LDH	EG	1 M KOH	260	[126]
NiFe-LDH/NiCo ₂ O ₄	Ni foam	1 M KOH	257	[93]

CFC: carbon fiber cloth; EG: exfoliated graphene.

Figure 4. 6a shows multiple current steps, the corresponding voltage increased and keep almost the same value at each stage of the various current range (10 ~ 200 mA cm⁻² each 500 s).

Figure 4. 6b shows the long-term stability (25 hours) of CoMn-LDH@Ni(OH)₂ at -10 mA cm⁻². The overpotential remained at ~133 mV during continuous electrolysis for 25 hours. After 25 hours of continuous electrolysis, FE-SEM analyses (**Figure 4. 6 c & d**) were performed. The FE-SEM images showed that the nanowire arrays were well preserved with only minor changes on the surface of the nanowire structure. This indicates excellent structural stability of the CoMn-LDH@Ni(OH)₂ electrode for electrocatalytic HER.

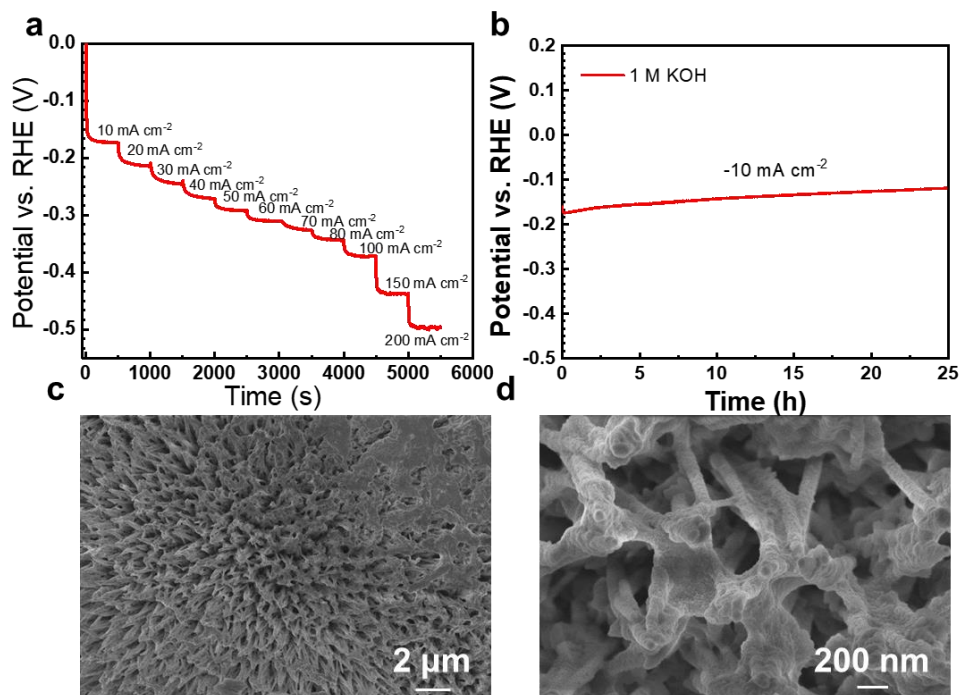


Figure 4. (a) Multiple current process (b) Long-term stability measurement of CoMn-LDH@Ni(OH)₂ at -10 mA cm^{-2} for 25 hours. (c, d) FE-SEM images of CoMn-LDH@Ni(OH)₂ after long-term stability test.

4.2.3 Origin of Superior Performance

We estimated the ECSA using a CV method (Eq. 4). The C_{dl} was determined by measuring voltammograms at different scanning rates ($2 \sim 12 \text{ mV s}^{-1}$) (Figure 4. 7 and 4. 8a).

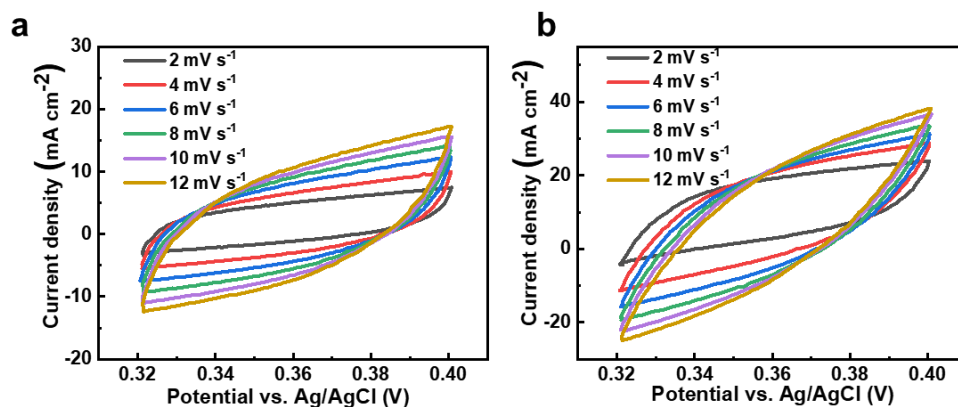


Figure 4. 7 CV curves at different scan rates of (a) CoMn-LDH, and (b) Ni(OH)₂.

Figure 4. 8b shows that C_{dl} values of CoMn-LDH@Ni(OH)₂, CoMn-LDH, and Ni(OH)₂ electrodes were 12.14, 8.71, and 7.95 mF cm⁻², respectively. C_{dl} of CoMn-LDH@Ni(OH)₂ electrode was respectively 39.3% and 52.7% higher than those of CoMn-LDH, and Ni(OH)₂ electrodes. The larger ECSA value of CoMn-LDH@Ni(OH)₂ electrode (303.50 cm⁻²) than those of CoMn-LDH (217.75 cm⁻²), and Ni(OH)₂ (198.75 cm⁻²) suggests the presence of more exposed active sites which favored the OER process[86]. Moreover, the conductivities and electrochemical performances of all samples were assessed by EIS. Nyquist plots of all samples with fitted equivalent circuits are respectively shown in **Figure 4. 8c** and **Figure 4. 9**. It shows that CoMn-LDH@Ni(OH)₂ possesses lower R_s (~ 0.53 Ω) and R_{ct} (~ 0.22 Ω) than CoMn-LDH (R_s - 0.54 Ω and R_{ct} - 0.24 Ω), Ni(OH)₂ (R_s - 0.57 Ω and R_{ct} - 0.48 Ω) The EIS results are consistent with other results indicating transfer of electrons at a more rapid rate during the electrocatalytic process for CoMn-LDH@Ni(OH)₂ electrode compared to CoMn-LDH and Ni(OH)₂. Additionally, the SA and MA of the electrocatalysts were calculated according to Eq. 5 and 6. At an overpotential of 320 mV, the MA and SA of CoMn-LDH@Ni(OH)₂ were 7.94 A g⁻¹ and 0.25 mA cm⁻², respectively while the corresponding values for CoMn-LDH and Ni(OH)₂ were 6.57 A g⁻¹, 0.21 mA cm⁻² and 4.1 A g⁻¹, 0.11 mA cm⁻², respectively (**Figure 4. 8d**). The above results indicate the enhanced OER activity of CoMn-LDH@Ni(OH)₂ is due to improvements in charge transport at the electrode/electrolyte interface and electrocatalytic active sites[86].

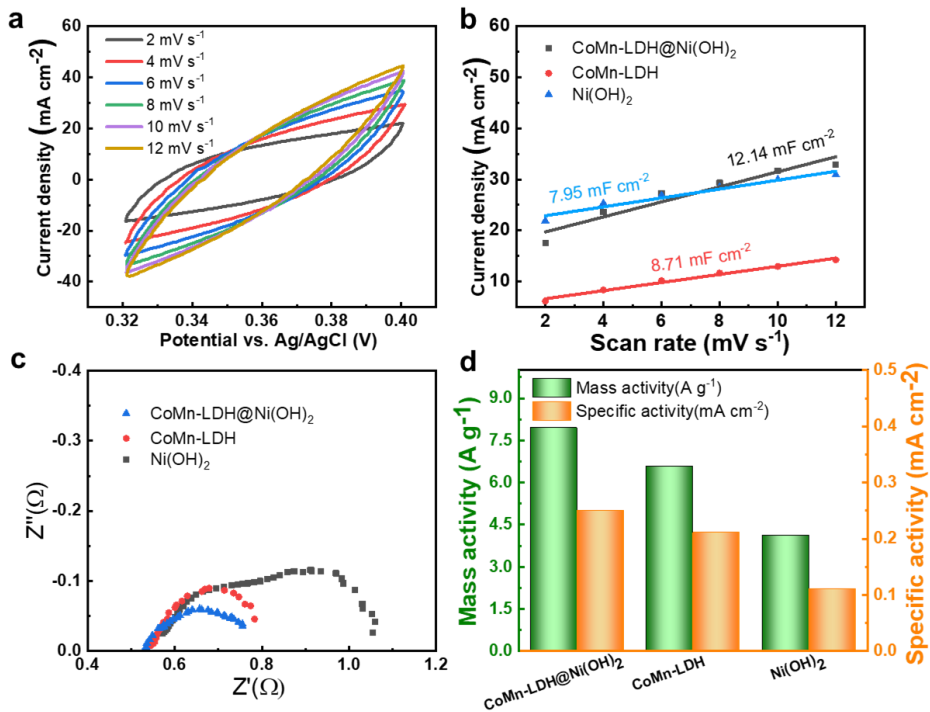


Figure 4. 8 (a) CV curves at different scan rates for CoMn-LDH@Ni(OH)₂. (b) Capacitive current density VS. scan rate, (c) Nyquist plots, and (d) Mass and specific activities at an overpotential of 320 mV of CoMn-LDH@Ni(OH)₂, CoMn-LDH, and Ni(OH)₂.

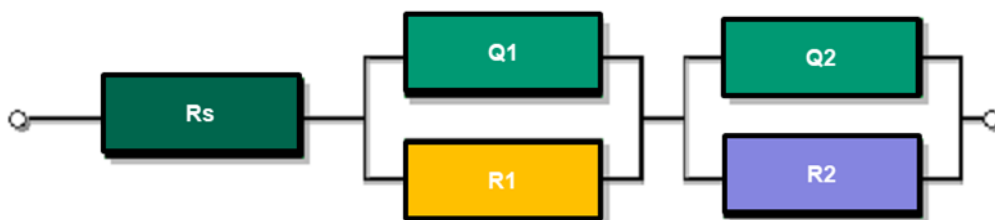


Figure 4. 9 The equivalent circuit of CoMn-LDH@Ni(OH)₂.

4.2.4 CoMn-LDH@Ni(OH)₂ for Overall Water Splitting

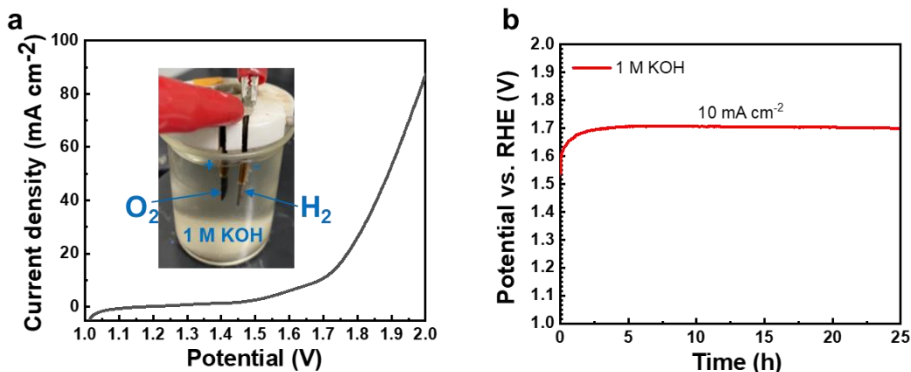


Figure 4. 10 Electrochemical performance of CoMn-LDH@Ni(OH)₂ towards overall water splitting (a) LSV polarization plot of a two-electrode system (inset: setup of the two electrode system) and (b) long-term stability over 25 hours at 10 mA cm⁻².

Table 4. 3 Comparison of overall water splitting performances of previously reported electrocatalysts.

Electrocatalysts	Substrate	Electrolyte	Voltage (V) @10 mA cm ⁻²	Durability (h)	Reference
CoMn-LDH@Ni(OH) ₂	Ni foam	1 M KOH	1.68	25	This work
NiCo ₂ O ₄	Ti foil	1 M KOH	1.73	20	[127]
Ni _{2.3%} -CoS ₂	Carbon cloth	1 M KOH	1.66	12	[128]
Co ₃ O ₄ NCs	CFP	1 M KOH	1.91	4	[129]
Co ₉ S ₈	Ni foam	1 M KOH	1.71	30	[130]
Ni(OH) ₂	-	1 M KOH	1.70	2	[131]
NiCo ₂ S ₄	Carbon cloth	1 M KOH	1.68	10	[132]

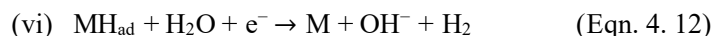
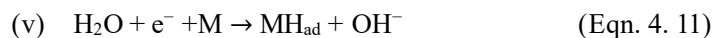
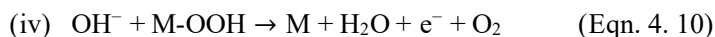
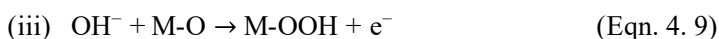
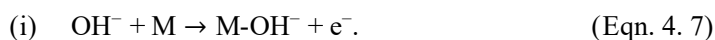
CFP: Carbon fiber paper

To explore the promising application of CoMn-LDH@Ni(OH)₂ for overall water electrolysis, an electrolyzer was performed with CoMn-LDH@Ni(OH)₂ as both cathode and anode in a two-electrode system. In **Figure 4. 10a**, it exhibits an overall cell voltage of 1.68 V to deliver 10 mA

cm². Additionally, it shows comparable and outstanding catalytic activity to that of previously reported electrocatalysts (Table 4. 3). In Figure 4. 10b, the long-term stability of CoMn-LDH@Ni(OH)₂ was measured and exhibits impressive durability over 25 hours without significant decay.

4.2.5 Mechanism Discussion

Herein, a basic mechanism of overall splitting of water related to the CoMn-LDH@Ni(OH)₂ core-shell catalyst is described. The water electrolysis process of CoMn-LDH@Ni(OH)₂ in an alkaline medium occurs in the following steps[106],[133].



Where M stands for Ni²⁺/Co²⁺/Mn³⁺ in the electrode. Consequently, the cyclic process proceeds with the redox couples (Ni²⁺/Ni³⁺, Co²⁺/Co³⁺, and Mn³⁺/Mn⁴⁺). It is to be noted that highly exposed active sites, largely exposed surface area, improved electronic modulation, synergistic enhancement and improved long-term durability are the outcomes of the correct engineering of this core-shell nanostructure of CoMn-LDH@Ni(OH)₂ [134]. When Ni(OH)₂ is deposited on the surface of CoMn-LDH nanowires, the energy difference between their conduction band acts as a driving force for the transfer of electrons from the CoMn-LDH core to Ni(OH)₂ shell.

More prominently, expedited and effective charge transfer as shown in Figure 4. 11 was probably due to the following factors: conductivity of the core was high, interfacial contact was excellent, and the shell had high activity. In addition, catalytic behavior was improved because the Ni(OH)₂ shell provided the more exposed active sites. The unsaturated Ni²⁺ ions show strong affiliation with OH⁻ which results in boosting the reaction kinetics thereby promoting the charge transfer.[40].

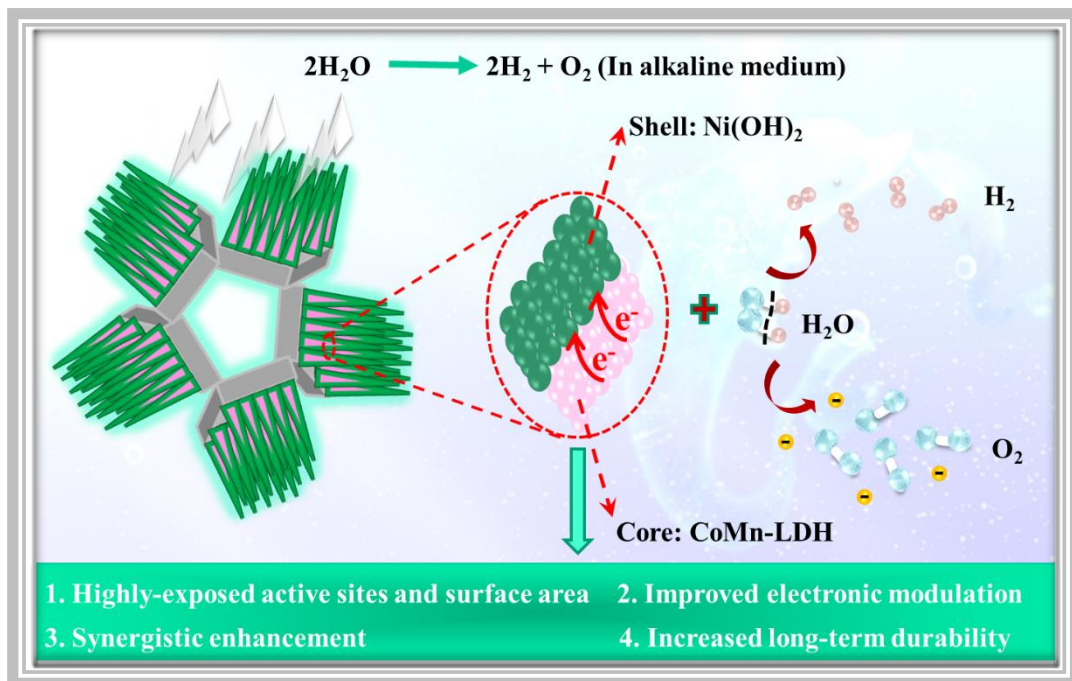


Figure 4. 11 Schematic of the overall water splitting process by the CoMn-LDH@Ni(OH)₂ core-shell nanowires.

In this section, the overall water splitting performance of CoMn-LDH@Ni(OH)₂ nanowires has been described. The as-prepared CoMn-LDH@Ni(OH)₂ exhibits significantly enhanced OER and HER performances. As anode, this as-prepared CoMn-LDH@Ni(OH)₂ electrode exhibits excellent oxygen evolution reaction (OER) performance with a lower overpotential of 250 and 341 mV at a current density of 30 and 100 mA cm⁻² respectively (without *iR*-correction) along with a lower Tafel slope of 102 mV dec⁻¹. As cathode, it exhibits outstanding HER performance with a lower overpotential of 133 mV at -10 mA cm⁻² (without *iR*-correction) along with a lower Tafel slope of 27 mV dec⁻¹. In addition, CoMn-LDH@Ni(OH)₂ remains stable for more than 25 hours in 1 M KOH electrolyte. Combining two CoMn-LDH@Ni(OH)₂ electrodes, a superior overall water electrolyzer required a low overall cell voltage of 1.68 V to reach 10 mA cm⁻² along with superior stability of 25 hours. This can be attributed to the unique hierarchical nanostructure, binder-free deposition, and synergistic effect of CoMn-LDH nanowire-core with

Ni(OH)₂-shell. This study provides a new strategy that can be applied to other sustainable and affordable energy conversion storage systems.

4.3 Heteroatomic Doping of CoMnFeO₄ for Water Oxidation

4.3.1 Performance Optimization of CoMnFeO₄ via OER studies

To determine the optimal Mn-based M_xMn_yO₄ (M = Co, Fe, Ni) electrocatalyst, a series of M_xMn_yO₄ were prepared and their OER performances were checked. In addition, the comparison of OER performances for series M_xMn_yO₄ was listed in **Figure 4. 12- 4. 13 & Table 4. 4-4. 6**. As a result, Co_xMn_yO₄ with a Co: Mn of 4: 1 and a molar concentration of 4 mM exhibited lower overpotential and faster current density response suggesting superior OER performance than the other Co_xMn_yO₄. In the case of Fe_xMn_yO₄, the electrode with a Fe: Mn of 1: 2 and a molar concentration of 8 mM exhibited superior OER performance than the other Fe_xMn_yO₄. In the case of Ni_xMn_yO₄, the electrode with a Ni: Mn of 7: 1 exhibited superior OER performance than the other Ni_xMn_yO₄. The relationship between the molar concentration of precursor and electrocatalytic activity of the as-prepared catalyst was carefully investigated and shown in **Figure 4. 12b & 4. 13b**. It was observed that the molar concentration of the precursor had a significant influence on electrocatalytic activity. The relatively high molar concentration of precursor significantly declined electrocatalytic activity as it decreased the insertion of ions and slowed down electrochemical reaction kinetics, so the overall electrochemical performance decreased. While the relatively low molar concentration of precursor provided few metal cations for the deposition. It may cause a very limited number of area active sites of catalysts and result in low electrochemical activity[81]. In addition, compared to the best one of each series of M_xMn_yO₄, the Co_xMn_yO₄ exhibited a lower overpotential of 416 mV at 50 mA cm⁻² and a faster current density of 101.42 mA cm⁻² at 1.7 V voltage than that of Fe_xMn_yO₄ (417 mV and 80.04 mA cm⁻²) and Ni_xMn_yO₄ (> 470 mV and 48.26 mA cm⁻²). Hence, it was further employed to

fabricate the CoMnFeO_4 .

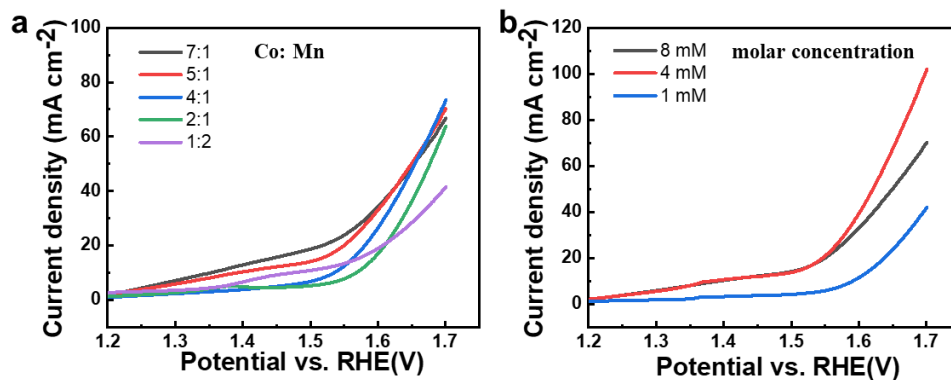


Figure 4. 12 OER polarization plots of $\text{Co}_x\text{Mn}_y\text{O}_4$.

Table 4. 4 Comparison of OER performances for different molar ratios and concentrations of $\text{Co}_x\text{Mn}_y\text{O}_4$.

Series	Co: Mn	Molar concentration (mM)	η_{50} (mV)	$j_{1.7\text{V}}$ (mA cm^{-2})
$\text{Co}_x\text{Mn}_y\text{O}_4$	7:1	8	419	66.57
	5:1	8	423	70.21
	4:1	8	424	73.85
	2:1	8	446	63.73
	1:2	8	> 470	41.48
	4:1	4	416	101.42
	4:1	1	> 470	41.64
	1:2	1	463	53.34

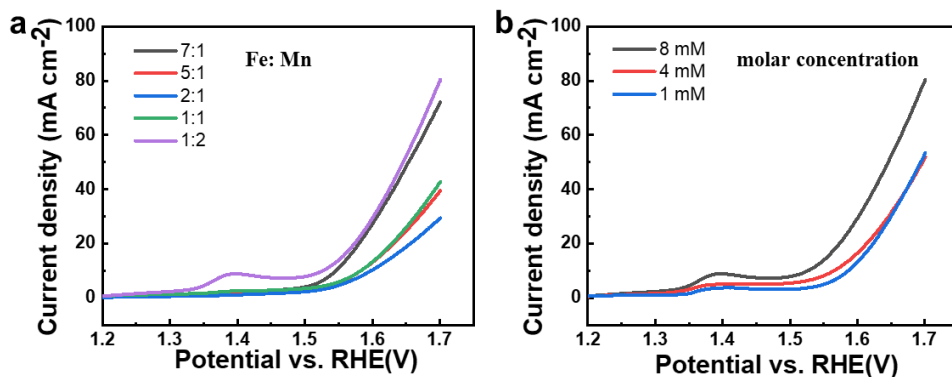


Figure 4. 13 OER polarization plots of $\text{Fe}_x\text{Mn}_y\text{O}_4$.

Table 4. 5 Comparison of OER performances for different molar ratios and concentrations of $\text{Fe}_x\text{Mn}_y\text{O}_4$.

Series	Fe: Mn	Molar concentration (mM)	η_{50} (mV)	$j_{1.7\text{V}}$ (mA cm^{-2})
$\text{Fe}_x\text{Mn}_y\text{O}_4$	7:1	8	422	72.32
	5:1	8	> 470	<40
	2:1	8	> 470	<40
	1:1	8	> 470	<40
	1:2	8	417	80.04
	1:2	4	465	52.12
	1:2	1	463	53.34

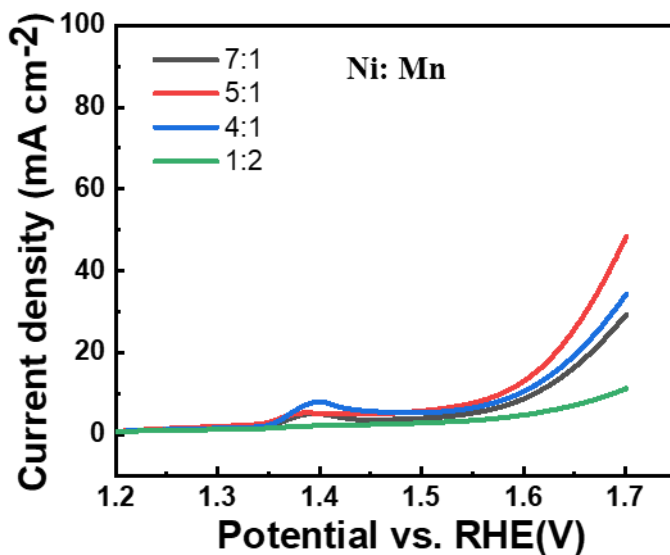


Figure 4. 14 OER polarization plots of $Ni_xMn_yO_4$.

Table 4. 6 Comparison of OER performances for different molar ratios and concentrations of $Ni_xMn_yO_4$.

Series	Ni: Mn	Molar concentration (mM)	η_{50} (mV)	$j_{1.7V}$ (mA cm ⁻²)
$Ni_xMn_yO_4$	7:1	8	> 470	48.26
	5:1	8	> 470	<40
	4:1	8	> 470	<40
	1:2	8	> 470	<40

4.3.2 Influence of Fe Concentration and Annealing Conditions on OER

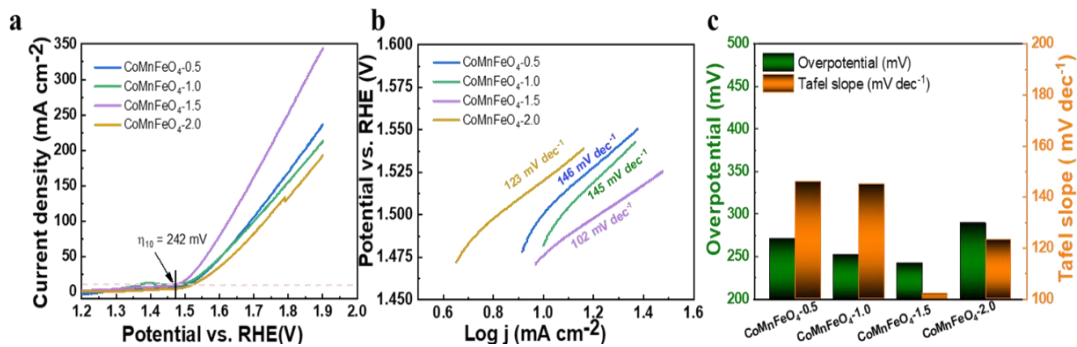


Figure 4. 15 The OER behavior of samples with different Fe concentrations.

To obtain the optimal sample, a series of samples with different Fe concentrations from 0.5, to 2.0 mmol were synthesized and denoted as CoMnFeO₄-0.5, CoMnFeO₄-1.0, CoMnFeO₄-1.5, and CoMnFeO₄-2.0, respectively. These compounds were compared for their OER behavior (**Figure 4. 15**). CoMnFeO₄-1.5 showed optimal OER performance (named as CoMnFeO₄) and was employed for further study.

Electrodes under different annealing conditions were collected to further study the calcination process of CoMnFeO₄, **Figure 4. 16a-b** shows LSV curves and overpotentials of samples under 200 mA cm⁻² at different calcination temperatures for 1 h. The sample calcinated at 300°C showed better OER performance and low overpotential to reach 200 mA cm⁻² compared to others. To investigate the origin of outstanding OER performance and crystallinity effect due to calcination, XRD analysis was carried out at different calcination temperatures (**Figure 4. 16c**). XRD images revealed that before annealing, the original sample exhibited a typical LDH structure[49] (JCPDS card no. 10-0144). After annealing at 200°C, the intensity of characteristic peaks corresponding to the LDH structure decreased significantly, and no extra peaks of spinel-type oxide showed up. The sample calcined at 300°C showed peaks corresponding to spinel-type oxide while the peaks for LDH structure disappeared. With the increase in calcination temperature to 500°C, the intensity of characteristic peaks for spinel-type oxide increased significantly. The broad and weak peaks result from poor crystallization, high structural disorder, and a high concentration of active sites. As the literature reporting, the ionic configuration of CoMnFeO₄ is denoted as (Co²⁺ Mn²⁺ Fe³⁺)[Co²⁺Mn³⁺Mn⁴⁺Fe³⁺] O₄²⁻[135]. The cations with a low valence state (such as Co²⁺, Mn²⁺) are unstable and tend to be easily oxidized at a temperature range from 200 to 450°C, resulting in a large number of vacancies that ultimately change the

chemical properties of the sample[111,135]. This is possibly beneficial for boosting the electrocatalytic performance[46] It is worthy to probe that 300°C is the appropriate temperature for calcination in the current research.

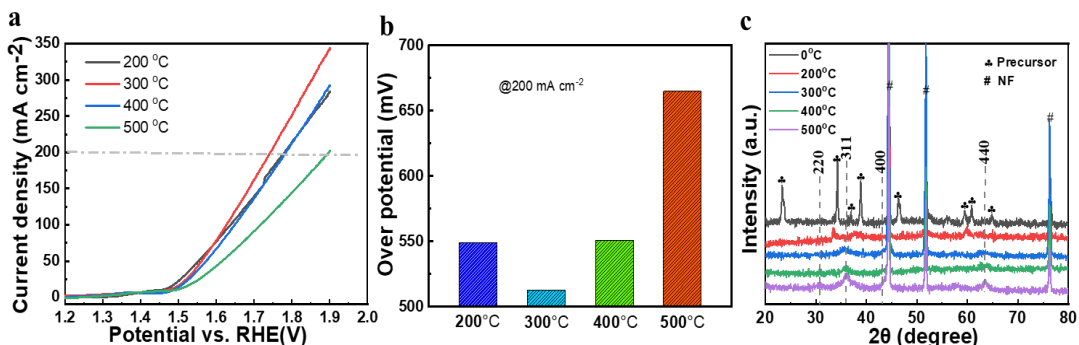


Figure 4. 16 (a) The LSV curves, (b)overpotentials under 200 mA cm⁻², and (c) XRD patterns of samples at different calcinated temperatures.

To know the optimal holding time under 300°C, we checked the LSV curves and overpotentials of samples at various holding times (**Figure 4. 17**). The sample calcined for 1 h showed better OER performance and low overpotential to reach 200 mA cm⁻² compared to others. To investigate the origin of outstanding OER performance and the crystallinity effect, we carried out the XRD patterns of the samples with different holding times (**Figure 4. 17c**). The XRD images revealed that before annealing, the original sample exhibited a typical LDH structure [49] (JCPDS card no. 10-0144). After annealing for 0.5 h, the intensity of characteristic peaks for LDH structure decreased, but no extra peaks of spinel-type oxide have been observed. Following the extended time to 1 h, the shape of peaks changed significantly, the peaks for LDH structure disappeared while the peaks for spinel-type oxide started to show up. As the temperature increased, the intensity of characteristic peaks for spinel-type oxide increased, suggesting increased crystallization. Samples with poor crystallization hold more active sites, which is beneficial for improving OER performance.

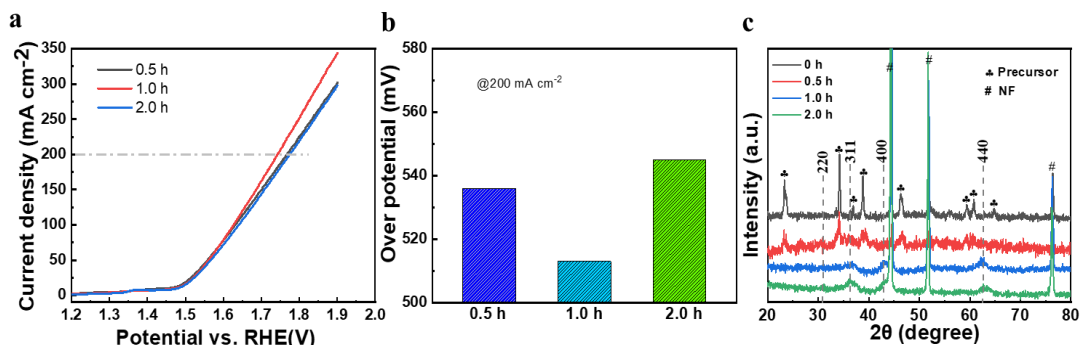


Figure 4.17 (a) The LSV curves, (b) overpotentials under 200 mA cm⁻², and (c) XRD patterns of samples with different calcinated time.

The LSV curves of samples under inert gas and air showed no obvious difference in the result (Figure 4.18a). To investigate the scan rate of LSV measurement effect on the OER performance, we gathered the LSV curves with a series of scan rates 1 ~ 20 mV s⁻¹ (Figure 4.18b). The outstanding OER performance was observed in the case of CoMnFeO₄ at 1 mV s⁻¹.

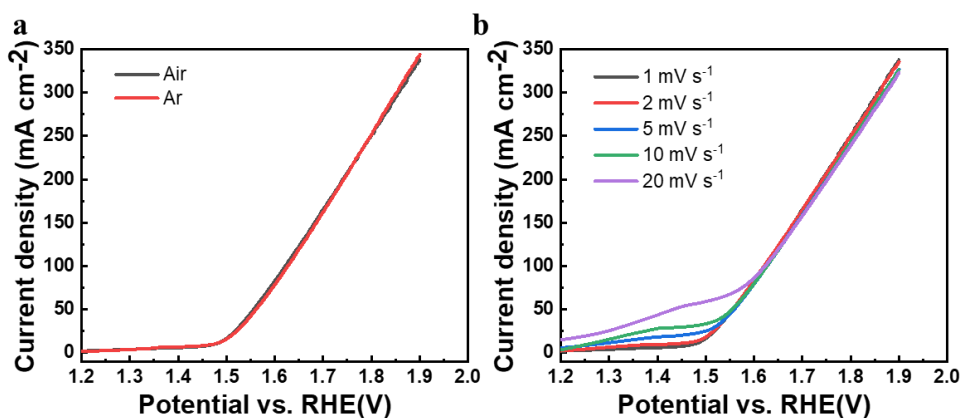


Figure 4.18 The LSV curves of samples at different calcinated atmospheres (a) and scan rates (b).

4.3.3 Electrocatalytic Activity for OER

The OER activities of CoMnFeO₄ were evaluated and compared with those of bare NF, and Co₂MnO₄. Figure 4.19a shows the OER LSV polarization curves of bare NF, Co₂MnO₄, and CoMnFeO₄. The OER overpotential of bare NF was 434 mV at 10 mA cm⁻², while the OER overpotential declined to 296 (for deposited Co₂MnO₄) and 242 mV (for deposited CoMnFeO₄)

to deliver the same current density. Moreover, the overpotential of CoMnFeO₄ (331 mV) was much lower than those of bare NF and Co₂MnO₄ (592 and 414 mV, respectively) at 50 mA cm⁻².

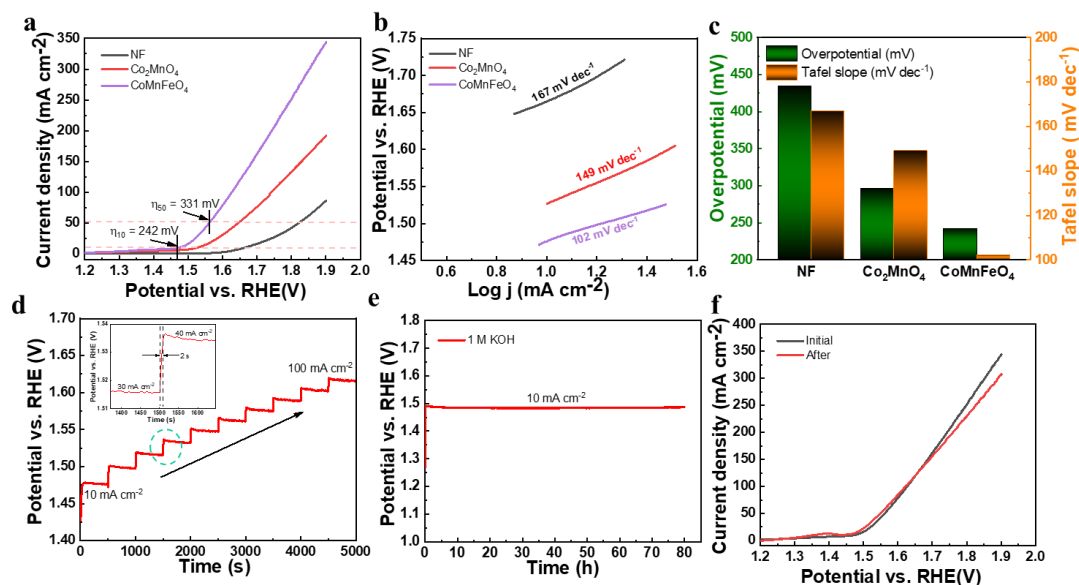


Figure 4. 19 (a) LSV polarization plots, (b) Corresponding Tafel curves, (c) Overpotential and Tafel slopes of bare NF, Co₂MnO₄, and CoMnFeO₄ at 10 mA cm⁻², (d) Multistep chronopotentiometry of CoMnFeO₄ at 10 ~ 100 mA cm⁻² for each 500 s, inset: enlarged region of green dotted line circle in Figure. 4. 19d, (e) Long-term stability measurement of CoMnFeO₄, and (f) LSV plots before and after 80 h stability test.

To further study the electrocatalytic kinetics of catalysts, the Tafel slopes of CoMnFeO₄, Co₂MnO₄, and bare NF were checked and determined to be 102, 149, and 167 mV dec⁻¹, respectively (**Figure 4. 19b**). Moreover, the smaller value of overpotential and Tafel slope of CoMnFeO₄ indicates more outstanding OER performance and faster reaction kinetics than the other electrodes (**Figure 4. 19c**). Therefore, OER performance has an order: CoMnFeO₄ > Co₂MnO₄ > bare NF. In practice, stability is another critical parameter for electrocatalysts. Chrono potentiometric measurement can be carried out to investigate the stability. **Figure 4. 19d** shows multistep Chrono potentiometry of CoMnFeO₄. It was observed that the corresponding potential was stable for each segment in the range of 10 ~ 100 mA cm⁻² with 10 mA cm⁻²

increment for each 500 s, suggesting that CoMnFeO₄ has superior mass and electron transportation. This prediction was also confirmed by a short response time (< 2 s) when current density shifted from low to high (inset of **Figure 4. 19d**, enlarged region of green dotted line circle in **Figure 4. 19d**). Moreover, the long-term stability of CoMnFeO₄ was performed for 80 hours at 10 mA cm⁻². Sample potential remained for 80 hours with a negligible increase (**Figure 4. 19e**). LSV curves after the long-term stability test for CoMnFeO₄ are displayed in **Figure 4. 19f**. These exhibited negligible decay of overpotential even after 80 hours.

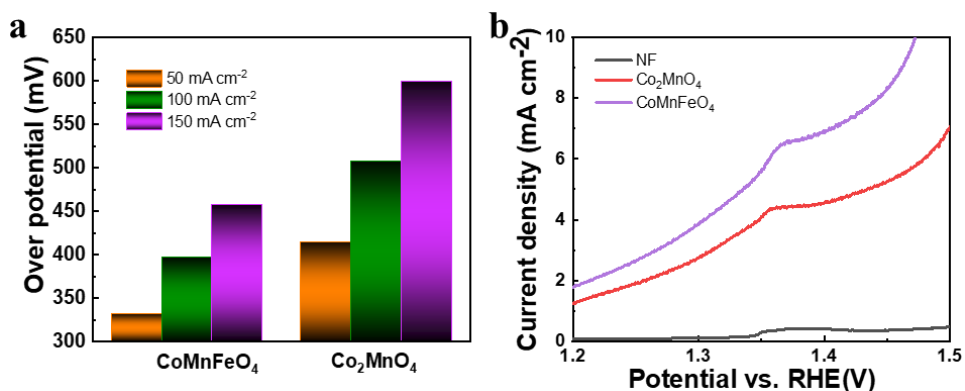


Figure 4. 20 (a) A comparison of overpotentials to reach different current densities for CoMnFeO₄ and Co₂MnO₄, (b) the LSV curves in the low current density range of CoMnFeO₄ and Co₂MnO₄.

A comparison of overpotentials to reach different current densities for CoMnFeO₄ and Co₂MnO₄ is displayed in **Figure 4. 20a**. It's observed that CoMnFeO₄ requires a lower overpotential than that of Co₂MnO₄ to reach 50, 100, and 150 mA cm⁻². As the current density increases, the requirement of overpotential increases. In addition, as presented in **Figure 4. 20b**, the LSV curves of the Co₂MnO₄ electrode possess a redox peak (~ 1.36 V), while the redox peak shifted to the positive direction (~ 1.37 V) in the case of CoMnFeO₄, suggesting that the addition of Fe may prevent the oxidation of Co²⁺ [46][113]. To note, CoMnFeO₄ exhibits outstanding electrocatalytic OER performance than those of the previously reported Co- or/ and Mn-based

oxides catalysts (Table 4. 7).

Table 4. 7 Electrochemical OER performances of the previously reported Co- or/ and Mn-based oxides catalysts.

Electrocatalysts	Electrolyte	η_{10} (mV)	η_{50} (mV)	Tafel slope (mV dec ⁻¹)	Reference
CoMnFeO ₄	1 M KOH	242	331	102	This work
Co ₂ MnO ₄	1 M KOH	296	414	142	This work
NiCo ₂ O ₄ nanosphere	1 M KOH	428	-	141	[136]
MnCo ₂ O ₄ microspheres	1 M KOH	510	-	55	[137]
MnCo ₂ O ₄ @NCNTs	0.1 M KOH	470	-	106	[138]
Ce-MnCo ₂ O ₄ -7%	1 M KOH	440	~ 570	156	[139]
Ce-MnCo ₂ O ₄ -1%	1 M KOH	430	~ 568	155	[139]
Mn ₂ O ₃ nanoplates	0.1 M KOH	420	-	81	[140]
MnCo ₂ O ₄	1M KOH	327	~ 385	79	[55]
Ce-MnCo ₂ O ₄ -3%	1 M KOH	390	~ 440	125	[139]

After the stability test, FE-SEM and XPS studies were carried out to check the changes in the morphology, chemical states, and composition (Figure 4. 21). The FE-SEM and TEM images exhibited only minor changes and damages on the edge of the nanosheets with well-preserved nanostructure, indicating good structural stability for the CoMnFeO₄ electrode (Figure 4. 21a). Furthermore, the XPS of the long period tested CoMnFeO₄ showed nearly the same spectra of every element as compared to the original one (Figure 4. 21b-f). It can be ascribed to the unique nanowire-nanosheets coexistence structure supported by porous Ni foam, which is beneficial for rapid desorption of gas, resulting in negligible destruction of nanostructure and change in the chemical composition and states [47].

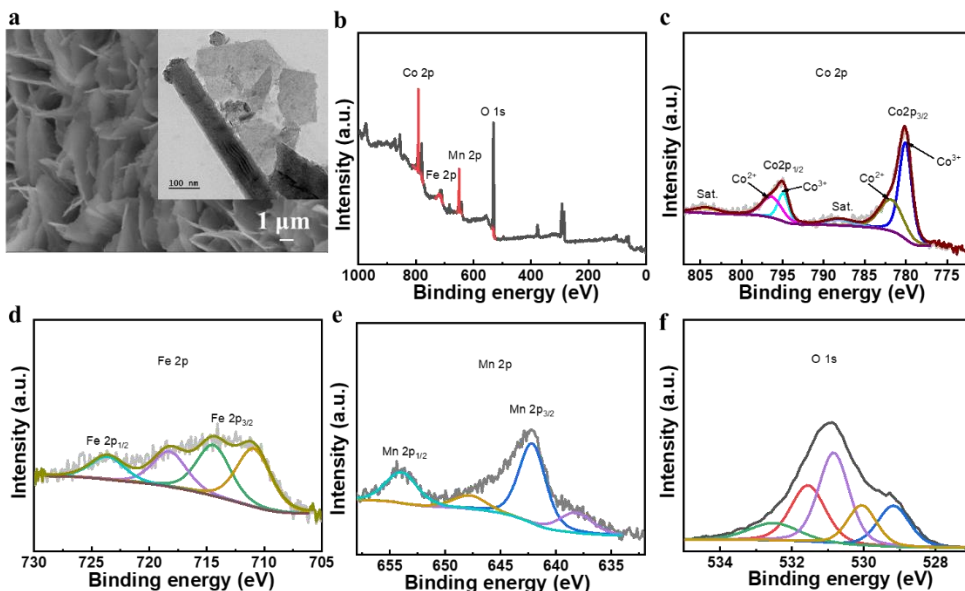


Figure 4. 21 (a) FE-SEM, inset TEM, and (b) XPS analyses of CoMnFeO₄ after stability test of 80 hours.

4.3.4 Origin of Superior OER activity

To investigate the origins of the excellent OER activity of catalysts, we compared the ECSA of CoMnFeO₄ and Co₂MnO₄ by determining their C_{d1} with a CV method (the equation is provided in chapter 2). In detail, the C_{d1} was estimated by measuring voltammograms at scan rates of 20 ~ 100 mV s⁻¹ (**Figure 4. 22 & 4. 23a**). As shown in **Figure 4.22f & 4. 23a**, the C_{d1} of the CoMnFeO₄ (27.2 mF cm⁻²) was 10.3, 8.5, 15.9 and 2.9 mF cm⁻² larger than that of CoMnFeO_{4-0.5} (17.0 mF cm⁻²), CoMnFeO_{4-1.0} (18.8 mF cm⁻²), CoMnFeO_{4-2.0} (11.4 mF cm⁻²), and Co₂MnO₄ (24.3 mF cm⁻²), respectively. It is suggesting bigger ECSA values for CoMnFeO₄ (680 cm⁻²) than that of CoMnFeO_{4-0.5} (425 cm⁻²), CoMnFeO_{4-1.0} (470 cm⁻²), CoMnFeO_{4-2.0} (285 cm⁻²) Co₂MnO₄ (607.5 cm⁻²). It suggests that a large amount of accessible active sites are present in CoMnFeO₄[141]. Furthermore, ECSA -normalized LSV plots were performed to estimate the intrinsic OER performance more reliably eliminating the effect of ECSA. In **Figure 4. 23b**, the CoMnFeO₄ exhibits a significantly larger current density in response than that of Co₂MnO₄ when

applied to the same potential, suggesting more excellent intrinsic OER performance of CoMnFeO_4 .

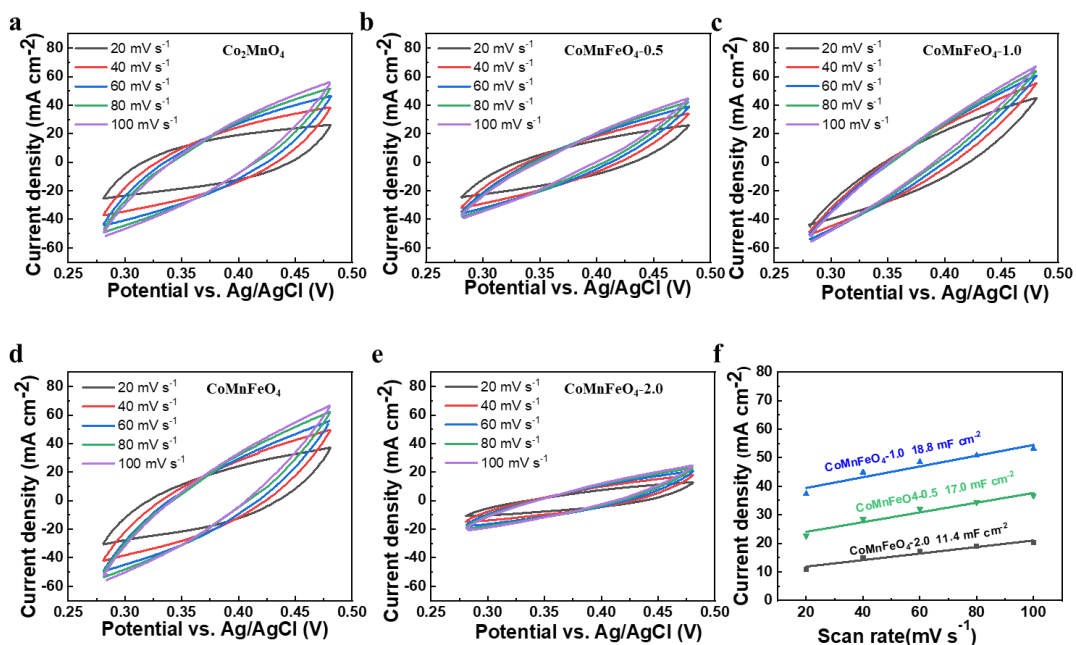


Figure 4. 22 (a-e) CV curves, (f) Curves of capacitive current density at different scan rates of $\text{CoMnFeO}_{4-0.5}$, $\text{CoMnFeO}_{4-1.0}$, and $\text{CoMnFeO}_{4-2.0}$.

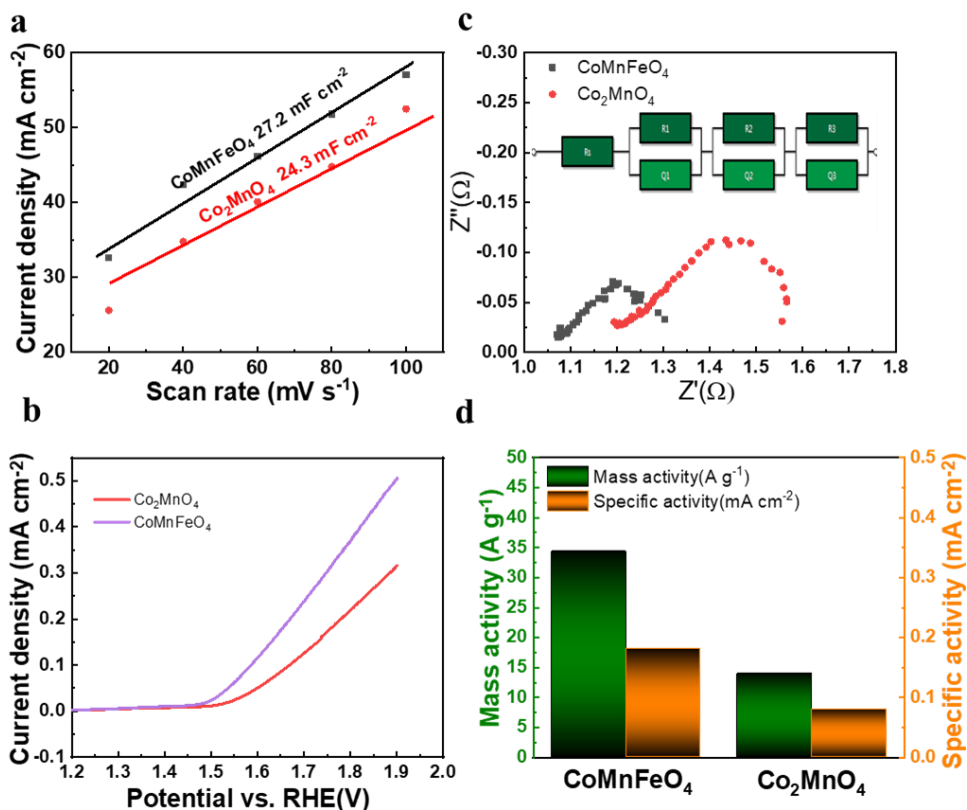


Figure 4. 23 (a) Curves of capacitive current density at different scan rates, (b) ECSA normalized LSV plots, (c) Nyquist plots, inset: a fitted equivalent circuit, and (d) MA and SA at a potential of 1.65 V.

EIS is another critical strategy to further evaluate the conductivity and electrocatalysis behavior of as-prepared samples. **Figure 4. 23c** show the Nyquist plot of all samples, along with a fitted equivalent circuit (inset of **Figure 4. 23c**). CoMnFeO₄ shows lower R_s ($\sim 1.07 \Omega$) and R_{ct} ($\sim 0.21 \Omega$) than Co₂MnO₄ (R_s - 1.19Ω and R_{ct} - 0.37Ω), which demonstrate a smaller transfer resistance and faster electron transfer of CoMnFeO₄. This may be ascribed to its trimetallic composition, the unique nanostructure of nanowire-nanosheets coexistence, and the high electroconductivity of porous NF substrate.[56] Moreover, the MA and SA of the electrodes were crucial evidence for outstanding OER activity. They were obtained according to the Equations provided in the experimental section. At a given potential of 1.65 V, the SA (0.18 mA cm^{-2}) and

MA (34.34 A g^{-1}) of CoMnFeO_4 were 2.25 and 2.45 times the corresponding results for Co_2MnO_4 (SA- 0.08 mA cm^{-2} , MA- 13.91 A g^{-1}), respectively (**Figure 4. 23d**). The SA of CoMnFeO_4 and Co_2MnO_4 were compared under the potential range of 1.50 to 1.68 V with a short interval of 0.02 V (**Figure 4. 24b**). It was observed that the SA of both samples increased with increasing given potentials, while the SA of CoMnFeO_4 showed higher values compared to that of Co_2MnO_4 under the same conditions, suggesting a high intrinsic OER activity.

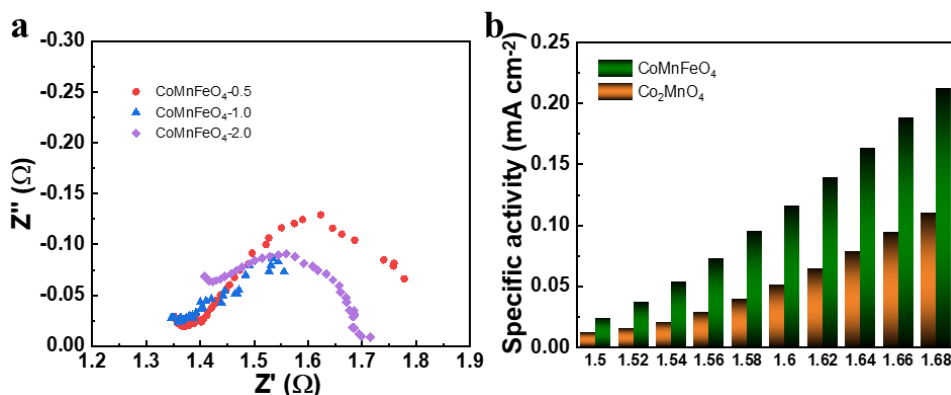


Figure 4. 24 (a) Nyquist plots of $\text{CoMnFeO}_4-0.5$, $\text{CoMnFeO}_4-1.0$, and $\text{CoMnFeO}_4-2.0$. (b) SA at a potential range of 1.50 to 1.68 V of CoMnFeO_4 and Co_2MnO_4 .

The electrocatalytic parameters of OER performances for all of the electrocatalysts were collected and displayed in the aforementioned **Table 4. 7**. In comparison to all the catalysts, CoMnFeO_4 exhibited an outstanding electrocatalytic activity. Herein, we try to conclude the essential understanding of OER related to the CoMnFeO_4 catalyst. Furthermore, the excellent OER activity originated from the following factors: (i) the unique nanowire-nanosheet structure, which supplied efficient catalytical active sites with a bigger ECSA; (ii) the direct deposition of CoMnFeO_4 on the porous NF substrate without binder, which made the nanowires and nanosheets well-aligned and prevented them from aggregation to enhance the electron transportation and favor oxygen evolution[88]; (iii) the excellent structural stability, which resulted from direct and close binding between NF substrate and catalysts which was not easy to peel off during the catalytic process; (iv) the altered electronic structure and adsorption energies of intermediates, which affected by the synergistic enhancement and interplay of additional cations in trimetallic electrocatalysts system[56,142,143]. Combining the aforementioned

advantages, the CoMnFeO_4 electrode was more superior electrocatalysts than Co_2MnO_4 .

In this section, to achieve a sufficiently high OER performance of $\text{M}_x\text{Mn}_y\text{O}_4$ samples, our present research focuses on not only fabricating $\text{Co}_x\text{Mn}_y\text{O}_4$ but also a series of $\text{Fe}_x\text{Mn}_y\text{O}_4$ and $\text{Ni}_x\text{Mn}_y\text{O}_4$. Through comparing the OER performances of $\text{Co}_x\text{Mn}_y\text{O}_4$, $\text{Fe}_x\text{Mn}_y\text{O}_4$, and $\text{Ni}_x\text{Mn}_y\text{O}_4$, it is distinctly observed that $\text{Co}_x\text{Mn}_y\text{O}_4$ precursor solution with a molar ratio of Co: Mn of 4: 1 and molar concentration of 4 mM exhibited a superior OER performance. Further, we demonstrated a unique nanostructure with nanowire-nanosheet coexistence of CoMnFeO_4 supported by NF prepared via a novel straightforward two-step synthesis route: HT method of CoMnFe-LDH precursor solution with Fe concentration of 1.5 mmol followed by calcination at 300 °C for 1 h in Ar. The as-prepared CoMnFeO_4 exhibited meaningfully boosted OER performance with a low overpotential of about 242 mV, and a low Tafel slope of 102 mV dec^{-1} at 10 mA cm^{-2} along with continuously stable catalysis for 80 hours. Furthermore, it only requires an overpotential of 331 mV for CoMnFeO_4 to reach 50 mA cm^{-2} . This can be attributed to unique nanostructure of nanowire-nanosheet coexistence, binder-free deposition, efficient exposed active sites, the synergistic effect of three different cations, excellent intrinsic performance, and the merit of combining with porous NF. It is expected that this work will offer a novel strategy for synthesizing the unique nanostructure of electrocatalyst for the enhanced electrocatalytic activity of OER.

5. Conclusion and Future Scope of Research

5.1 Conclusions

This thesis aimed to propose, synthesize, and evaluate nanostructured electrocatalyst of earth-abundant, low-cost transition metal compounds (e.g. CoMn-hydroxide and CoMnFe-oxide) for electrochemical water splitting, especially for OER, and HER. The activities of as-prepared catalysts were investigated for water electrolysis chemical reactions by using electrochemical techniques. Moreover, the important factors affecting preparation, the electrochemical performance of the catalytic process, the working mechanism, and related issues are discussed and demonstrated.

Section 3.2 describes the synthesis of the nanowire with core (CoMn-LDH) covered by a shell ($\text{Ni}(\text{OH})_2$) via HT and ED methods. Furthermore, the electrochemical water splitting performance of these efficient catalysts for OER and HER has been discussed in Section 4.2. The catalyst exhibited outstanding OER performance ($\eta_{30} = 250$ mV and Tafel slope = 102 mV dec^{-1}). These were remarkably lower than those of $\text{Ni}(\text{OH})_2$ (340 mV and 132 mV dec^{-1}), and CoMn-LDH (300 mV and 126 mV dec^{-1}). On another side, $\text{CoMn-LDH@Ni}(\text{OH})_2$ also showed a remarkable electrochemical catalytic activity towards HER ($\eta_{10} = 133$ mV and Tafel slope = 27 mV dec^{-1}). These were notably lower than those of $\text{Ni}(\text{OH})_2$ (223 mV, 37 mV dec^{-1}), and CoMn-LDH (187 mV and 158 mV dec^{-1}). Besides, $\text{CoMn-LDH@Ni}(\text{OH})_2$ remained stable for 25 hours. Utilizing two $\text{CoMn-LDH@Ni}(\text{OH})_2$ electrodes, the superior overall water electrolyzer was set up. It required an ultralow overall voltage of 1.68 V and stable catalysis for 25 hours at 10 mA cm^{-2} . The work reveals that reconstruction of hierarchical core-shell nanostructure provides the ease of OH^- adsorption and desorption of generated gases. Moreover, surface modification and synergistic effect between Co, Mn, and Ni positively affect enhance the catalytic activities

towards water electrolysis. From this study, we can obtain insights of assistance to serve this catalyst as a bifunctional catalyst for OER & HER.

In Section 3.3, the research strategy was focused on the fabrication of a series of $\text{Co}_x\text{Mn}_y\text{O}_4$, $\text{Fe}_x\text{Mn}_y\text{O}_4$, and $\text{Ni}_x\text{Mn}_y\text{O}_4$ catalysts to achieve high OER performance. Interestingly, $\text{Co}_x\text{Mn}_y\text{O}_4$, $\text{Fe}_x\text{Mn}_y\text{O}_4$, and $\text{Ni}_x\text{Mn}_y\text{O}_4$ exhibited different morphologies of a nanowire, nanowire-nanosheet dual structure, and nanosheet, respectively. In Section 4.3, as compared to the OER performances of $\text{Fe}_x\text{Mn}_y\text{O}_4$ and $\text{Ni}_x\text{Mn}_y\text{O}_4$, $\text{Co}_x\text{Mn}_y\text{O}_4$ precursor solution with a molar ratio of Co: Mn of 4: 1 and molar concentration of 4 mM exhibited superior OER performance. While, it was 1: 2 for Fe: Mn, and 7: 1 for Ni: Mn, at a molar concentration of 8 mM for $\text{Fe}_x\text{Mn}_y\text{O}_4$, and $\text{Ni}_x\text{Mn}_y\text{O}_4$, respectively. Further, we demonstrated a unique nanostructure with coexisting nanowire-nanosheet of CoMnFeO_4 supported on NF prepared by a novel and two-step fabrication route: an HT method for the fabrication of CoMnFe-LDH precursor followed by a calcination process. CoMnFeO_4 nanoarrays have been synthesized by varying the Fe concentration from 0 ~ 2 mmol, annealing temperature from 200 ~ 500 °C, and annealing time from 0.5 ~ 2 h. The effects of OER performance variation by changing Fe concentration and calcination condition were investigated. The results of this investigation have shown the optimal sample which was calcined in the Ar atmosphere at 300 °C for 1 h. XRD analysis confirmed that the optimal sample was poorly crystallized. Generally, catalyst in poor crystallization has numerous unsaturated active site and randomly oriented chemical bonds, which enhances the adsorption of reactants and desorption of byproducts and gases. Therefore, the as-prepared CoMnFeO_4 exhibited significantly enhanced OER performance ($\eta_{10} = 242$ mV and Tafel slope = 102 mV dec⁻¹), along with good stability (80 hours). It's observed that the catalytic activity of CoMnFeO_4 is relevant to the Fe concentration. With 1.5 mmol of Fe concentration, the electrical structure of the catalyst was modulated at a high-valent Mn oxidation rate. Taken together, these findings suggest that the coexistence of a unique interconnected nanowire-nanosheet structure that provides large ECSA and numerous active sites, poor crystallization which has abundant defects in the interfaces, binder-free deposition, the synergy of three different cations (Co, Mn, and Fe), excellent intrinsic performance, and the merit of combining with porous NF were the main reasons for superior OER activity.

Among these catalysts, CoMn-LDH@Ni(OH)_2 exhibits superior OER performance and gained particular attention for electrolysis of overall water splitting. In conclusion, this research

work provides an advanced strategy for synthesizing the unique nanostructure of electrocatalyst for the enhanced electrocatalytic activity of OER and HER and offers a wide scope for the simple synthesis of electrocatalysts based on multi-metal hydroxide and oxide to apply in ECWS. Expecting this work will be performed on another energy conversion/storage system.

5.2 Future Scope of Research

Based on the present study, we can perform the following work to enrich/reveal this field further.

- For TMH work, the long-term durability of CoMn-LDH@Ni(OH)₂ nanowires requires more investigations at large current densities (500~1000 mA cm⁻²). More electrochemical characterizations such as Turn over frequency and Faradic efficiency in terms of O₂ and H₂ generation should be monitored. In addition, the rate-determining step of the OER process and precise evidence of active sites should be investigated deeply and analyzed by Density Functional Theory analyses.
- For TMO work, the electrochemical characterizations including Turn over frequency and Faradic efficiency in terms of O₂ should be monitored. In addition, the overall water splitting system and urea electrolysis can be set up on CoMnFeO₄, then it can be employed for the fuel cell industry. Moreover, the performance of oxygen reduction reaction (ORR) even dehydrogenation, and H₂ peroxide reduction should be investigated to further explore potential applications.
- There are still opportunities for boosting the catalytic activity and apply forward the industrialization of ECWS more efficiently and quickly. Utilizing operando characterization such as in situ FE-SEM, TEM, and Raman for investigating crystal morphology and structure changes during electrochemical intermediates reaction. Even though operando techniques are high-cost and complicated, they are very necessary for systematically understanding the thermodynamic variations which happen on the intersurface between catalyst and electrolyte and identifying the catalysts' performance.

In summary, a more sophisticated analysis of the water electrolysis process of catalysts based on transition metal compounds is vastly required, involving detailed techno-economic analysis as the last step for wide-scaling purposes. However, using TMC as catalysts for water splitting has significant potential for green, sustainable, and high purity H₂ production with low cost and high efficiency.

ACKNOWLEDGEMENT

It is impossible to complete this doctoral work without help from the person surrounding me. I would first love to express my immense thanks to Prof. Young Tae Yoo (my research supervisor) for the most helpful supervision and warm encouragement. Thanks for providing me with indispensable laboratory equipment to carry out all the experiments. He has been an excellent adviser to me during my Ph.D. duration. His kind, loving heart, and expertise have moved me and made my research experience productive and valuable. His advice on research, career, and daily life has been priceless. I couldn't control myself to share with you that I feel lucky to be a number of his lab. Throughout my Ph.D., he created a very easygoing and welcoming atmosphere and gave me strong moral support and enough freedom to achieve the target that I established. Without his constant guidance and timely feedback, I would not be here.

My sincere thanks to the dissertation committee members for evaluating my dissertation. Their immense support and insightful comments have made my doctoral work valuable and memorable.

I owe my warm gratitude to my deeply loved parents. They showed their unconditional love, raised me independently, and allowed me to decide on my colorful life.

My deep gratitude goes to lab mates who always have been supportive of lab work. Thank you for their undeniable help and for providing wonderful fun lab time.

PUBLICATIONS

- (1) **Li, X.**; Patil, K.; Agarwal, A.; Babar, P.; Jang, J. S.; Chen, X.; Yoo, Y. T.; Kim, J. H. New J. Chem. 2022. <https://doi.org/10.1039/d1nj04792b>.
- (2) **Li, X.**; Ahmed, A.; Choi, B. S. J. Korean Inst. Met. Mater. 2021, 59 (11), 821–828. <https://doi.org/10.3365/KJMM.2021.59.11.821>.
- (3) **Li, X.**; Ring, T. A.; Choi, B. S. J. Korean Inst. Met. Mater. 2019, 57 (8), 529–534. <https://doi.org/10.3365/KJMM.2019.57.8.529>.
- (4) Zhu, W.; **Li, X.**; Shon, Y. M. Comput. Mater. Contin. 2020, 65 (1), 945–962. <https://doi.org/10.32604/cmc.2020.010089>.
- (5) Patil, K.; Babar, P.; **Li, X.**; Jang, J. S.; Kim, D.; Cheol Baek, M.; Bhoite, P.; Hyeok Kim, J. Mater. Lett. 2022, 310 (October 2021), 131409. <https://doi.org/10.1016/j.matlet.2021.131409>.
- (6) Jo, Y. D.; **Li, X.**; Cho, D. M.; Choi, B. S. J. Adv. Eng. Technol. 2019, 12 (2), 91–95. <https://doi.org/10.35272/jaet.2019.12.2.91>.
- (7) **Li, X.**; Choi, B. conference. Poster of 2019 KIM spring conference
- (8) **Li, X.**; Hussain, Z.; Choi, B. Poster of 2019 KIM autumn conference
- (9) **Li, X.**; Patil, K.; Babar, P.; Agarwal, A.; Chen, X.; Kim, D. M.; Kim, J. H.; Yoo, Y. T. Energy & Fuels.
- (10) **Li, X.**; Babar, P.; Patil, K.; Kale, S.; Jo, E.; Chen, X.; Hussain, Z.; Kim, J. H.; Yoo, Y. T.
- (11) Patil, K.; Babar, P.; **Li, X.**; Karade, V.; Kim, S.; Jang, S. Y.; Bhoite, P.; Kim, J. H.

- (12) Agarwal, A.; Li, X.; LiCoO₂ impregnated nano hierarchical HZSM₅ assisted catalytic upgrading of Kraft lignin derived liquefaction bio-oil. Biomass & Bioenergy. (under review)

MANUSCRIPT UNDER PREPARATION

- (13) Li, X.; Chen, X.; Kim, J. H.; Yoo, Y. T.. Hetero-nanostructured FeOOH coated CoMnP nanowires as a cocatalyst for efficient overall water splitting. (under preparation)
- (14) Li, X.; Chen, X.; Yoo, Y. T.; Kim, J. H.. Self-supported FeMnV-LTH nanosheets with enhanced performance for efficient water oxidation. (under preparation)

BIBLIOGRAPHY

- [1] R. Lee, The outlook for population growth, *Science* (80-.). 333 (2011) 569–573.
doi:10.1126/science.1208859.
- [2] M. Aresta, A. Dibenedetto, *The Carbon Dioxide Revolution - Challenges and Perspectives for a Global Society*, 2021.
- [3] <https://eneroutlook.enerdata.net/forecast-world-energy-primary-consumption.html>.
(2021) 1.
- [4] K. Singh, R. Rathore, S. Rai, *Review of Hydrogen-Based Energy Storage Techniques*,
(2021).
- [5] Royal Dutch shell (2012) *Sustainability Report*, 2012.
- [6] I.B. Franco, T. Chatterji, E. Derbyshire, J. Tracey, *Actioning the Global Goals for Local Impact*, 2020. <http://link.springer.com/10.1007/978-981-32-9927-6>.
- [7] S. McAllister, J.-Y. Chen, A.C. Fernandez-Pello, *Fundamentals of Combustion Processes*,
(2011) 1–13. doi:10.1007/978-1-4419-7943-8.
- [8] Eng. ToolBox https://www.engineeringtoolbox.com/fossil-57-fuels-energy-content-d_1298.html. (n.d.).
- [9] L. Li, P. Wang, Q. Shao, X. Huang, *Metallic nanostructures with low dimensionality for electrochemical water splitting*, *Chem. Soc. Rev.* 49 (2020) 3072–3106.
doi:10.1039/d0cs00013b.
- [10] X. Li, L. Zhao, J. Yu, X. Liu, X. Zhang, H. Liu, W. Zhou, *Water Splitting: From Electrode*

- to Green Energy System, *Nano-Micro Lett.* 12 (2020) 1–29. doi:10.1007/s40820-020-00469-3.
- [11] H. Sun, X. Xu, Y. Song, W. Zhou, Z. Shao, Designing High-Valence Metal Sites for Electrochemical Water Splitting, *Adv. Funct. Mater.* 31 (2021) 1–44. doi:10.1002/adfm.202009779.
- [12] M. Zeng, Y. Li, Recent advances in heterogeneous electrocatalysts for the hydrogen evolution reaction, *J. Mater. Chem. A* 3 (2015) 14942–14962. doi:10.1039/c5ta02974k.
- [13] W. Kreuter, H. Hofmann, Electrolysis: the important energy transformer in a world of sustainable energy, *Int. J. Hydrogen Energy*. 23 (1998) 661–666. doi:10.1016/S0360-3199(97)00109-2.
- [14] J.M. Olivares-Ramírez, M.L. Campos-Cornelio, J. Uribe Godínez, E. Borja-Arco, R.H. Castellanos, Studies on the hydrogen evolution reaction on different stainless steels, *Int. J. Hydrogen Energy*. 32 (2007) 3170–3173. doi:10.1016/j.ijhydene.2006.03.017.
- [15] S. Wang, A. Lu, C.J. Zhong, Hydrogen production from water electrolysis: role of catalysts, *Nano Converg.* 8 (2021). doi:10.1186/s40580-021-00254-x.
- [16] C. Hu, L. Zhang, J. Gong, Recent progress made in the mechanism comprehension and design of electrocatalysts for alkaline water splitting, *Energy Environ. Sci.* 12 (2019) 2620–2645. doi:10.1039/c9ee01202h.
- [17] F. Song, L. Bai, A. Moysiadou, S. Lee, C. Hu, L. Liardet, X. Hu, Transition Metal Oxides as Electrocatalysts for the Oxygen Evolution Reaction in Alkaline Solutions: An Application-Inspired Renaissance, *J. Am. Chem. Soc.* 140 (2018) 7748–7759. doi:10.1021/jacs.8b04546.

- [18] J. Zhu, L. Hu, P. Zhao, L.Y.S. Lee, K.Y. Wong, Recent Advances in Electrocatalytic Hydrogen Evolution Using Nanoparticles, *Chem. Rev.* 120 (2020) 851–918. doi:10.1021/acs.chemrev.9b00248.
- [19] M.S. Dresselhaus, I.L. Thomas, Alternative energy technologies. dresselhaus2001, *Nature*. 414 (2001) 332–337.
- [20] S. Kumaravel, K. Karthick, S.S. Sankar, A. Karmakar, R. Madhu, K. Bera, S. Kundu, Current progressions in transition metal based hydroxides as bi-functional catalysts towards electrocatalytic total water splitting, *Sustain. Energy Fuels*. 5 (2021) 6215–6268. doi:10.1039/d1se01193f.
- [21] N. Yuan, Q. Jiang, J. Li, J. Tang, A review on non-noble metal based electrocatalysis for the oxygen evolution reaction, *Arab. J. Chem.* 13 (2020) 4294–4309. doi:10.1016/j.arabjc.2019.08.006.
- [22] S.M. Ibn Shamsah, Earth-abundant electrocatalysts for water splitting: Current and future directions, *Catalysts*. 11 (2021). doi:10.3390/catal11040429.
- [23] M.I. Jamesh, X. Sun, Recent progress on earth abundant electrocatalysts for oxygen evolution reaction (OER) in alkaline medium to achieve efficient water splitting – A review, *J. Power Sources*. 400 (2018) 31–68. doi:10.1016/j.jpowsour.2018.07.125.
- [24] V. Vij, S. Sultan, A.M. Harzandi, A. Meena, J.N. Tiwari, W.G. Lee, T. Yoon, K.S. Kim, Nickel-based electrocatalysts for energy-related applications: Oxygen reduction, oxygen evolution, and hydrogen evolution reactions, *ACS Catal.* 7 (2017) 7196–7225. doi:10.1021/acscatal.7b01800.
- [25] C. Zhang, J. Zhao, L. Zhou, Z. Li, M. Shao, M. Wei, Layer-by-layer assembly of

- exfoliated layered double hydroxide nanosheets for enhanced electrochemical oxidation of water, *J. Mater. Chem. A*. 4 (2016) 11516–11523. doi:10.1039/c6ta02537d.
- [26] J. Kibsgaard, Z. Chen, B.N. Reinecke, T.F. Jaramillo, Engineering the surface structure of MoS₂ to preferentially expose active edge sites for electrocatalysis, *Nat. Mater.* 11 (2012) 963–969. doi:10.1038/nmat3439.
- [27] D. Jiang, W. Ma, R. Yang, B. Quan, D. Li, S. Meng, M. Chen, Nickel–manganese bimetallic phosphides porous nanosheet arrays as highly active bifunctional hydrogen and oxygen evolution electrocatalysts for overall water splitting, *Electrochim. Acta*. 329 (2020). doi:10.1016/j.electacta.2019.135121.
- [28] A. Dutta, N. Pradhan, Developments of Metal Phosphides as Efficient OER Precatalysts, *J. Phys. Chem. Lett.* 8 (2017) 144–152. doi:10.1021/acs.jpcclett.6b02249.
- [29] M. Sun, H. Liu, J. Qu, J. Li, Earth-Rich Transition Metal Phosphide for Energy Conversion and Storage, *Adv. Energy Mater.* 6 (2016). doi:10.1002/aenm.201600087.
- [30] M.R. Gao, J.X. Liang, Y.R. Zheng, Y.F. Xu, J. Jiang, Q. Gao, J. Li, S.H. Yu, An efficient molybdenum disulfide/cobalt diselenide hybrid catalyst for electrochemical hydrogen generation, *Nat. Commun.* 6 (2015). doi:10.1038/ncomms6982.
- [31] J.A. Rajesh, Y.H. Lee, Y.H. Yun, V.H. Vinh Quy, S.H. Kang, H. Kim, K.S. Ahn, Bifunctional NiCo₂Se₄ and CoNi₂Se₄ nanostructures: Efficient electrodes for battery-type supercapacitors and electrocatalysts for the oxygen evolution reaction, *J. Ind. Eng. Chem.* 79 (2019) 370–382. doi:10.1016/j.jiec.2019.07.013.
- [32] M. Cui, X. Bai, J. Zhu, C. Han, Y. Huang, L. Kang, C. Zhi, H. Li, Electrochemically induced NiCoSe₂@NiOOH/CoOOH heterostructures as multifunctional cathode

- materials for flexible hybrid zn batteries, *Energy Storage Mater.* 36 (2021) 427–434. doi:10.1016/j.ensm.2021.01.015.
- [33] H. Liang, F. Meng, M. Cabán-Acevedo, L. Li, A. Forticaux, L. Xiu, Z. Wang, S. Jin, Hydrothermal continuous flow synthesis and exfoliation of NiCo layered double hydroxide nanosheets for enhanced oxygen evolution catalysis, *Nano Lett.* 15 (2015) 1421–1427. doi:10.1021/nl504872s.
- [34] L. Feng, A. Li, Y. Li, J. Liu, L. Wang, L. Huang, Y. Wang, X. Ge, A Highly Active CoFe Layered Double Hydroxide for Water Splitting, *Chempluschem.* 82 (2017) 483–488. doi:10.1002/cplu.201700005.
- [35] K. Patil, P. Babar, D.M. Lee, V. Karade, E. Jo, S. Korade, J.H. Kim, Bifunctional catalytic activity of Ni-Co layered double hydroxide for the electro-oxidation of water and methanol, *Sustain. Energy Fuels.* 4 (2020) 5254–5263. doi:10.1039/d0se00899k.
- [36] P. Babar, K. Patil, D.M. Lee, V. Karade, K. Gour, S. Pawar, J.H. Kim, Cost-effective and efficient water and urea oxidation catalysis using nickel-iron oxyhydroxide nanosheets synthesized by an ultrafast method, *J. Colloid Interface Sci.* 584 (2021) 760–769. doi:10.1016/j.jcis.2020.09.108.
- [37] L. Yu, H. Zhou, J. Sun, I.K. Mishra, D. Luo, F. Yu, Y. Yu, S. Chen, Z. Ren, Amorphous NiFe layered double hydroxide nanosheets decorated on 3D nickel phosphide nanoarrays: a hierarchical core-shell electrocatalyst for efficient oxygen evolution, *J. Mater. Chem. A.* 6 (2018) 13619–13623. doi:10.1039/c8ta02967a.
- [38] L. Hu, M. Li, X. Wei, H. Wang, Y. Wu, J. Wen, W. Gu, C. Zhu, Modulating interfacial electronic structure of CoNi LDH nanosheets with Ti₃C₂T_x MXene for enhancing water

- oxidation catalysis, *Chem. Eng. J.* 398 (2020) 1–6. doi:10.1016/j.cej.2020.125605.
- [39] J. Zhou, L. Yu, Q. Zhu, C. Huang, Y. Yu, Defective and ultrathin NiFe LDH nanosheets decorated on V-doped Ni₃S₂ nanorod arrays: A 3D core-shell electrocatalyst for efficient water oxidation, *J. Mater. Chem. A.* 7 (2019) 18118–18125. doi:10.1039/c9ta06347a.
- [40] P. Wang, J. Qi, C. Li, W. Li, T. Wang, C. Liang, Hierarchical CoNi₂S₄@NiMn-layered double hydroxide heterostructure nanoarrays on superhydrophilic carbon cloth for enhanced overall water splitting, *Electrochim. Acta.* 345 (2020) 1–11. doi:10.1016/j.electacta.2020.136247.
- [41] N.K. Chaudhari, H. Jin, B. Kim, K. Lee, Nanostructured materials on 3D nickel foam as electrocatalysts for water splitting, *Nanoscale.* 9 (2017) 12231–12247. doi:10.1039/c7nr04187j.
- [42] P. Wang, T. Jia, B. Wang, A critical review: 1D/2D nanostructured self-supported electrodes for electrochemical water splitting, *J. Power Sources.* 474 (2020) 228621. doi:10.1016/j.jpowsour.2020.228621.
- [43] X. Yin, L. Yang, Q. Gao, Core-shell nanostructured electrocatalysts for water splitting, *Nanoscale.* 12 (2020) 15944–15969. doi:10.1039/d0nr03719b.
- [44] Z. Liu, C. Yu, X. Han, J. Yang, C. Zhao, H. Huang, J. Qiu, CoMn Layered Double Hydroxides/Carbon Nanotubes Architectures as High-Performance Electrocatalysts for the Oxygen Evolution Reaction, *ChemElectroChem.* 3 (2016) 906–912. doi:10.1002/celec.201600116.
- [45] M.P. Suryawanshi, U. V. Ghorpade, S.W. Shin, U.P. Suryawanshi, E. Jo, J.H. Kim, Hierarchically Coupled Ni:FeOOH Nanosheets on 3D N-Doped Graphite Foam as Self-

- Supported Electrocatalysts for Efficient and Durable Water Oxidation, *ACS Catal.* 9 (2019) 5025–5034. doi:10.1021/acscatal.9b00492.
- [46] P. Babar, K. Patil, V. Karade, K. Gour, A. Lokhande, S. Pawar, J.H. Kim, In Situ Fabrication of Nickel-Iron Oxalate Catalysts for Electrochemical Water Oxidation at High Current Densities, *ACS Appl. Mater. Interfaces.* 13 (2021) 52620–52628. doi:10.1021/acsami.1c14742.
- [47] Q. Kong, W. Bai, F. Bai, X. An, W. Feng, F. Zhou, Q. Chen, Q. Wang, C. Sun, FeCoNi Ternary Spinel Oxides Nanosheets as High Performance Water Oxidation Electrocatalyst, *ChemCatChem.* 12 (2020) 2209–2214. doi:10.1002/cctc.202000004.
- [48] S.M. Pawar, A.T. Aqueel Ahmed, C.H. Lee, P.T. Babar, J.H. Kim, S.U. Lee, H. Kim, H. Im, Experimental and Theoretical Insights into Transition-Metal (Mo, Fe) Codoping in a Bifunctional Nickel Phosphide Microsphere Catalyst for Enhanced Overall Water Splitting, *ACS Appl. Energy Mater.* 4 (2021) 14169–14179. doi:10.1021/acsaem.1c02930.
- [49] X. Li, K. Patil, A. Agarwal, P. Babar, J.S. Jang, X. Chen, Y.T. Yoo, J.H. Kim, Ni(OH)₂ Coated CoMn-layered double hydroxide nanowires as efficient water oxidation electrocatalysts, *New J. Chem.* 46 (2022) 2044–2052. doi:10.1039/d1nj04792b.
- [50] S. Periyasamy, P. Subramanian, E. Levi, D. Aurbach, A. Gedanken, A. Schechter, Exceptionally Active and Stable Spinel Nickel Manganese Oxide Electrocatalysts for Urea Oxidation Reaction, *ACS Appl. Mater. Interfaces.* 8 (2016) 12176–12185. doi:10.1021/acsami.6b02491.
- [51] P. Babar, K. Patil, P. Bhoite, S. Pawar, J. Hyeok Kim, 1D iron cobaltite electrode for

- efficient electrochemical water oxidation, *Mater. Lett.* 312 (2022) 131663.
doi:10.1016/j.matlet.2022.131663.
- [52] S. Peng, L. Li, Y. Hu, M. Srinivasan, F. Cheng, J. Chen, S. Ramakrishna, Fabrication of spinel one-dimensional architectures by single-spinneret electrospinning for energy storage applications, *ACS Nano*. 9 (2015) 1945–1954. doi:10.1021/nn506851x.
- [53] N. Garg, M. Mishra, Govind, A.K. Ganguli, Electrochemical and magnetic properties of nanostructured CoMn_2O_4 and Co_2MnO_4 , *RSC Adv.* 5 (2015) 84988–84998. doi:10.1039/c5ra16937b.
- [54] P.W. Menezes, A. Indra, O. Levy, K. Kailasam, V. Gutkin, J. Pfrommer, M. Driess, Using nickel manganese oxide catalysts for efficient water oxidation, *Chem. Commun.* 51 (2015) 5005–5008. doi:10.1039/c4cc09671a.
- [55] K. Lankauf, K. Cysewska, J. Karczewski, A. Mielewczyk-Gryń, K. Górnicka, G. Cempura, M. Chen, P. Jasiński, S. Molin, $\text{Mn}_x\text{Co}_{3-x}\text{O}_4$ spinel oxides as efficient oxygen evolution reaction catalysts in alkaline media, *Int. J. Hydrogen Energy*. 45 (2020) 14867–14879. doi:10.1016/j.ijhydene.2020.03.188.
- [56] S. Peng, F. Gong, L. Li, D. Yu, D. Ji, T. Zhang, Z. Hu, Z. Zhang, S. Chou, Y. Du, S. Ramakrishna, Necklace-like Multishelled Hollow Spinel Oxides with Oxygen Vacancies for Efficient Water Electrolysis, *J. Am. Chem. Soc.* 140 (2018) 13644–13653. doi:10.1021/jacs.8b05134.
- [57] G. Zhu, X. Xie, X. Li, Y. Liu, X. Shen, K. Xu, S. Chen, Nanocomposites Based on CoSe_2 -Decorated FeSe_2 Nanoparticles Supported on Reduced Graphene Oxide as High-Performance Electrocatalysts toward Oxygen Evolution Reaction, *ACS Appl. Mater.*

- Interfaces. 10 (2018) 19258–19270. doi:10.1021/acsami.8b04024.
- [58] H.F. Wang, C. Tang, Q. Zhang, A Review of Precious-Metal-Free Bifunctional Oxygen Electrocatalysts: Rational Design and Applications in Zn–Air Batteries, *Adv. Funct. Mater.* 28 (2018) 1–22. doi:10.1002/adfm.201803329.
- [59] J. Wang, X. Yue, Y. Yang, S. Sirisomboonchai, P. Wang, X. Ma, A. Abudula, G. Guan, Earth-abundant transition-metal-based bifunctional catalysts for overall electrochemical water splitting: A review, *J. Alloys Compd.* 819 (2020) 153346. doi:10.1016/j.jallcom.2019.153346.
- [60] W. Liu, D. Cao, D. Cheng, Review on Synthesis and Catalytic Coupling Mechanism of Highly Active Electrocatalysts for Water Splitting, *Energy Technol.* 9 (2021) 1–23. doi:10.1002/ente.202000855.
- [61] Y.X. Gan, A.H. Jayatissa, Z. Yu, X. Chen, M. Li, Hydrothermal Synthesis of Nanomaterials, *J. Nanomater.* 2020 (2020). doi:10.1155/2020/8917013.
- [62] M.L.M. Napi, S.M. Sultan, R. Ismail, M.K. Ahmad, G.M.T. Chai, Optimization of a hydrothermal growth process for low resistance 1d fluorine-doped zinc oxide nanostructures, *J. Nanomater.* 2019 (2019). doi:10.1155/2019/4574507.
- [63] L. Ma, Z. Wei, X. Zhu, J. Liang, X. Zhang, Synthesis and photocatalytic properties of co-doped $Zn_{1-x}Co_xMn_2O$ hollow nanospheres, *J. Nanomater.* 2019 (2019). doi:10.1155/2019/4257270.
- [64] <https://books.google.co.kr/books?hl=en&lr=&id=asA3BQAAQBAJ&oi=fnd&pg=PP1&dq=Electrodeposition+&ots=-DCg6z3BUn&sig=LAthoFm568tZYmKjSC0RY7dj1>

Ak#v=onpage&q=Electrodeposition&f=false, n.d.

- [65] U. Erb, Electrodeposited nanocrystals: Synthesis, properties and industrial applications, *Nanostructured Mater.* 6 (1995) 533–538. doi:10.1016/0965-9773(95)00114-X.
- [66] E. Hatami, A. Toghraei, G. Barati Darband, Electrodeposition of Ni–Fe micro/nano urchin-like structure as an efficient electrocatalyst for overall water splitting, *Int. J. Hydrogen Energy.* 46 (2021) 9394–9405. doi:10.1016/j.ijhydene.2020.12.110.
- [67] H. Feng, X. Sun, X. Guan, D. Zheng, W. Tian, C. Li, C. Li, M. Yan, Y. Yao, Construction of interfacial engineering on CoP nanowire arrays with CoFe-LDH nanosheets for enhanced oxygen evolution reaction, *FlatChem.* 26 (2021) 100225. doi:10.1016/j.flatc.2021.100225.
- [68] T. Han, L. Wu, P. Wang, T. Wang, Z. Yang, K. Tian, J. Jin, Room chemical bath temperature deposition of Mn:FeOOH on BiVO₄ photoanode to enhance water oxidation, *J. Alloys Compd.* 894 (2022) 162571. doi:10.1016/j.jallcom.2021.162571.
- [69] J.A. Switzer, G. Hodes, Electrodeposition and chemical bath deposition of functional nanomaterials, *MRS Bull.* 35 (2010) 743–750. doi:10.1557/s0883769400051253.
- [70] D.P. Dubal, R. Holze, P. Gomez-Romero, Development of hybrid materials based on sponge supported reduced graphene oxide and transition metal hydroxides for hybrid energy storage devices, *Sci. Rep.* 4 (2014) 1–10. doi:10.1038/srep07349.
- [71] F.G. Hone, T. Abza, Short review of factors affecting chemical bath deposition method for metal chalcogenide thin films, *Int. J. Thin Film Sci. Technol.* 8 (2019) 43–52. doi:10.18576/ijtfst/080203.
- [72] D. Briggs, X-ray photoelectron spectroscopy (XPS), *Handb. Adhes.* Second Ed. (2005)

- 621–622. doi:10.1002/0470014229.ch22.
- [73] B.D. Cullity, *Elements of X-ray Diffraction*, Addition-Wesley Publishing, 1956.
- [74] B.J. Inkson, *Scanning electron microscopy (SEM) and transmission electron microscopy (TEM) for materials characterization, Mater. Charact. Using Nondestruct. Eval. Methods.* (2016) 17–43.
- [75] D. Zhou, Weilie and Apkarian, Robert and Wang, Zhong Lin and Joy, *Fundamentals of scanning electron microscopy (SEM)*, in: *Scanning Microsc. Nanotechnol.*, Springer, 2006: pp. 1–40.
- [76] A. Abdullah, A. Mohammed, *Scanning Electron Microscopy (SEM): A Review* *Scanning Electron Microscopy (SEM): A Review*, *Int. Conf. Hydraul. Pneum.* (2019) 1–9.
- [77] D. Zhang, Y. Zhu, L. Liu, X. Ying, C.E. Hsiung, R. Sougrat, K. Li, Y. Han, *Atomic-resolution transmission electron microscopy of electron beam-sensitive crystalline materials*, *Science* (80-.). 359 (2018) 675–679. doi:10.1126/science.aao0865.
- [78] R.R. Jones, D.C. Hooper, L. Zhang, D. Wolverson, V.K. Valev, *Raman Techniques: Fundamentals and Frontiers*, *Nanoscale Res. Lett.* 14 (2019). doi:10.1186/s11671-019-3039-2.
- [79] W.D. Perkins, *Fourier transform infrared spectroscopy. Part II. Advantages of FT-IR*, *J. Chem. Educ.* 64 (1987) A269. doi:10.1021/ed064pa269.
- [80] J.R. Ferraro, *Practical Fourier transform infrared spectroscopy: industrial and laboratory chemical analysis*, Elsevier, 2012.

- [81] S. Anantharaj, S. Kundu, Do the Evaluation Parameters Reflect Intrinsic Activity of Electrocatalysts in Electrochemical Water Splitting?, *ACS Energy Lett.* 4 (2019) 1260–1264. doi:10.1021/acsenergylett.9b00686.
- [82] A.J.B. and L. Faulkner, *Electrochemical Methods: Fundamentals and Applications*, John Wiley & son, 2001.
- [83] T. Gueshi, K. Tokuda, H. Matsuda, Voltammetry at partially covered electrodes. Part I. Chronopotentiometry and chronoamperometry at model electrodes, *J. Electroanal. Chem.* 89 (1978) 247–260. doi:10.1016/S0022-0728(78)80188-0.
- [84] J.J. Van Benschoten, J.Y. Lewis, W.R. Heineman, D.A. Roston, P.T. Kissinger, Cyclic voltammetry experiment, *J. Chem. Educ.* 60 (1983) 772–776. doi:10.1021/ed060p772.
- [85] N. Sekar, R.P. Ramasamy, Electrochemical impedance spectroscopy for microbial fuel cell characterization, *J. Microb. Biochem. Technol.* 5 (2013). doi:10.4172/1948-5948.s6-004.
- [86] W. Choi, H.C. Shin, J.M. Kim, J.Y. Choi, W.S. Yoon, Modeling and applications of electrochemical impedance spectroscopy (Eis) for lithium-ion batteries, *J. Electrochem. Sci. Technol.* 11 (2020) 1–13. doi:10.33961/jecst.2019.00528.
- [87] X. Lin, H. Li, F. Musharavati, E. Zalnezhad, S. Bae, B.Y. Cho, O.K.S. Hui, Synthesis and characterization of cobalt hydroxide carbonate nanostructures, *RSC Adv.* 7 (2017) 46925–46931. doi:10.1039/c7ra09050a.
- [88] M. Guo, L. Zhou, Y. Li, Q. Zheng, F. Xie, D. Lin, Unique nanosheet-nanowire structured CoMnFe layered triple hydroxide arrays as self-supporting electrodes for a high-efficiency oxygen evolution reaction, *J. Mater. Chem. A.* 7 (2019) 13130–13141.

- doi:10.1039/c9ta01531k.
- [89] S. Fan, J. Zhang, Q. Wu, S. Huang, J. Zheng, D. Kong, S. Chen, Y. Wang, L.K. Ang, Y. Shi, H.Y. Yang, Morphological and Electronic Dual Regulation of Cobalt-Nickel Bimetal Phosphide Heterostructures Inducing High Water-Splitting Performance, *J. Phys. Chem. Lett.* 11 (2020) 3911–3919. doi:10.1021/acs.jpcelett.0c00851.
- [90] J.O. Abe, A.P.I. Popoola, E. Ajenifuja, O.M. Popoola, Hydrogen energy, economy, and storage: Review and recommendation, *Int. J. Hydrogen Energy.* 44 (2019) 15072–15086. doi:10.1016/j.ijhydene.2019.04.068.
- [91] X. Hu, X. Tian, Y.W. Lin, Z. Wang, Nickel foam and stainless steel mesh as electrocatalysts for hydrogen evolution reaction, oxygen evolution reaction and overall water splitting in alkaline media, *RSC Adv.* 9 (2019) 31563–31571. doi:10.1039/c9ra07258f.
- [92] M. Arif, G. Yasin, M. Shakeel, X. Fang, R. Gao, S. Ji, D. Yan, Coupling of Bifunctional CoMn-Layered Double Hydroxide@Graphitic C₃N₄ Nanohybrids towards Efficient Photoelectrochemical Overall Water Splitting, *Chem. - An Asian J.* 13 (2018) 1045–1052. doi:10.1002/asia.201800016.
- [93] Z. Wang, S. Zeng, W. Liu, X. Wang, Q. Li, Z. Zhao, F. Geng, Coupling molecularly ultrathin sheets of NiFe-layered double hydroxide on NiCo₂O₄ nanowire arrays for highly efficient overall water-splitting activity, *ACS Appl. Mater. Interfaces.* 9 (2017) 1488–1495. doi:10.1021/acsami.6b13075.
- [94] M. Guo, M. He, X. Li, Q. Zheng, F. Xie, C. Xu, D. Lin, CoMnFe hydroxysulfide nanowire@Ni(OH)₂ nanorod arrays as self-supporting electrodes for high-efficiency

- oxygen evolution reaction, *Electrochim. Acta.* 356 (2020).
doi:10.1016/j.electacta.2020.136793.
- [95] F.O. Ochai-Ejeh, M.J. Madito, D.Y. Momodu, A.A. Khaleed, O. Olaniyan, N. Manyala, High-performance hybrid supercapacitor device based on cobalt manganese layered double hydroxide and activated carbon derived from cork (*Quercus Suber*), *Electrochim. Acta.* 252 (2017) 41–54. doi:10.1016/j.electacta.2017.08.163.
- [96] T. Nogueira, N. Gonçalves, R. Botan, F. Wypych, L. Lona, Layered double hydroxides as fillers in poly(l-lactide) nanocomposites, obtained by in situ bulk polymerization, *Polimeros.* 26 (2016) 106–114. doi:10.1590/0104-1428.2282.
- [97] G. Abellán, J.A. Carrasco, E. Coronado, J. Romero, M. Varela, Alkoxide-intercalated CoFe-layered double hydroxides as precursors of colloidal nanosheet suspensions: Structural, magnetic and electrochemical properties, *J. Mater. Chem. C.* 2 (2014) 3723–3731. doi:10.1039/c3tc32578d.
- [98] J. Zhao, J. Chen, S. Xu, M. Shao, D. Yan, M. Wei, D.G. Evans, X. Duan, CoMn-layered double hydroxide nanowalls supported on carbon fibers for high-performance flexible energy storage devices, *J. Mater. Chem. A.* 1 (2013) 8836–8843. doi:10.1039/c3ta11452j.
- [99] J. Tian, Y. Xue, X. Yu, Y. Pei, H. Zhang, J. Wang, 2D nanoporous Ni(OH)₂ film as an electrode material for high-performance energy storage devices, *RSC Adv.* 9 (2019) 17706–17716. doi:10.1039/c9ra02034a.
- [100] T. Tang, W.J. Jiang, S. Niu, N. Liu, H. Luo, Y.Y. Chen, S.F. Jin, F. Gao, L.J. Wan, J.S. Hu, Electronic and Morphological Dual Modulation of Cobalt Carbonate Hydroxides by Mn Doping toward Highly Efficient and Stable Bifunctional Electrocatalysts for Overall

- Water Splitting, *J. Am. Chem. Soc.* 139 (2017) 8320–8328. doi:10.1021/jacs.7b03507.
- [101] F. Yan, D. Guo, J. Kang, L. Liu, C. Zhu, P. Gao, X. Zhang, Y. Chen, Fast fabrication of ultrathin CoMn LDH nanoarray as flexible electrode for water oxidation, *Electrochim. Acta.* 283 (2018) 755–763. doi:10.1016/j.electacta.2018.06.202.
- [102] L. Yang, L. Chen, D. Yang, X. Yu, H. Xue, L. Feng, NiMn layered double hydroxide nanosheets/NiCo₂O₄ nanowires with surface rich high valence state metal oxide as an efficient electrocatalyst for oxygen evolution reaction, *J. Power Sources.* 392 (2018) 23–32. doi:10.1016/j.jpowsour.2018.04.090.
- [103] M. Gong, Y. Li, H. Wang, Y. Liang, J.Z. Wu, J. Zhou, J. Wang, T. Regier, F. Wei, H. Dai, An advanced Ni-Fe layered double hydroxide electrocatalyst for water oxidation, *J. Am. Chem. Soc.* 135 (2013) 8452–8455. doi:10.1021/ja4027715.
- [104] Z. Liu, C. Yu, X. Han, J. Yang, C. Zhao, H. Huang, J. Qiu, CoMn Layered Double Hydroxides/Carbon Nanotubes Architectures as High-Performance Electrocatalysts for the Oxygen Evolution Reaction, *ChemElectroChem.* 3 (2016) 906–912. doi:10.1002/CELC.201600116.
- [105] M.C. Biesinger, B.P. Payne, A.P. Grosvenor, L.W.M. Lau, A.R. Gerson, R.S.C. Smart, Resolving surface chemical states in XPS analysis of first row transition metals, oxides, and hydroxides: Cr, Mn, Fe, Co and Ni, *Appl. Surf. Sci.* 257 (2011) 2717–2730. doi:10.1016/j.apsusc.2010.10.051.
- [106] P. Babar, K. Patil, D.M. Lee, V. Karade, K. Gour, S. Pawar, J.H. Kim, Cost-effective and efficient water and urea oxidation catalysis using nickel-iron oxyhydroxide nanosheets synthesized by an ultrafast method, *J. Colloid Interface Sci.* 584 (2021) 760–769.

- doi:10.1016/j.jcis.2020.09.108.
- [107] D. Chen, H. Chen, X. Chang, P. Liu, Z. Zhao, J. Zhou, G. Xu, H. Lin, S. Han, Hierarchical CoMn-layered double hydroxide nanowires on nickel foam as electrode material for high-capacitance supercapacitor, *J. Alloys Compd.* 729 (2017) 866–873. doi:10.1016/j.jallcom.2017.07.313.
- [108] P. Babar, K. Patil, V. Karade, K. Gour, A. Lokhande, S. Pawar, J.H. Kim, In Situ Fabrication of Nickel–Iron Oxalate Catalysts for Electrochemical Water Oxidation at High Current Densities, *ACS Appl. Mater. Interfaces.* 13 (2021) 52620–52628. doi:10.1021/acsami.1c14742.
- [109] M. Guo, L. Zhou, Y. Li, Q. Zheng, F. Xie, D. Lin, Unique nanosheet-nanowire structured CoMnFe layered triple hydroxide arrays as self-supporting electrodes for a high-efficiency oxygen evolution reaction, *J. Mater. Chem. A.* 7 (2019) 13130–13141. doi:10.1039/c9ta01531k.
- [110] M.E. Dos Santos, A. Castro, I. Martinez, P. Noronha Lisboa-Filho, O. Peña, Mechano-synthesis of the multiferroic cubic spinel Co_2MnO_4 : Influence of the calcination temperature, *Ceram. Int.* 40 (2014) 7185–7193. doi:10.1016/j.ceramint.2013.12.057.
- [111] L. Saleh Ghadimi, N. Arsalani, I. Ahadzadeh, A. Hajalilou, E. Abouzari-Lotf, Effect of synthesis route on the electrochemical performance of CoMnFeO_4 nanoparticles as a novel supercapacitor electrode material, *Appl. Surf. Sci.* 494 (2019) 440–451. doi:10.1016/j.apsusc.2019.07.183.
- [112] J.Y. Wang, P.Y. Kuang, N. Li, Z.Q. Liu, Y.Z. Su, S. Chen, Facile hydrothermal synthesis of cobalt manganese oxides spindles and their magnetic properties, *Ceram. Int.* 41 (2015)

- 8670–8679. doi:10.1016/j.ceramint.2015.03.083.
- [113] M. Baek, D. Kim, K. Yong, Simple but effective way to enhance photoelectrochemical solar-water-splitting performance of ZnO nanorod arrays: Charge-trapping Zn(OH)₂ annihilation and oxygen vacancy generation by vacuum annealing, *ACS Appl. Mater. Interfaces*. 9 (2017) 2317–2325. doi:10.1021/acsami.6b12555.
- [114] P.T. Babar, A.C. Lokhande, B.S. Pawar, M.G. Gang, E. Jo, C. Go, M.P. Suryawanshi, S.M. Pawar, J.H. Kim, Electrocatalytic performance evaluation of cobalt hydroxide and cobalt oxide thin films for oxygen evolution reaction, *Appl. Surf. Sci.* 427 (2018) 253–259. doi:10.1016/j.apsusc.2017.07.142.
- [115] S. Anantharaj, S.R. Ede, K. Karthick, S. Sam Sankar, K. Sangeetha, P.E. Karthik, S. Kundu, Precision and correctness in the evaluation of electrocatalytic water splitting: Revisiting activity parameters with a critical assessment, *Energy Environ. Sci.* 11 (2018) 744–771. doi:10.1039/c7ee03457a.
- [116] H. Zhang, X. Li, A. Hähnel, V. Naumann, C. Lin, S. Azimi, S.L. Schweizer, A.W. Maijenburg, R.B. Wehrspohn, Bifunctional Heterostructure Assembly of NiFe LDH Nanosheets on NiCoP Nanowires for Highly Efficient and Stable Overall Water Splitting, *Adv. Funct. Mater.* 28 (2018) 1–10. doi:10.1002/adfm.201706847.
- [117] J. Bao, J. Xie, F. Lei, Z. Wang, W. Liu, L. Xu, M. Guan, Y. Zhao, H. Li, Two-dimensional Mn-Co LDH/graphene composite towards high-performance water splitting, *Catalysts*. 8 (2018). doi:10.3390/catal8090350.
- [118] M. Gao, W. Sheng, Z. Zhuang, Q. Fang, S. Gu, J. Jiang, Y. Yan, Efficient water oxidation using nanostructured α -nickel-hydroxide as an electrocatalyst, *J. Am. Chem. Soc.* 136

- (2014) 7077–7084. doi:10.1021/ja502128j.
- [119] Y. Shi, B. Zhang, Recent advances in transition metal phosphide nanomaterials: Synthesis and applications in hydrogen evolution reaction, *Chem. Soc. Rev.* 45 (2016) 1529–1541. doi:10.1039/c5cs00434a.
- [120] S. Anantharaj, S.R. Ede, K. Sakthikumar, K. Karthick, S. Mishra, S. Kundu, Recent Trends and Perspectives in Electrochemical Water Splitting with an Emphasis on Sulfide, Selenide, and Phosphide Catalysts of Fe, Co, and Ni: A Review, *ACS Catal.* 6 (2016) 8069–8097. doi:10.1021/acscatal.6b02479.
- [121] A.D. Jagadale, G. Guan, X. Li, X. Du, X. Ma, X. Hao, A. Abudula, Ultrathin nanoflakes of cobalt-manganese layered double hydroxide with high reversibility for asymmetric supercapacitor, *J. Power Sources.* 306 (2016) 526–534. doi:10.1016/j.jpowsour.2015.12.097.
- [122] G. Jia, Y. Hu, Q. Qian, Y. Yao, S. Zhang, Z. Li, Z. Zou, Formation of Hierarchical Structure Composed of (Co/Ni)Mn-LDH Nanosheets on MWCNT Backbones for Efficient Electrocatalytic Water Oxidation, *ACS Appl. Mater. Interfaces.* 8 (2016) 14527–14534. doi:10.1021/acsami.6b02733.
- [123] P. Zhang, L. Li, D. Nordlund, H. Chen, L. Fan, B. Zhang, X. Sheng, Q. Daniel, L. Sun, Dendritic core-shell nickel-iron-copper metal/metal oxide electrode for efficient electrocatalytic water oxidation, *Nat. Commun.* 9 (2018) 1–10. doi:10.1038/s41467-017-02429-9.
- [124] L. Yu, H. Zhou, J. Sun, F. Qin, F. Yu, J. Bao, Y. Yu, S. Chen, Z. Ren, Cu nanowires shelled with NiFe layered double hydroxide nanosheets as bifunctional electrocatalysts for

- overall water splitting, *Energy Environ. Sci.* 10 (2017) 1820–1827. doi:10.1039/c7ee01571b.
- [125] A.L. Wang, H. Xu, G.R. Li, NiCoFe Layered Triple Hydroxides with Porous Structures as High-Performance Electrocatalysts for Overall Water Splitting, *ACS Energy Lett.* 1 (2016) 445–453. doi:10.1021/acseenergylett.6b00219.
- [126] Y. Hou, M.R. Lohe, J. Zhang, S. Liu, X. Zhuang, X. Feng, Vertically oriented cobalt selenide/NiFe layered-double-hydroxide nanosheets supported on exfoliated graphene foil: An efficient 3D electrode for overall water splitting, *Energy Environ. Sci.* 9 (2016) 478–483. doi:10.1039/c5ee03440j.
- [127] F. Ming, H. Liang, H. Shi, X. Xu, G. Mei, Z. Wang, MOF-derived Co-doped nickel selenide/C electrocatalysts supported on Ni foam for overall water splitting, *J. Mater. Chem. A.* 4 (2016) 15148–15155. doi:10.1039/c6ta06496e.
- [128] W. Fang, D. Liu, Q. Lu, X. Sun, A.M. Asiri, Nickel promoted cobalt disulfide nanowire array supported on carbon cloth: An efficient and stable bifunctional electrocatalyst for full water splitting, *Electrochem. Commun.* 63 (2016) 60–64. doi:10.1016/j.elecom.2015.10.010.
- [129] S. Du, Z. Ren, J. Zhang, J. Wu, W. Xi, J. Zhu, H. Fu, Co₃O₄ nanocrystal ink printed on carbon fiber paper as a large-area electrode for electrochemical water splitting, *Chem. Commun.* 51 (2015) 8066–8069. doi:10.1039/c5cc01080b.
- [130] S. Deng, Y. Zhong, Y. Zeng, Y. Wang, X. Wang, X. Lu, X. Xia, J. Tu, Hollow TiO₂@Co₉S₈ Core–Branch Arrays as Bifunctional Electrocatalysts for Efficient Oxygen/Hydrogen Production, *Adv. Sci.* 5 (2018). doi:10.1002/ADVS.201700772.

- [131] H. Liang, L. Li, F. Meng, L. Dang, J. Zhuo, A. Forticaux, Z. Wang, S. Jin, Porous Two-Dimensional Nanosheets Converted from Layered Double Hydroxides and Their Applications in Electrocatalytic Water Splitting, *Chem. Mater.* 27 (2015) 5702–5711. doi:10.1021/acs.chemmater.5b02177.
- [132] D. Liu, Q. Lu, Y. Luo, X. Sun, A.M. Asiri, NiCo₂S₄ nanowires array as an efficient bifunctional electrocatalyst for full water splitting with superior activity, *Nanoscale.* 7 (2015) 15122–15126. doi:10.1039/c5nr04064g.
- [133] R. Khan, M.T. Mehran, M.M. Baig, B. Sarfraz, S.R. Naqvi, M.B. Muhammad, M.Z. Khan, A.H. Khoja, 3D hierarchical heterostructured LSTN@NiMn-layered double hydroxide as a bifunctional water splitting electrocatalyst for hydrogen production, *Fuel.* 285 (2021) 119174. doi:10.1016/j.fuel.2020.119174.
- [134] L. Zhou, S. Jiang, Y. Liu, M. Shao, M. Wei, X. Duan, Ultrathin CoNiP@Layered Double Hydroxides Core-Shell Nanosheets Arrays for Largely Enhanced Overall Water Splitting, *ACS Appl. Energy Mater.* 1 (2018) 623–631. doi:10.1021/acsaem.7b00151.
- [135] P.S. Jain, V.S. Darshane, Cation distribution of the system Zn_{1-x}Co_xFeMnO₄ by x-ray, electrical conductivity and Mössbauer studies, *Pramana.* 20 (1983) 7–17. doi:10.1007/BF02846175.
- [136] Z. Li, B. Li, J. Chen, Q. Pang, P. Shen, Spinel NiCo₂O₄ 3-D nanoflowers supported on graphene nanosheets as efficient electrocatalyst for oxygen evolution reaction, *Int. J. Hydrogen Energy.* 44 (2019) 16120–16131. doi:10.1016/j.ijhydene.2019.04.219.
- [137] P.W. Menezes, A. Indra, N.R. Sahraie, A. Bergmann, P. Strasser, M. Driess, Cobalt-manganese-based spinels as multifunctional materials that unify catalytic water oxidation

- and oxygen reduction reactions, *ChemSusChem*. 8 (2015) 164–167. doi:10.1002/cssc.201402699.
- [138] T. Zhao, S. Gadipelli, G. He, M.J. Ward, D. Do, P. Zhang, Z. Guo, Tunable Bifunctional Activity of $\text{Mn}_x\text{Co}_{3-x}\text{O}_4$ Nanocrystals Decorated on Carbon Nanotubes for Oxygen Electrocatalysis, *ChemSusChem*. 11 (2018) 1295–1304. doi:10.1002/cssc.201800049.
- [139] X. Huang, H. Zheng, G. Lu, P. Wang, L. Xing, J. Wang, G. Wang, Enhanced Water Splitting Electrocatalysis over MnCo_2O_4 via Introduction of Suitable Ce Content, *ACS Sustain. Chem. Eng.* 7 (2019) 1169–1177. doi:10.1021/acssuschemeng.8b04814.
- [140] H. Sim, J. Lee, T. Yu, B. Lim, Manganese oxide with different composition and morphology as electrocatalyst for oxygen evolution reaction, *Korean J. Chem. Eng.* 35 (2018) 257–262. doi:10.1007/s11814-017-0247-2.
- [141] M. Zulqarnain, A. Shah, M.A. Khan, F. Jan Iftikhar, J. Nisar, FeCoSe_2 Nanoparticles Embedded in $\text{g-C}_3\text{N}_4$: A Highly Active and Stable bifunctional electrocatalyst for overall water splitting, *Sci. Rep.* 10 (2020) 1–8. doi:10.1038/s41598-020-63319-7.
- [142] L. Gao, E. Han, Y. He, C. Du, J. Liu, X. Yang, Effect of different templating agents on cobalt ferrite (CoFe_2O_4) nanomaterials for high-performance supercapacitor, *Ionics (Kiel)*. 26 (2020) 3643–3654. doi:10.1007/s11581-020-03482-z.
- [143] J. Yuan, C. Chen, Y. Hao, X. Zhang, R. Agrawal, C. Wang, X. Li, Y. Hao, B. Liu, Q. Li, Y. Xie, Three-dimensionally porous CoMn_2O_4 thin films grown on Ni foams for high-performance lithium-ion battery anodes, *J. Mater. Sci.* 52 (2017) 5751–5758. doi:10.1007/s10853-017-0810-6.

APPENDICES

Appendix “A” Main Reagents and Materials

The reagents and materials used in this work and their origin are listed in Table A.1

Table A. 1 Main reagents and materials

Reagents and materials	Quality
NF	PN-04 pure, thickness: 1.6 mm, bulk density: 0.42 g cm ⁻³ , Alantum
Hydrochloric acid	≥ 35%
NiCl ₂ ·6H ₂ O	≥ 98.0%
FeCl ₃ ·6H ₂ O	≥ 98.0%
CoCl ₂ ·6H ₂ O	≥ 98.0%
Ni(NO ₃) ₂ ·6H ₂ O	≥ 98.0%
Co(NO ₃) ₂ ·6H ₂ O	≥ 98.0%
Fe(NO ₃) ₃ ·9H ₂ O	≥ 98.0%
MnSO ₄ ·H ₂ O	≥ 98.0%
Urea	≥ 98.0%
NH ₄ F	≥ 98.0%
KOH	≥ 95.0%
H ₂ O ₂	30% w/v.
Milli-Q ultrapure water	18.4 MΩ cm
Methanol	≥ 98.0%
Ethanol	Assay 94.02 v%
Acetone	≥ 99.5%

Appendix “B” Synthesis and Characterization Tools

B.1 Experimental instrument and its usage

Table B.1 shows the other experimental instruments and their usage

Table B. 1 Other experimental instruments and their usage

Instrument	Model	Usage
Ultrasonic cleaner	BRANSON 2210R-DTH	Cleaning substrate
Drying oven	JISICO J-924 AHO	Drying sample
Vacuum oven	JISICO J-924 AHO	Avoiding sample oxidation
Desiccator	Korea Ace Scientific Co., LTD	Preserve sample
Analytical Balances	SHINKO DENSHICO., LTD (AF-R220E-D)	Weigh the sample
Electrochemical measurement	WonATeche, WMPG1000 Multichannel Potentiostat	OER, HER

B.2 Characterization Instruments and Model

Table B. 2 Characterization instruments and their type

Instrument	Model
XRD	Philips, Eindhoven, Netherlands
XPS	VG Multilab 2000
FE-SEM	JSM-6701F (JEOL, Japan)
TEM	JEOL-3010
Raman Spectroscopy	Horiba Jobin-Yvon LabRam Aramis 151

Different instruments were employed in this study to characterize the materials fabricated and trace the reactions during the synthesis processes. This section mainly introduces the catalyst characterization techniques used in this work, and the material structure and the specific method characteristics of various physical properties are described in detail. The characterization technology helps optimize the preparation process of catalysts, improve the quality of materials, and lay a foundation for subsequent applications basis.

Appendix “C” Electrolyte Preparation and Microscopy Sample Preparation

C.1 1 M KOH Electrolyte Preparation

1. Wear gloves and calibrate the analytical balance.
2. Weigh 3.9140 g of KOH white sheet powder and put it into a beaker.
3. Add 70 ml of deionized water slowly and gently, and seal it in a fume hood.
4. Stir continuously with a magnetic stirrer for 20 min to ensure that the KOH particles are completely dissolved in deionized water to form a uniform electrolyte solution.

C.2 TEM Sample Preparation

1. Use scissors to cut the sample to an appropriate size of 1 cm* 1cm so that the fabricated materials of the sample can be enough for the test.
2. Put the sample into a 10 mL capacity glass bottle, and pour 6 mL of ethanol to immerse the sample.
3. Use an ultrasonic cleaner to sonicate the sample for 5 h to gain the peeled synthesized material from the NF.
4. Use a Copper grid to support the peeled material to prepare for TEM measurement.